Nonlinear Response in Active Microrheology

Inaugural-Dissertation

zur Erlangung des Doktorgrades
der Mathematisch-Naturwissenschaftlichen Fakultät
der Heinrich-Heine-Universität Düsseldorf

vorgelegt von

Ting Wang

aus Jiande, China

Köln, Juli 2015

aus dem Institut für Theoretische Physik II : Weiche Materie
der Heinrich-Heine-Universität Düsseldorf

Gedruckt mit der Genehmigung der
Mathematisch-Naturwissenschaftlichen Fakultät der
Heinrich-Heine-Universität Düsseldorf

Referent: Prof. Dr. Jürgen Horbach

Korreferent: Prof. Dr. Hartmut Löwen

Tag der mündlichen Prüfung: 25.09.2015

Eidesstattliche Versicherung

Ich versichere an Eides Statt, dass die Dissertation von mir selbständig und ohne unzulässige fremde Hilfe unter Beachtung der Grundsätze zur Sicherung guter wissenschaftlicher Praxis an der Heinrich-Heine-Universität Düsseldorf erstellt worden ist.

Köln, den 28.07.2015

Ting Wang

Acknowledgement

First of all, I would like to thank my supervisor Dr. Matthias Sperl for introducing me the exciting doctoral research topic: active microrheology, and for his continuing financial support. Without him, this thesis is impossible. I am very grateful to him for giving me sufficient freedom to train me to become an independent researcher.

I thank Prof. Dr. Jürgen Horbach for supervising my thesis in Düsseldorf university.

I thank our cooperators Matthias Grob and Prof. Dr. Annette Zippelius for simulation input. I thank Andrea for discussion about her simulation details, and thank Till for sharing many derivation details in his granular MCT.

I thank Prof. Dr. Thomas Voigtmann and Prof. Mathias Fuchs for many valuble discussions on MCT and microrheology as well. I thank Prof. Dr. John Brady for his enlightening discussion on the microrheology in the low density limit.

I thank following friends: Hailong, thank you for teaching me so many useful simulation skills. Sixue Qin and Yunlong, thank you for encouragement and interesting discussion on physics.

I also want to thank following of my colleagues: Elmar and Peidong, thank you for great help in my everyday life. Anoosheh, thank you for creating quite environment and interesting discussions. Hideyuki, thank you for critical comments on my manuscript and valuable suggestions on physics. Sebastian, thank you for help to translate the abstract into German.

I thank my wife Ming and my new born baby Xinning, for bring me magic power.

Publication

Peer-reviewed

"Active microrheology of driven granular particles", *Phys. Rev. E* 89, 042209 (2014) **Ting Wang**, Matthias Grob, Annette Zippelius, and Matthias Sperl.

Abstract: When pulling a particle in a driven granular system with constant force F_{ex}, the probe particle may approach a steady-state velocity v. The corresponding friction coefficient of the probe $\zeta = Fex/v$ is obtained by a schematic model of mode coupling theory (MCT) and a direct event-driven simulation. In small and moderate drag force regime, the general fitting of the schematic model with the simulation result indicates the energy dissipation of collision play a negative role to the glass transition. In large force regime, the origin of the increasing scaling law of the friction coefficient found in [Fiege et al., Granular Matter **14**, 247 (2012)] is analysed by a simple kinetic theory.

Contribution: M. Grob and Prof. A. Zippelius performed the simulation. Dr. M. Sperl proposed the idea to apply a schematic model to fit the simulation result. I constructed the schematic model including short time dynamics, and proposed the idea of kinetic argument to clarify the mechanism of thickening. I wrote the first manuscript. All authors revised the manuscript together.

Pre-print

"Thinning and thickening in active microrheology" *Arxiv*:1504.02277 (2015).
Ting Wang and Matthias Sperl

Abstract: When pulling a probe particle in a many-particle system with fixed velocity, the probe's effective friction, defined as average pulling force over its

velocity, $\gamma_{eff} := \langle F_{ex} \rangle / u$, first keeps constant (linear response), then decreases (thinning) and finally increases (thickening). We propose a three-time-scales picture (TTSP) to unify thinning and thickening behaviour. The points of the TTSP are that there are three distinct time scales of bath particles: diffusion, damping, and single probe-bath (P-B) collision; the dominating time scales, which are controlled by the pulling velocity, determine the behaviour of the probe's friction. We confirm the TTSP by Langevin dynamics simulation. Microscopically, we find that for computing the effective friction, Maxwellian distribution of bath particles' velocities works in low Reynolds number (Re) but fails in high Re. It can be understood based on the microscopic mechanism of thickening obtained in the T=0 limit. Based on the TTSP, we explain different thinning and thickening observations in some earlier literature.

Contribution: I proposed the idea, performed the simulation and wrote the manuscript. Dr. M. Sperl and I revised the manuscript together.

Abstract

When pulling a probe particle in a many-particle system with fixed force, the probe may approach a steady velocity. the effective friction of the probe, defined as the pulling force over its average velocity, $\gamma_{eff} := F_{ex}/\langle u \rangle$, exhibits intriguing non-linear behaviours with increase of the pulling force: it first keeps constant (linear response), then decreases (thinning), and finally keeps constant for colloidal suspensions but increases for granular particles.

The goal of this thesis is to understand the non-linear behaviour in the active microrheology, in particular, to understand why thickening happens in the granular particle systems, but not in the earlier colloidal suspensions.

To achieve this, we study the microrheology in both low and high density. In the low density limit, we first construct a simple kinetic model, and find that inertia causing thickening. Then we extend the model to include the thinning regime. The thinning and thickening behaviour of the probe is unified by a three-time-scales picture: the thinning/thickening is determined by the interplay of the three time scales of bath particles: diffusion, damping and single probe-bath particles collision. This picture is confirmed by a Langevin dynamics simulation. Correspondingly, the microscopic mechanism of thickening is obtained as well: the crossover from the creep motion of the bath particle to the direct single collision leads to the thickening behaviour.

In high density, we extend the MCT to include the force-dependent short time decay, which is crucial for thickening. First we construct a schematic-MCT model, which can exhibit thickening behaviour as the friction contains the square of the force. And we apply it to fit simulation data of pulling in driven granular particles. Microscopically, we obtain the force dependent memory term in the schematic model by a MCT calculation.

Zusammenfassung

Beim Ziehen eines Testpartikels durch ein Vielteilchensystem mit konstanter Kraft, nähert sich das Teilchen einer gleichbleibenden Geschwindigkeit an. Die effektive Reibung des Teilchens, welche durch die Zugkraft geteilt durch die Durchschnittsgeschwindigkeit definiert ist, $\gamma_{\text{eff}} := F_{\text{ex}}/\langle u \rangle$, zeigt dabei interessante nichtlineare Eigenschaften mit steigender Zugkraft: Sie bleibt zunächst konstant (lineares Verhalten), wird dann kleiner (thinning), um dann schließlich für kolloidale Suspensionen konstant zu bleiben oder für Granulate anzusteigen.

Das Ziel dieser Arbeit ist es, das nichtlineare Verhalten der aktiven Mikrorheologie zu verstehen, insbesondere, zu verstehen, warum es in granularen Teilchensystemen zu einer Verdickung kommt, nicht aber bei den oben genannten Kolloiden.

Um dies zu erreichen, wollen wir Mikrorheologie bei niedrigen und hohen Dichten untersuchen. Für den Grenzfall sehr niedriger Dichten erstellen wir erst ein einfaches kinetisches Modell, um festzustellen, dass Trägheit Verdickung er-zeugt. Wir erweitern dieses Modell dann auf das Verdünnungsregime. Das Verdünnungs- und Verdickungsverhalten des Testteilchens wird durch ein Drei-Zeitskalen-Bild erklärt: Verdünnung/Verdickung wird durch das Zusammenspiel der drei Zeitskalen mit den Badpartikeln bestimmt: Diffusion, Dämpfung und Einzelstöße zwischen Test- und Badteilchen. Dieses Bild wird mittels einer Langevindynamiksimulation bestätigt. Dementsprechend wird auch der mikroskopische Mechanismus erhalten: Der Übergang des Kriechverhaltens der Badpartikel hin zu direkten Einzelstößen führt zur Verdickung.

Für hohe Dichten erweitern wir die MCT, um den kraftabhängigen Zerfall auf kleinen Zeitskalen mit einzuschließen, was für Verdickung entscheidend ist. Zunächst erstellen wir ein schematisches MCT-Modell, welches Verdickungsverhalten auf-weisen kann, da die Kraft quadratisch in die Reibung eingeht. Wir passen

dies dann auf Simulationsdaten von Zugversuchen in getriebenen Granulaten an. Mikroskopisch erhalten wir in diesem schematischen Modell dann den kraftabhängigen Memory-Term durch MCT-Berechnungen.

Contents

Chapter 1

Introduction

Rheology [1] studies flow and deformation of materials under external forces [1, 2]. It can be applied to all kinds of materials, ranging from simple liquids to *complex fluids*. The later includes colloidal suspensions, granular materials, polymers, gels, active bacteria, etc. A comprehensive review of rheology of different complex fluids can be found in ref. [3]. Conventionally, external forces are applied to the bulk materials (for instance, simple shear), which is referred to as *macrorheology*. Due to experimental developments in the past two decades [4, 5], forces can also be applied to a single particle size level (such as passively monitor the motion of a single particle, or actively pulling a particle embedded in a bulk materials), which is referred to as *microrheology*.

The task of this thesis is to investigate the non-linear response behaviour of active microrheology. We first introduce the phenomena of micro-shear thinning and thickening in active microrheology, and compare them with macro-shear thinning and thickening in macrorheology. Then we briefly discuss two typical theoretical methods to calculate the non-linear response of the active microrheology: 1) in low density, the two-body Smolukwuski equation and 2) in high density, the mode-coupling theory (MCT). The main goal of this thesis is to develop these two methods to include thickening, which will be discussed in detail in the following chapters.

[1] The term "rheo" originated from Greek, means to flow.

1.1 Microrheology

Microrheology studies the deformation and the flow of materials under micro-mechanical control [6, 7]. It can be classified into two categories:

- passive-microrheology. The diffusive motion of a probe particle is monitored, e.g., by diffusive wave spectroscopy [8] or confocal microscopy [9], and the visco-elastic properties, the frequency dependent storage and loss moduli, are yield by the fluctuation-dissipation relation [6], which connects the response of an observable to the thermal fluctuations.

- active-microrheology. The motion of a probe is controlled by an external force, which can be realized by magnetic [10] or optical [11] tweezers in colloidal suspensions, or direct mechanic pulling [12, 13, 14] in granular matter.

While in passive microrheology, only linear response to the thermal fluctuations is possible, in active microrheology, nonlinear response can also be realized by pulling with large forces. It provides not only a novel method to understand materials' viscoelasticity on the microscopic level [15, 16, 17, 18] but also a nice example of studying the response theory, which is a fundamental issue in statistical mechanics [19, 20, 21, 22, 23].

1.1.1 Phenomena: micro-shear thinning and thickening

A typical experiment of active microrheology is to pull a probe particle embedded in a complex fluid with fixed velocity then measure the average force, or pull it with fixed force, then measure the average velocity [24, 25] [2]. Let us pull a probe particle in a colloidal or driven granular system with constant force F_{ex} (see fig. 1.1), then the probe particle may approach a steady velocity u. Correspondingly, we can define an effective friction coefficient of the probe as the external pulling force over its steady velocity

$$\gamma_{eff} := F_{ex}/\Big\langle u \Big\rangle, \tag{1.1}$$

which exhibits interesting non-monotone behaviours both in the colloidal suspen-

[2] Typically, for the same system, the friction for the fixed velocity pulling is larger than the one for the fixed force pulling, because the former has to break the build-up of the surrounding particles along the moving direction, while the latter has freedom to choose a less build-up way [24, 25], which is also confirmed experimentally in [26].

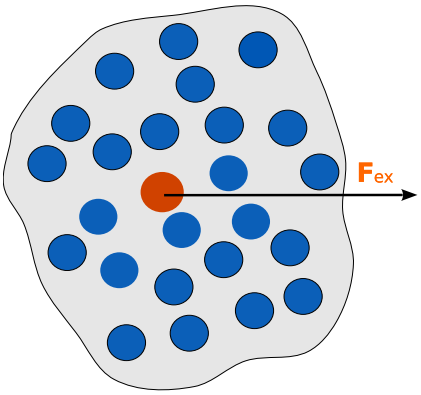

Figure 1.1: Sketch of active microrheology of pulling with fixed force. A probe particle (red) is embedded in host bath particles (blue). All particles are immersed in a solvent (gray). The particles are agitated either by thermal fluctuations for colloidal suspensions or external random driving for granular materials. An external fixed force F_{ex} is applied to pull the probe particle (red) only.

sion [27] and granular systems [28].

- For a colloidal suspension of hard sphere particles [27], see Fig.1.2 left. with fixed packing fraction Φ, the effective friction γ_{eff} keeps constant (linear response) in the small pulling force regime and starts to decrease only (thinning) to a constant value in the large force regime, i.e.

$$\gamma_{eff} \propto F_{ex}^{0} \tag{1.2}$$

  as $F_{ex} \to \infty$. With increasing packing fraction, the effective friction γ_{eff} increases dramatically in the small pulling force regime. Linear response and thinning were observed in colloidal systems in experiments [29, 30] and simulations [31, 32] as well.

- For a driven granular hard sphere system [28], see Fig.1.2 right. The effective friction behaves similar to the one in the colloidal system, except that in the large-force regime, the effective friction does not only decrease in the moderate force regime but also increases in the large force regime, and asymptotically tends to

$$\gamma_{eff} \propto \sqrt{F_{ex}}. \tag{1.3}$$

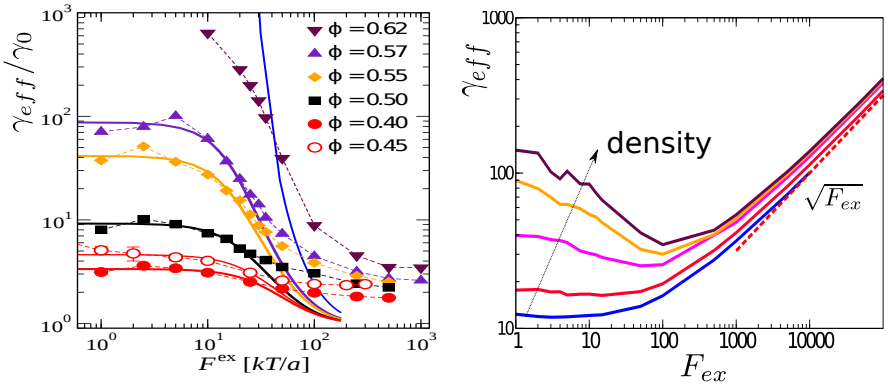

Figure 1.2: Effective friction for increasing external pulling force. Left: colloidal hard sphere system. The points are simulation result, and the lines are schematic mode-coupling theory fits. F_{ex} is the external pulling force, γ_{eff} is the effective friction coefficient rescaled by the solvent friction γ_0, Φ is the packing fraction. The figure is adopted from [27]. Right: driven granular hard sphere system. The arrow indicates the direction of the increasing of the density. The dashed line indicates the scaling of $\sqrt{F_{ex}}$. Data are reproduced from the original velocity-force relation in [28]

.

In short, in the microrheology of fixed force pulling experiments, linear response and thinning occurs in the colloidal system [27]; while in the driven granular system [28], besides linear response and thinning, thickening also occurs.

In addition, for the fixed velocity pulling, thickening was also observed for the static granular systems (surrounding particles at rest), by experiment in refs. [13, 14] and simulation in ref. [33]. All data exhibit the same scaling law [3]

$$\gamma_{eff} \propto u \tag{1.4}$$

But no thinning behaviour was observed for the static granular system. It will be explained why thinning was not observed by a time scales picture in chapter 3.

[3]The scaling is essentially the same with the fixed force pulling by noting that $\gamma_{eff} = F_{ex}/u \propto u \rightarrow \gamma_{eff} \propto \sqrt{F_{ex}}$

1.1.2 Granular materials vs. colloidal suspensions

Why does thickening occur in granular particles, but not in the colloidal suspensions? To better understand the discrepancy, let us compare some fundamental differences between them.

Colloidal particles have small size, ranging from $1nm$ to $1\mu m$ [34] Typically, they are over-damped due to the large viscosity of the solvent, and affects by the temperature due to the thermal fluctuations from the solvent.

Granular particles have much larger size, ranging from $10\mu m$ to $10cm$. The viscosity of the surrounding medium of them is typically much smaller than the one of colloidal particles. They can lose kinetic energy through inelastic collisions [35]. Temperature is ignorable for static granular particles.

Note that granular particles can also be agitated by external random forces to balance the dissipative collisions between particles. In this aspect, as colloids, they can behave like a thermal system as well. Thus for driving granular particles, the intrinsic differences from colloids are 1) dissipative collisions and 2) small viscosity. It will be clarified in the following chapters that not dissipation but small viscosity is the essential point for thickening.

1.1.3 Comparison with macrorheology

A typical macrorheology measurement is the simple shear of a bulk material, i.e. applying a fixed shear stress σ (defined as the total force along the shear direction over the area of one plane, $\sigma := F_x/A$) to the two parallel planes of it, then observing how the materials deforms. As illustrated in Fig. 1, for fixed stress σ, there are two limiting deformation cases:

- Elastic solid. After some transient time, the deformation along the stress stops (solidity), which is characterized by the strain κ (defined as the displacement of the top plane over its hight $\kappa := \Delta x/h$). The corresponding shear modulus G can be defined as the applied stress over the responding strain

  $$G := \sigma/\kappa, \tag{1.5}$$

  which indicates the rigidity of a solid against an applied shear. Ideally, the strain is proportional to the external stress, the shear modulus is independent

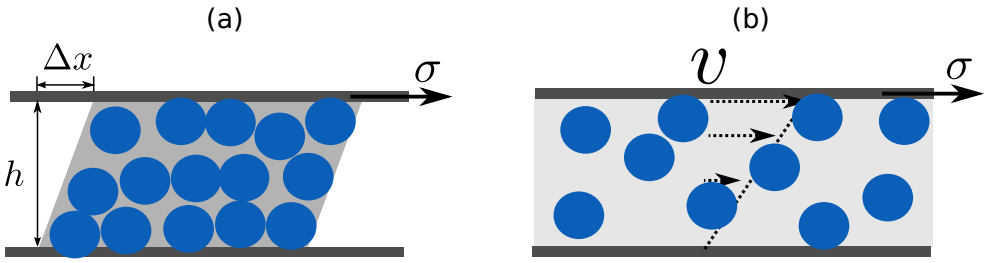

Figure 1.3: Sketch of simple shear for a solid and a fluid. For both materials, a shear stress σ is applied to the top plane of the material. The deformations are different. (a) For a solid, the deformation stops with strain $\kappa = \Delta x/h$. (b) For a fluid, the deformation continues in time with constant shear rate $\dot{\kappa} = dv/dy$. The arrows in the bulk indicate the velocity field of the flow. (The figure is adapted from [36].)

of the strain, which is an *elastic solid*.

- Newtonian fluid. After some transient time, the deformation along the stress keeps constant speed, i.e. $\dot{\kappa} = \Delta\dot{x}/h = const.$ (fluidity). The corresponding viscosity η can be defined as the shear stress over its shear rate

$$\eta := \sigma/\dot{\kappa}. \tag{1.6}$$

  Ideally, the shear rate is proportional to the applied stress, which is a *Newtonian fluid*.

Many soft materials are neither ideal solid nor ideal fluid, they exhibit both elastic and viscous properties. Here we focus on the unideal fluid property, i.e. the flow is non-Newtonian. The relation between the shear stress and the shear rate is nonlinear, either *thinning* – the viscosity decreases with increasing of the shear rate (or stress), or *thickening* – the viscosity increases with increasing of the shear rate (or stress).

The control variables and observables in the simple shear are similar to the ones in the single particle pulling experiments as shown in the following table

Microrheology	Macrorheology
force F_{ex}	stress σ
velocity u	shear rate $\dot{\kappa}$
friction $\gamma = F_{ex}/u$	viscosity $\eta = \sigma/\dot{\kappa}$

Furthermore, they also exhibit similar non-Newtonian behaviour. In the macrorheology of the simple shear,

- For colloidal suspensions, linear response and shear thinning are typically observed [37, 38, 39], and also thickening [40, 41]. Conventionally, thickening is explained due to hydrodynamical interaction (HI) causing cluster forming of particles [42]. And a recent simulation [43] found that friction between particles plays the key role but not the HI.

- For granular materials, a typical thickening behaviour is that the shear stress is propotional to the square of the shear rate,

$$\sigma \propto \dot{\kappa}^2, \tag{1.7}$$

  as proposed by Bagnold [44]. The Bagnold law describes the inertial effect of rapid shear granular flow [45, 46]. Noting that if we replace the variables in the Bagnold law (1.7) by their microscopic corresponding variables as shown in the above table, we get $F_{ex} \propto u^2$, which equals the scaling law (1.4).

1.2 Two theoretical methods

Theoretically, there are two different methods for the calculation of the nonlinear force dependent effective friction of active microrheology: the effective two body Smoluchowski equation [24] in low density, and the non-equilibrium mode-coupling theory (MCT) [27, 47] in high density. Here we first give the

microscopic equations, the Smoluchowski equations, and then briefly introduce these two theories.

1.2.1 Microscopic dynamics: under-damped vs. over-damped

Stochastic description: Langevin vs. over-damped Langevein

Let us consider a system of N identical particles suspended in a solvent. One of them, the probe labelled s, is under a constant pulling force $\boldsymbol{F}_{ex}$. The dynamics of each particle obeys the (under-damped) Langevin equation (LE)

$$m\dot{\boldsymbol{v}}_i = -\gamma_0 \boldsymbol{v}_i + \boldsymbol{\xi}_i + \boldsymbol{F}_i + \boldsymbol{F}_{ex}\delta_{i,s}, \tag{1.8}$$

where m is the mass of each particle; γ_0 is the friction coefficient of each particle. The Stokes law [48] gives the friction of each particle as

$$\gamma_0 = 6\pi R\eta, \tag{1.9}$$

where η is the solvent viscosity, and R is the radius of each particle, $\boldsymbol{\xi}_i$ is a Gaussian random force satisfying the fluctuation-dissipation relation

$$\left\langle \xi_i^{\nu}(t)\xi_{i'}^{\mu}(t') \right\rangle = 2\gamma_0 k_B T \delta_{i,i'}\delta^{\nu,\mu}\delta(t-t') \tag{1.10}$$

$\nu, \mu \in \{x, y\}$ are the components of the random force; $\boldsymbol{F}_i$ is the interaction force of other particles to the i-th; $\boldsymbol{F}_{ex}$ is a constant external pulling force on the probe only.

In the large friction γ_0 limit, the inertial term $m\dot{\boldsymbol{v}}_i$ may be dropped, which reduces the dynamics to the over-damped LE

$$\dot{\boldsymbol{r}}_i = \frac{1}{\gamma_0}\Big(\boldsymbol{\xi}_i + \boldsymbol{F}_i + \boldsymbol{F}_{ex}\delta_{i,s}\Big) \tag{1.11}$$

Probability description: Fokker-Planck vs. Smoluchowski

Equivalently, the above stochastic description of the dynamical variables can be transferred to the probability description of the phase-space variables Γ. The dynamical equations of the probability distribution function (PDF) $P(\Gamma, t)$ can be obtained by applying the Kramers-Moyal expansion [49] of the corresponding stochastic equations.

- For the under-damped system, a phase-space point includes both position and velocity of the N particle's

$$\Gamma = \left(\boldsymbol{r}_1, \cdots, \boldsymbol{r}_N, \boldsymbol{v}_1, \cdots \boldsymbol{v}_N\right) \tag{1.12}$$

The dynamical equation of the PDF obeys the Fokker-Planck equation (FPE)

$$\partial_t P(\mathbf{\Gamma}, t) = \Big\{ \underbrace{-\left[\boldsymbol{v}_i \cdot \partial_{\boldsymbol{r}_i} + \frac{\boldsymbol{F}_i}{m} \cdot \partial_{\boldsymbol{v}_i}\right]}_{\hat{\Omega}^0_{FP}} + \underbrace{\frac{\gamma_0}{m}\partial_{\boldsymbol{v}_i} \cdot \left[\boldsymbol{v}_i + \frac{k_B T}{m}\partial_{\boldsymbol{v}_i}\right]}_{\hat{\Omega}^1_{FP}} \underbrace{- \frac{\boldsymbol{F}_{ex}}{m} \cdot \partial_{\boldsymbol{v}_s}}_{\hat{\Omega}^{ex}_{FP}} \Big\} P \tag{1.13}$$

where the sum rule for the same index is applied in the equation.

- For the over-damped Langevin equation, a phase-space point is the N-particle positions only

$$\Gamma = \left(\boldsymbol{r}_1, \cdots, \boldsymbol{r}_N\right) \tag{1.14}$$

The corresponding dynamical equation of the PDF obeys the Smoluchowski equation

$$\partial_t P(\mathbf{\Gamma}, t) = \left[D\partial_{\boldsymbol{r}_i} \cdot \left(\partial_{\boldsymbol{r}_i} - \boldsymbol{F}_i\right) - D\boldsymbol{F}_{ex} \cdot \partial_{\boldsymbol{r}_s} \right] P. \tag{1.15}$$

where D is the self diffusion coefficient of a single particle in the low density limit obeying the Einstein relation [50]

$$D = \frac{k_B T}{\gamma_0} \tag{1.16}$$

1.2.2 Low density: two body Smoluchowski equation

In the low density limit, the interaction between bath particles can be ignored. Besides the friction due to the solvent, only the interaction between probe-bath particles (P-B) causes an additional friction of the probe. In this limit, without HI, Squares and Brady derived a two-body Smoluchowski equation (or say diffusion-convection equation) [24]:

$$D\nabla^2 g + \boldsymbol{U} \cdot \nabla g = 0 \tag{1.17}$$

with a reflecting boundary condition (RBC) at the P-B contact surface

$$\boldsymbol{n} \cdot \boldsymbol{j} = D\boldsymbol{n} \cdot \nabla g + \boldsymbol{n} \cdot \boldsymbol{U} g = 0, \quad r = R \tag{1.18}$$

and undisturbed distribution far away

$$g = 1, \quad r \to \infty, \tag{1.19}$$

Where $g(\boldsymbol{r})$ is the P-B pair distribution function in the coordinate of the probe describing the relative number density of bath particles around the probe

$$g(\boldsymbol{r}) = n(\boldsymbol{r})/n_0 \tag{1.20}$$

$n(\boldsymbol{r})$ is the density of bath particles in the coordinate of the probe; $n = N/V$ is the average number density (N is particle number, V is the volume of the system.).

The above two-body SE is derived from the many body SE (1.15) with truncation of the condition average to the P-B pair distribution only, which is valid in the low density limit. The two-body SE (1.17) with BCs (1.18) and (1.19) can be analytically solved by polynomial expansion. The corresponding average velocity of the probe can be obtained by

$$\left\langle U \right\rangle = \frac{1}{\gamma_0}\Big[F_{ex} - nk_BT \oint_{r=R} \boldsymbol{e}_n g(\boldsymbol{r}) ds\Big], \tag{1.21}$$

which results in the increased effective friction relative to the solvent friction, $\Delta\gamma_{eff}/\gamma_0$. Linear response and shear thinning was obtained based on this model.

1.2.3 High density: mode-coupling theory

In high density, the interaction between bath particles no longer can be ignored. Bath particles move slowly and collectively (glassy dynamics) due to crowding. Such glassy dynamics can be described by conventional MCT [4], which predicts a dynamical arrest transition of the system [52] for a quasi-equilibrium state.

As the system is driven out of equilibrium by an external force, the response to the driving can be calculated by a MCT with the integration through transients (ITT) method. The ITT is a generalized Green-Kubo formula, expressing a responding observable by the time autocorrelator of it [53] [54]. The derivation of the ITT will be discussed in chapter 5. The key point of applying the ITT in high density

[4] A quite readable introduction to MCT can be found in ref. [51].

is to project the autocorrelator in the ITT formula onto the density pairs. The latter can then be treated by the standard MCT. This novel ITT-MCT method was first introduced by Fuchs and Cates by applying the ITT to the simple shear of the dense hard-sphere system [55], A review of the method and applications to simple shear can be found in ref. [56].

Recently, the ITT-MCT method was applied to investiage the nonlinear active microrheology [27, 47] as well. The main points of the calculation in [47] are as follows: The dynamics of the system obeys the many body Smoluchowski equation (1.15). The average force is connected by the force autocorrelator of the probe by ITT

$$\left\langle \boldsymbol{F}_s \right\rangle(t) = -D\boldsymbol{F}_{ex} \int_0^t \left\langle \boldsymbol{F}_s \middle| e^{\mathcal{L}_{SM}t'} \middle| \boldsymbol{F}_s \right\rangle dt'. \tag{1.22}$$

where $e^{\mathcal{L}_{SM}t'}$ is the dynamical evolution operator of the N-body Smoluchowski equation. And the force autocorrelator is approximated by the projecting it onto the density pairs of the probe and the bath particles

$$\left\langle \boldsymbol{F}_s \middle| \boldsymbol{F}_s(t) \right\rangle \approx \sum_{\boldsymbol{p},\boldsymbol{q},\boldsymbol{p}',\boldsymbol{q}'} \underbrace{\left\langle \boldsymbol{F}_s \middle| \rho^s_{\boldsymbol{p}}\rho_{\boldsymbol{q}} \right\rangle}_{L} \underbrace{\left\langle \rho^s_{\boldsymbol{p}}\rho_{\boldsymbol{q}} \middle| e^{\mathcal{L}_{SM}t'} \middle| \rho^s_{\boldsymbol{p}'}\rho_{\boldsymbol{q}'} \right\rangle}_{M} \underbrace{\left\langle \rho^s_{\boldsymbol{p}'}\rho_{\boldsymbol{q}'} \middle| \boldsymbol{F}_s \right\rangle}_{R} \tag{1.23}$$

where term (M) can be treated by standard MCT theory, approximating the four correlator by pairs: $\left\langle \rho^s_{\boldsymbol{p}}\rho_{\boldsymbol{q}} \middle| e^{\mathcal{L}_{SM}t'} \middle| \rho^s_{\boldsymbol{p}'}\rho_{\boldsymbol{q}'} \right\rangle \to \phi_{\boldsymbol{q}}(t)\phi^s_{\boldsymbol{q}}(t)$, (A similar calculation will be given in detail in chapter 5.) Terms (L) and (R) just pre factors and can be calculated directly. Thus the force correlator is approximated by the density correlators, which can be treated by the MCT. The ITT-MCT calculation in refs. [27, 47] predicts a linear response and thinning behaviour of the probe.

1.3 Motivation and structure of the thesis

Obviously, thickening in active microrheology is not included either in the two-body Smoluchowski equation, or in the ITT-MCT calculation based on the many-body Smoluchowski equation. Why can't they capture the thickening behaviour? Does the problem come from the Smoluchowski equation, the over-damped description? And what's the mechanism of thickening?

To answer these questions, we apply the under-damped Langevin dynamics and

the corresponding Fokker-Planck equation to describe the system, and investigate the non-linear response behaviour in active microrheology, especially the thickening behaviour, in both low and high density.

The rest of the thesis are organized as follows:

In the first part, we focus on the low density limit. In chapter 2, the thickening phenomenon is captured by simple kinetic models, both for the case of pulling with fixed force, and with fixed velocity.

In chapter 3, we propose a Langevin dynamics model to include both thinning and thickening. And the whole range of the non-linear response is reproduced by the model.

In chapter 4, we discuss the microscopic mechanism for thinning and thickening. We will clearly see what role inertia plays in the microrheology.

In the second part, see chapter 5, we are discuss the microrheology in the high density. Basesd on the Fokker-Planck equation, we develop a MCT of microrheology which can exhibit thickening.

The summary of the main results and a final discussion is given in chapter 6.

Chapter 2

Kinetic Models of Thickening

One of the central issues in active microrheology is to understand the mechanism of thinning and thickening effects, i.e. why the effective friction of the probe will decrease first (thinning) and then increase (thickening) with the external increasing pulling force. In this chapter, we propose a kinetic model to understand the thickening behaviour.

2.1 Kinetic models of thickening I: fixed force pulling

Why does thickening occur in the driven granular system but not in the colloidal system? Here, we study the origin of the discrepancy of the above phenomena by simple kinetic models in the low density limit. (The content of this section except the fixed point analysis for the case of energy dissipation is published in [57].)

2.1.1 Model

Our driven granular system consists of N identical particles interacting with each other and one of them, the probe, experiences a constant pulling force. The equation of motion of the probe is

$$m\dot{\boldsymbol{v}} = -\gamma_0 \boldsymbol{v} + \boldsymbol{F}_{int} + \boldsymbol{\eta}_{dr} + \boldsymbol{F}_{ex}, \tag{2.1}$$

where γ_0 is the bare friction due to the surrounding medium, $\boldsymbol{F}_{int}$ is the particle interacting force, $\boldsymbol{\eta}_{dr}$ is a random Gaussian noise and $\boldsymbol{F}_{ex}$ is the pulling force. The

probe's ensemble average velocity is

$$\Big\langle \boldsymbol{v}(t) \Big\rangle = \frac{\boldsymbol{F}_{ex}}{\gamma_0}\big(1 - e^{-\frac{\gamma_0}{m}t}\big) + \frac{e^{-\frac{\gamma_0}{m}t}}{m}\int_0^t e^{\frac{\gamma_0}{m}t'}\Big\langle \boldsymbol{F}_{int}(t') \Big\rangle dt', \tag{2.2}$$

where the initial velocity and the random force are averaged out: $\Big\langle \boldsymbol{v}_0 \Big\rangle = 0$ and $\Big\langle \boldsymbol{\eta}(t) \Big\rangle = 0$.

2.1.2 Key idea

It is difficult to directly calculate the interaction force $\boldsymbol{F}_{int}$. The key point of our kinetic theory is viewing the dynamics as a series of scattering processes: on collisions, the interaction force causes momentum and energy transfer; between two consecutive collisions, no interaction force exists.

For simplicity, let us consider the equal mass and two-body head-on elastic collision first:

- between two consecutive collisions, the probe will be accelerated by the pulling force.
- on a collision, the probe will totally lose its kinetic energy by collision due to momentum and energy conservation.

Thus, the velocity of the probe exhibits periodic motion, which is illustrated in Fig. 2.1.

2.1.3 Expression of average velocity and friction

The velocity of the probe during a period is

$$\Big\langle \boldsymbol{v}(t) \Big\rangle = \frac{\boldsymbol{F}_{ex}}{\gamma_0}\big(1 - e^{-\frac{\gamma_0}{m}t}\big), \quad 0 \le t \le t_c, \tag{2.3}$$

and the displacement of it during the period, which equals the mean free path l_0, is

$$l_0 = \Big| \int_0^{t_c} \Big\langle \boldsymbol{v}(t) \Big\rangle dt \Big| = \frac{F_{ex}}{\gamma_0}\big[t_c - \frac{m}{\gamma_0}(1 - e^{-\frac{\gamma_0}{m}t_c})\big], \tag{2.4}$$

where l_0 is mean free path assumed to be fixed in the low density limit and t_c is the collision time.

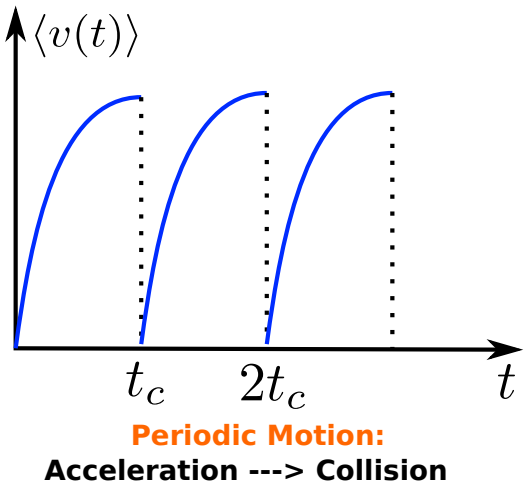

Figure 2.1: Sketch of the periodic motion of the probe due to the equal-mass head-on collision. The probe is accelerating before colliding a bath particles, and completely loses its velocity due to the collision. t_c denotes the time between two consecutive collision events.

For given mean free path l_0 and pulling force F_{ex}, the collision time t_c can be calculated by eq. (2.4). The corresponding average velocity and the effective friction during a period of motion are

$$\left\langle v \right\rangle = l_0/t_c, \tag{2.5}$$

and

$$\gamma_{eff} = F_{ex}/\left\langle v \right\rangle = \frac{F_{ex}t_c}{l_0} \tag{2.6}$$

can be calculated based on eq.2.4 as well.

2.1.4 Result

The effective friction of the probe is numerically calculated based on eqs. (2.4) and (2.6). Before giving the full solution, let us consider the two limiting cases (see Fig.2.2):

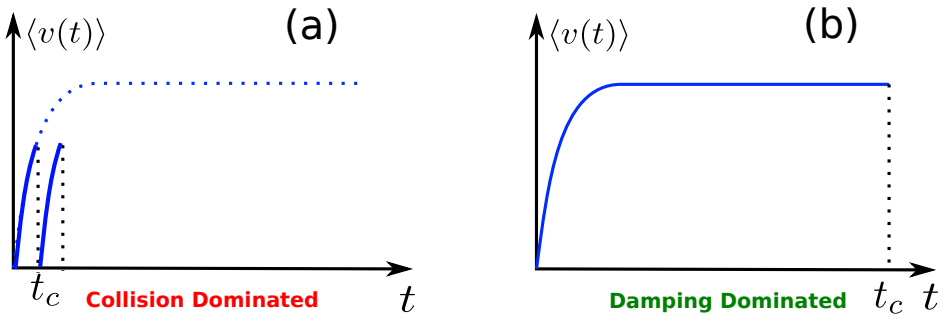

Figure 2.2: Sketch of two limiting cases of the periodic motion. (a) Collision dominated. The collision processes are so frequent that the velocity of the probe is little affected by the damping of the solvent but the collision. (b) Damping dominated. The collision time is so long that in most time the velocity balances with the damping.

(a) Overdamped limit: $t_c \gg \frac{m}{\gamma_0}$, Brownian motion dominates. Equivalently,

$$F_{ex}\gamma_0^2 \ll \frac{l_0}{m}. \tag{2.7}$$

The friction of the probe is just the bare friction from the surrounding medium:

$$\left\langle v_s \right\rangle = F_{ex}/\gamma_0, \quad \gamma = \gamma_0. \tag{2.8}$$

(b) Ballistic limit: $t_c \ll \frac{m}{\gamma_0}$, collision dominates. Equivalently,

$$\frac{F_{ex}}{\gamma_0^2} \gg \frac{l_0}{m}. \tag{2.9}$$

The average velocity and the friction of the probe are

$$\left\langle v_s \right\rangle = \sqrt{\frac{l_0 F_{ex}}{2m}} \propto \sqrt{F_{ex}}, \quad \gamma = \sqrt{\frac{2mF_{ex}}{l_0}} \propto \sqrt{F_{ex}}. \tag{2.10}$$

Both are proportional to the square-root of the external pulling force and independent of the solvent friction.

The whole solution of the force dependent effective friction is plotted in Fig. 2.3.

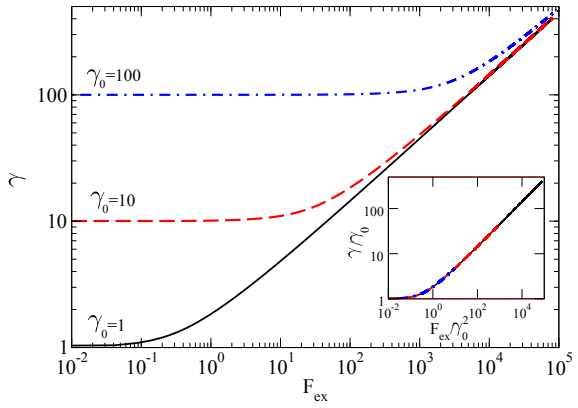

Figure 2.3: Effective friction γ vs. pulling force F_{ex} for different bare friction γ_0. Inset: Overlap of the rescaled variables ($F_{ex} \to F_{ex}/\gamma^2, \quad \gamma \to \gamma/\gamma_0$) of different curves in the main figure.

2.1.5 Discussion

The behaviour of the probe in the large-pulling-force regime is determined by the ratio of the collision time scale over the Brownian velocity relaxation time scale, $t_c/\frac{m}{\gamma_0}$, or equivalently the value of the rescaled force $\frac{F_{ex}m}{\gamma_0^2 l_0}$. In a driven granular system, the bare friction is quite small compared to the one in a Brownian suspension, $\gamma_0 = 1$ in [28] and $\gamma_0 = 50$ in [58], which is the origin of the apparent discrepancy between driven granular systems and Brownian ones under large pulling force. Indeed, one would also obtain the same asymptotic behaviour $\gamma \propto \sqrt{F_{ex}}$ for Brownian systems for extremely large pulling forces.

2.1.6 Role of energy dissipation

For non-equal-mass collisions, or inelastic ones, the velocity of the probe may not totally vanish. Interestingly, by stability analysis of the mapping problem [59], it can be proved that after finite collisions, the probe may achieve a steady average velocity, a stable fixed point, and then exhibit periodic motion again. As a result, the above analytical result is still valid; energy dissipation is non-essential to the asymptotic behaviour.

Momentum conservation holds during the collision process between the probe and a bath particle

$$m_s v_s' + m_b v_b' = m_s v_s + m_b v_b \tag{2.11}$$

Different from colloidal particles, the collision typically is inelastic, which can be modelled by the phenomenon law [35]

$$v_s' - v_b' = -\epsilon(v_s - v_b) \tag{2.12}$$

where ϵ indicates the restitution coefficient. According to Eqs.(2.11) and (2.12), we get the velocity of the probe after collision is

$$v_s' = v_s - \frac{m_2}{m_1 + m_2}(1+\epsilon)(v_s - v_b) \tag{2.13}$$

In the large pulling force regime , the velocity of a bath particle may be ignored, due to the fact $v_s \gg v_b$. In the following, we set $v_b = 0$ and Eq.(2.13) can be written as

$$v_s' = (1-K)v_s \tag{2.14}$$

with $K = \frac{m_b(1+\epsilon)}{m_s+m_b} \in (0,1]$ indicating the effective relative mass. The velocity of the probe is fluctuating in time. Denote its average velocity just after the n-th collision as v_n at collision time t_n. Thus the velocity just before $(n+1)$-th collision can be calculated by the eq. (2.4). Explicitly, we have

$$l_0 = \int_{t_n}^{t_{n+1}} v_n(t)dt = v_n \frac{m_b}{\gamma_0}\Big[1 - e^{-\frac{\gamma_0}{m_b}\Delta t_n}\Big] + \frac{F_{ex}}{\gamma_0}\Big[\Delta t_n - \frac{m}{\gamma_0}(1 - e^{-\frac{\gamma_0}{m}\Delta t_n})\Big], \tag{2.15}$$

where $\Delta t_n = t_{n+1} - t_n$ is the time interval between the n-th and the (n+1)-th collisions. The average velocity just after the $(n+1)$ collision can be expressed based on Eq.(2.2) (here the initial velocity is nonzero.) and Eq.

$$v_{n+1} = (1-k)\Big\{v_n e^{-\frac{\gamma_0}{m_b}\Delta t_n} + \frac{F_{ex}}{\gamma_0}[1 - e^{-\frac{\gamma_0}{m_b}\Delta t_n}]\Big\} \tag{2.16}$$

Note that the time interval $\Delta t_n(v_n)$ is a function of the n-th collision velocity v_n, implicitly given in (2.15). Correspondingly, the velocity of (n+1)-th collision is the function of the n-th collision only, denoting as $v_{n+1} = f(v_n)$.

Stability analysis of fixed point

Physically, after many collision times, the velocity of the probe may become stable. Thus the steady velocity should satisfy the following fixed point equation

$$v_{n+1}^* = f(v_n^*) = v_n^* \tag{2.17}$$

which can be numerically solved based on Eq. (2.15) and (2.16). Furthermore, based on Eq. (2.15) and (2.16), it can be proved that

$$\left|\frac{dv_{n+1}}{dv_n}\right|_{v_n=v_n^*} = e^{-\Delta t_n}(1-k) < 1 \tag{2.18}$$

satisfying the stability condition of a fixed point [59]. In other words, after a transient of many collisions, the motion of the probe shows periodic motion again. Thus the above discussion of the elastic collision can be also applied, which means that the inelastic collision is not essential for the thickening.

2.2 Kinetic models of thickening II: fixed velocity pulling

What happens in the case of fixed velocity pulling? Intuitively, the thickening should also occur due to inertia.

For simplicity, let us consider a toy model of pulling a thin plane with fixed velocity $\boldsymbol{u} = u\boldsymbol{e}_u$, where $\boldsymbol{e}_u = \boldsymbol{u}/|\boldsymbol{u}|$ is the unit vector of $\boldsymbol{u}$. The bath particles are isotropically distributed in space and have only two equal-weighted velocities along the moving plane, $\pm v\boldsymbol{e}_u$. The particles are non-interacting with each other, each of them moves freely before colliding the plane. The only interaction is the collision between the plane and the bath particles. See the schematic Fig. 2.4. We want to get the collision force on the plane and the corresponding effective friction, which depends on the relative velocity:

1) $u < v$. The absolute velocity of the plane is smaller than the one of the bath particles.

- In front of the plane. The collision number is

$$N_f = \frac{1}{2}\rho A|-\boldsymbol{v}-\boldsymbol{u}|\Delta t = \frac{1}{2}\rho(v+u)\Delta t, \tag{2.19}$$

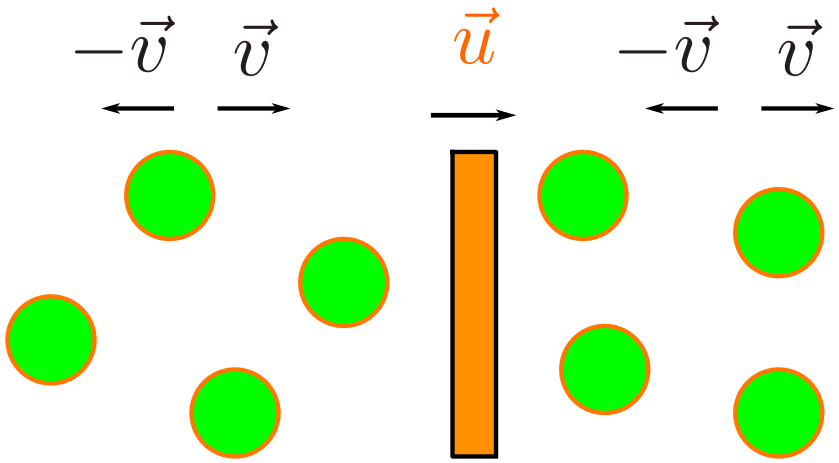

Figure 2.4: Sketch of microrheology with fixed velocity pulling. A plane is pulled with a fixed velocity $\boldsymbol{u}$. Initially, bath particles are isotropically distributed around the probe, and have two kinds of velocities along and opposite the velocity of the probe, $\boldsymbol{v}$,$-\boldsymbol{v}$,with equal probability.

where $\rho = N/V$ is bath particles' number density, A is the area of one side of the plane, and Δt is the time interval. In the frame of the plane, the transferred momentum and force on the plane are

$$\boldsymbol{I}_f = 2m(-\boldsymbol{v} - \boldsymbol{u})N_f = -m\rho A(v+u)^2\Delta t\boldsymbol{e}_u \tag{2.20}$$

$$\boldsymbol{F}_f = \boldsymbol{I}_f/\Delta t = -m\rho A(v+u)^2\boldsymbol{e}_u \tag{2.21}$$

- Behind the plane. The collision number is

$$N_b = \frac{1}{2}\rho A|\boldsymbol{v} - \boldsymbol{u}|\Delta t = \frac{1}{2}\rho(v-u)\Delta t \tag{2.22}$$

The transferred momentum and force to the plane are

$$\boldsymbol{I}_b = 2m(\boldsymbol{v} - \boldsymbol{u})N_b = m\rho A(v-u)^2\Delta t\boldsymbol{e}_u \tag{2.23}$$

$$\boldsymbol{F}_b = \boldsymbol{I}_b/\Delta t = m\rho A(v-u)^2\boldsymbol{e}_u \tag{2.24}$$

The effective friction is defined as the ratio of the total external pulling force acting on the plane over its velocity

$$\gamma_{eff} := |\boldsymbol{F}_{ex}|/|\boldsymbol{u}|. \tag{2.25}$$

For fixed velocity pulling, the external force balances the collision force

$$\boldsymbol{F}_{ex} = -\boldsymbol{F}_{col} = -(\boldsymbol{F}_f + \boldsymbol{F}_b) = 4m\rho A v u \boldsymbol{e}_u \tag{2.26}$$

The corresponding effective friction is

$$\boxed{\gamma_{eff} = |\boldsymbol{F}_f + \boldsymbol{F}_b|/u = 4m\rho A v} \tag{2.27}$$

2) $u \geq v$. The absolute velocity of the plane is larger than the one of the bath particles. In this case, behind the plane, no particles collide with the plane. And in front, there are additional collision forces due to the collision of front bath particles with velocity $\boldsymbol{v}$. The additional collision number and force are

$$N_f' = \frac{1}{2}\rho A(|\boldsymbol{v} - \boldsymbol{u}|)\Delta t = \frac{1}{2}\rho A(u - v)\Delta t \tag{2.28}$$

$$\boldsymbol{F}_f' = 2m(\boldsymbol{v} - \boldsymbol{u})N_f'/\Delta t = -m\rho A(u - v)^2 \boldsymbol{e}_u \tag{2.29}$$

The effective friction is

$$\boxed{\gamma_{eff} = |\boldsymbol{F}_f + \boldsymbol{F}_f'|/u = 2m\rho A(u + \frac{v^2}{u})} \tag{2.30}$$

In summary, the effective friction shows a constant value for small pulling velocity ($u < u$). Then it starts to increase when $u > v$ and tends to asymptotically being proportional to the pulling velocity u. The pulling velocity vs. effective friction is plotted in Fig. 2.4

What can we learn from the toy model? The model proposes a microscopic mechanism for the linear response and the thickening phenomena in the single pulling particle experiment. In the linear response regime, when the velocity of the plane is smaller then the velocity of the bath particles, the plane will be affected by the collisions of the bath particles on both sides of it. The front side (towards its moving direction) will receive the collisions of the bath particles moving opposite of the velocity of the plane, which cause resistance in front; while the back side will receive the particles' collisions along the velocity of the plane, which cause pushing behind.

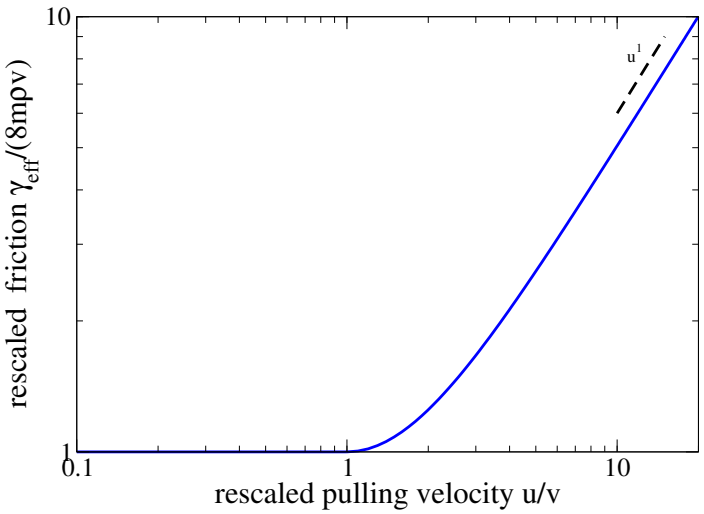

Figure 2.5: Pulling velocity vs. effective friction for the microrheology of fixed velocity pulling. The effective friction keeps constant as the pulling velocity is smaller than the velocity of the bath particles, $u < v$, see eq.(2.27). When $u > v$, the friction starts to increase and tends to be proportional to the pulling velocity in the large pulling velocity regime, see eq.(2.30).

2.3 What's new

We propose two simple kinetic models, pulling with fixed force and pulling with fixed velocity to investigate the thickening behaviour. We find inertia is the mechanism for thickening in both cases. It can be determined by the ratio of the collision time scale over the velocity relaxation time scale, $t_c/\frac{m}{\gamma_0}$. The granular materials have quite small bare friction compared with the Brownian suspension, which is the origin of the apparent discrepancy between driven granular systems and Brownian ones under large pulling. However, these two models do not capture the thinning behaviour. Temperature and solvent friction may be non-trivial for the thinning, which will be discussed in the following chapters.

Chapter 3

Time scales picture of thinning and thickening

In the last chapter, we found that inertia causes thickening. To find a general picture including both thinning and thickening, here, we propose a three-time-scales picture (TTSP) to unify thinning and thickening and confirm it by a stochastic simulation. The results of chapter 3 and 4 are presented based on the pre-print [60].

3.1 Three-time-scales picture

The probe's friction arises from the drag of the solvent with friction coefficient γ_0 and the interaction with bath particles. Because fixed force pulling and fixed velocity pulling both show similar thinning and thickening behaviour, here let us consider the case of fixed velocity pulling for simplicity. Let us fix our frame in the probe. In the large pulling velocity regime, we found in our earlier paper [57] that inertia causes thickening by a simple kinetic theory.

Thickening occurs when the frequent probe-bath collisions dominate over the velocity damping of bath particles due to the solvent. The criterion of the thickening is $t_{col}/t_{damp} \ll 1$, where $t_{col} = l_0/u$ is the P-B collision time scale, and $t_{damp} = \gamma_0/m$ is the damping time scale of a bath particle.

Now let us consider thinning. In the small pulled velocity regime, the diffusion of bath particles may cause additional resistance. The corresponding diffusion time

scale is $t_{diff} = l_0^2/D$ with the diffusion coefficient $D = k_BT/\gamma_0$. The competition between the diffusion time scale and the damping time scale should cause thinning.

A unifying picture of thinning and thickening is that three time scales of bath particles are involved (see fig. 3.1.):

- diffusion time scale: $t_{diff} = R^2/D$, where $D = \frac{k_BT}{\gamma_0}$ is the diffusion coefficient with the solvent friction γ_0, R is the characteristic length scale (for hard sphere systems, it should be the center distance of the probe-bath particles contacting with each other). The corresponding diffusion velocity is $u_{diff} = R/t_{diff}$.
- damping time scale: $t_{damp} = m_b/\gamma_0$, where m_b is the mass of a bath particle. The damping velocity is $u_{damp} = R/t_{damp}$.
- collision time scale: $t_{col} = R/u$, where u is the pulling velocity. It characterizes the mean-free time between first and second P-B collisions without damping. The collision velocity is $u_{col} = R/t_{col} = u$.

The dominating time scales are controlled by the pulling velocity $\boldsymbol{u}$, which can be indicated by the Peclet number $Pe := u/u_{diff} = \frac{R\gamma_0}{k_BT}u$ and the Reynolds number $Re := u/u_{damp} = \frac{m_b}{R\gamma_0}u$. Different dominating time scales lead to different behaviour of the increased friction $\Delta\gamma_{eff} = \gamma_{eff} - \gamma_0$. In detail,

(i) when the pulling velocity is small enough that $Pe \ll 1$ and $Re \ll 1$, the diffusion dominates. $\Delta\gamma_{eff}$ arises from the diffusion of bath particles, which leads to a linear response regime.

(ii) As the pulling velocity is much larger than the diffusion velocity but still much smaller than the damping velocity, *i.e.* $Pe \gg 1$ and $Re \ll 1$, diffusion is unimportant, damping dominates. $\Delta\gamma_{eff}$ arises from the damping of bath particles, which leads to another linear response regime.

(iii) As the pulling velocity is even larger than the damping velocity, *i.e.* $Pe \gg 1$ and $Re \gg 1$, inertia dominates, $\Delta\gamma_{eff}$ arises from single P-B collision, which leads to a regime of increasing friction.

The plateau value of the linear response regime in (i) should be larger than the value in (ii), because diffusion causes larger friction in (i) compared to the one arising from the damping only in (ii). As a result, the crossover from (i) to (ii)

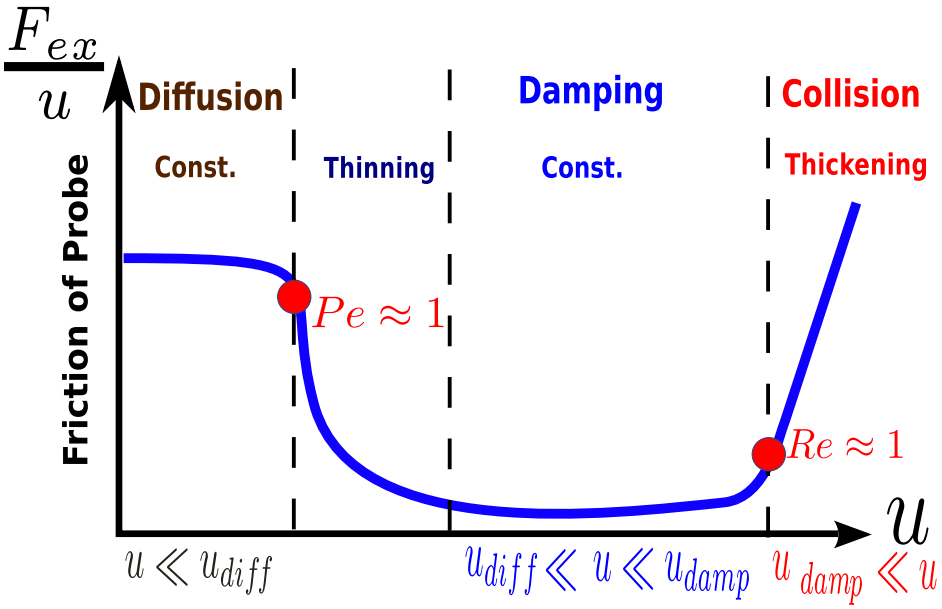

Figure 3.1: Sketch of the TTSP of thinning and thickening: the effective friction $\gamma_{eff} = F_{ex}/u$ vs. the pulling velocity u. Three time scales of bath particles are involved: diffusion, damping and single P-B collision, which lead to three friction behaviour: a high plateau regime, a low plateau regime, and an increasing friction regime, respectively. The pulling velocity controls which time scale dominates. The crossover from diffusion to damping causes thinning. Thickening starts from the crossover from damping to collision. The onsets of thinning and thickening are around $Pe := u/u_{diff} = \frac{R\gamma_0}{k_B T}u = 1$ and $Re := u/u_{damp} = \frac{m_b}{R\gamma_0}u = 1$, respectively.

causes thinning. And the crossover from (ii) to (iii) causes thickening. The starting points of thinning and thickening should be around $Pe = 1$ and $Re = 1$, respectively (see fig. 3.1).

3.2 Model

To test the TTSP, we consider the model of pulling a probe particle with fixed velocity embedded in a suspension of N identical bath particles in two dimensions. Because pulling with fixed force and pulling with fixed velocity behave similarly, both may show thinning and thickening [1], we choose the latter for simplicity. All particles are assumed to be smooth and elastic hard disks with the same radius r_0. The dynamics of a bath particle (labelled i) and of the probe (labelled p) obey the Langevin equations (3.1a) and (3.1b), respectively,

$$m_b \dot{\boldsymbol{v}}_i = -\gamma_0 \boldsymbol{v}_i + \boldsymbol{\xi}_i + \boldsymbol{F}_{i,col} \tag{3.1a}$$

$$0 = -\gamma_0 \boldsymbol{u} + \boldsymbol{\xi}_p + \boldsymbol{F}_{p,col} + \boldsymbol{F}_{ex} \tag{3.1b}$$

where m_b is the mass of a bath particle; $\boldsymbol{v}_i$ is the velocity of the i-th bath particle, $\boldsymbol{u}$ is the fixed pulling velocity of the probe; γ_0 is the friction coefficient (all particles have the same value due to $\gamma_0 \propto r_0\eta$; η is the solvent's viscosity.); $\boldsymbol{\xi}_k$ ($k = i$ or p) is a Gaussian random force satisfying the fluctuation-dissipation relation as discussed for the Langevin equation of the fixed force pulling, see (1.10). $\boldsymbol{F}_{i,col}$ (or $\boldsymbol{F}_{p,col}$) is the interaction force between particles; $\boldsymbol{F}_{ex}$ is the external pulling force on the probe only. Being different from the case of fixed force pulling, here the external force is not constant but fluctuating in time to keep the probe with fixed velocity. According to the equation of motion (EOM) (3.1b), the probe's increased friction $\Delta\gamma_{eff} := \gamma_{eff} - \gamma_0$ is

$$\Delta\gamma_{eff} = \left\langle F_{p,col} \right\rangle / u, \tag{3.2}$$

where $u, F_{ex}, F_{p,col}$ are absolute values of the corresponding vectors, and the random force has been averaged out: $\left\langle \boldsymbol{\eta}_p \right\rangle = 0$.

Obviously, the P-B interaction directly leads to the increased friction of the probe, while the bath-bath (B-B) particle interaction affects the probe's effective friction

[1] The effective friction of pulling with fixed velocity in general is larger than the one of pulling with fixed force as pointed out in [24] and further analysed in [25]

indirectly. *We omit the B-B interaction in our model* because 1) such interaction may not be necessary for thinning and thickening behaviour; 2) the omission itself should be valid in the low density limit. In addition, we set the mass of the probe as much heavier than the mass of a bath particle: $m_p \gg m_b$, so that in the coordinate of the probe, P-B collision just causes specular reflection of the bath particles, but affects little the probe's velocity.

Now the system of pulling a probe with fixed velocity $\boldsymbol{u}$ is equivalent to the system of a flow with velocity $-\boldsymbol{u}$ of a suspension of N non-interacting bath particles passing a fixed disk with radius $R = 2r_0$. The EOM of a bath particle (the index i is dropped) in the coordinate of the probe is

$$m_b\dot{\boldsymbol{v}} = -\gamma_0(\boldsymbol{v} + \boldsymbol{u}) + \boldsymbol{\xi} \tag{3.3a}$$

with the reflecting boundary condition (RBC)

$$\boldsymbol{v} = \boldsymbol{v} - (\boldsymbol{v} \cdot \boldsymbol{e}_n)\boldsymbol{e}_n \text{ for } |\boldsymbol{r}| = R, \tag{3.3b}$$

where $R = 2r_0$ is the contact distance between the probe and a bath particle, and $\boldsymbol{e}_n$ is the unit normal vector along the direction from the center of the probe to that of the bath particle colliding with it. Note that the P-B interaction term $\boldsymbol{F}_{i,col}$ in Eq.(3.1a) is mapped into the RBC (3.3b).

Being equivalent to its stochastic description Eq.(3.3), the probability description of a bath particle obeys the Fokker-Planck equation (FPE)

$$\partial_t P(\boldsymbol{r}, \boldsymbol{v}, t) = -\boldsymbol{v} \cdot \partial_r P + \frac{\gamma_0}{m_b}\partial_{\boldsymbol{v}} \cdot \left[(\boldsymbol{v} + \boldsymbol{u}) + \frac{k_B T}{m_b}\partial_{\boldsymbol{v}}\right] P, \tag{3.4a}$$

The corresponding RBC is

$$P(\boldsymbol{r}, \boldsymbol{v}, t) = P(\boldsymbol{r}, \boldsymbol{v} - (\boldsymbol{v} \cdot \boldsymbol{e}_n)\boldsymbol{e}_n, t) \text{ for } |\boldsymbol{r}| = R. \tag{3.4b}$$

In principle, the steady state equation ($\partial_t P = 0$) of the FPE (3.4a) can be solved with the RBC (3.4b). Then one can obtain the average collision force of N bath particles on the probe:

$$\left\langle \boldsymbol{F}_{p,col} \right\rangle = \int d\boldsymbol{v} \oint_{r=R} dl N P_{st}(\boldsymbol{r}, \boldsymbol{v}) \boldsymbol{v} \cdot (-\boldsymbol{e}_n) \Theta[\boldsymbol{v} \cdot (-\boldsymbol{e}_n)] \\ 2(-\boldsymbol{e}_n) m_b \boldsymbol{v} \cdot (-\boldsymbol{e}_n) \tag{3.5}$$

where P_{st} denotes the steady state distribution, $dlNP_{st}(\boldsymbol{r},\boldsymbol{v})\boldsymbol{v}\cdot(-\boldsymbol{e}_n)\Theta[\boldsymbol{v}\cdot(-\boldsymbol{e}_n)]$ is the density current of bath particles with velocity $\boldsymbol{v}$ passing through a small contact surface $dl\boldsymbol{e}_n$ ($\Theta(x)=1$ for $x\geq 0$;$\Theta(x)=0$ for $x\leq 0$), and $2(-\boldsymbol{e}_n)m_b\boldsymbol{v}\cdot(-\boldsymbol{e}_n)$ is the bath particles' momentum transferred to the probe due to single P-B collisions. Inserting Eq.(4.20) into Eq.(3.2), one obtains the effective friction γ_{eff}.

In practice, however, to analytically solve the FPE (3.4) is difficult due to the RBC (3.4b). Our strategy is to solve Eq.(3.4) by simulation of the stochastic process Eq.(3.3), because of its equivalence to the FPE (3.4) and simplicity.

3.3 Stochastic simulation

To calculate the effective friction, the stochastic dynamics simulation according to Eq.(3.3) is performed.

3.3.1 Wiener Process

The discrete form of the Gaussian random force is

$$\boldsymbol{\xi}=\sqrt{2\gamma_0 k_B T/h}(\xi_0^x,\xi_0^y), \tag{3.6}$$

where ξ_0^μ ($\mu\in x,y$) is the standard Gaussian random number of the probability distribution function as

$$P(\xi_0^\mu)=\frac{1}{\sqrt{2\pi}}\exp(-\frac{\xi_0^{\mu\,2}}{2}), \tag{3.7}$$

and h is the time step of the dynamics set to be $h=\frac{1}{2\gamma_0}$ for different solvent frictions. The box size is set to be $Lx\times Ly=20R\times 20R$ with periodic boundary conditions, which is large enough to suppress finite size effects. The mass of bath particles and the P-B contact distance are set to be unit values: $m_p=1$, $R=1$. The density of bath particles is also rescaled to unit value $n_0=1$, since it is not a control parameter in our model due to the assumption of non-interacting bath particles. The control parameters are the pulling velocity u, the solvent friction γ_0 and the temperature k_BT, which are applied to investigate the whole regime of different time scales.

3.3.2 Reflecting boundary condition

The RBC (3.3b) for the stochastic dynamics (3.3a) can be realized as follows: consider a P-B collision process in the coordinate of the probe. Before the collision at time $t = 0$, a bath particle is located at $\boldsymbol{x}_0$ with $|\boldsymbol{x}_0| \geq 1$, and ignoring the P-B collision, at time h, it would move into the P-B boundary $\boldsymbol{x}_1'$ with $|\boldsymbol{x}_1'| < 1$. Thus the average velocity during the time interval $\Delta t = h$ is

$$\boldsymbol{v}_0 = (\boldsymbol{x}_1' - \boldsymbol{x}_0)/h. \tag{3.8}$$

For small enough h, we can consider the velocity during the short time interval $[0, t^*]$ keeping constant value $\boldsymbol{v}_0$, where t^* is the collision time satisfying the geometry restriction (the bath particle should be located on the P-B contact surface) as indicated in the fig. 3.2.

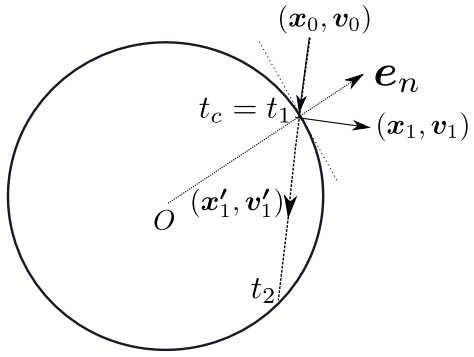

Figure 3.2: Sketch of simulation realization of reflecting boundary condition

$$|\boldsymbol{x}_0 + \boldsymbol{v}_0 t^*| = 1 \tag{3.9}$$

There are two roots of the above equation t_1, t_2[2] . We choose the smaller one, $t^* = t_1$ due to the real physics process. The collision point is

$$\boldsymbol{x}_c = \boldsymbol{x}_0 + \boldsymbol{v}_0 t^* = \boldsymbol{e}_n, \tag{3.10}$$

where $\boldsymbol{e}_n$ is the normal vector of the reflecting surface. The corresponding reflecting velocity and the position at time h are

$$\begin{aligned} \boldsymbol{v}_1 &= \boldsymbol{v}_0 - 2(\boldsymbol{v}_0 \cdot \boldsymbol{e}_n)\boldsymbol{e}_n \\ \boldsymbol{x}_1 &= \boldsymbol{x}_c + \boldsymbol{v}_1(h - t^*) \end{aligned} \tag{3.11}$$

[2]In 2D, the (3.9) is equivalent to $(x_0^x + v_0^x t^*)^2 + (x_0^y + v_0^y t^*) = 1$.

The transformed momentum of the bath particle due to the P-B collision is

$$\Delta I_b = m_b(\boldsymbol{v}_1 - \boldsymbol{v}_0) = -2m_b(\boldsymbol{v}_0 \cdot \boldsymbol{e}_n)\boldsymbol{e}_n \tag{3.12}$$

And the collision force acting on the probe is

$$\boldsymbol{F}_{p,col} = \Delta I_p/h = 2m_b(\boldsymbol{v}_0 \cdot \boldsymbol{e}_n)\boldsymbol{e}_n/h, \tag{3.13}$$

where we have applied the momentum conservation of the P-B system, i.e. $I_b + I_p = 0$.

Initially, bath particles are homogeneously distributed in space (the configuration is generated by uniform random numbers) with Maxwellian distributed velocities. Then the probe is pulled along the x direction with total running time $10R/u$, which ensures that the bath particles around the probe reach the steady state. After a transient time, the steady average P-B collision force is computed by detecting the bath particles passing through the boundary:

$$\left\langle \boldsymbol{F}_{p,col} \right\rangle = \frac{1}{\Delta t} \oint_{r=R} dl \int_0^{\Delta t} dt 2\big[m_p(-\boldsymbol{e}_n)\boldsymbol{v}(t) \cdot (-\boldsymbol{e}_n)\big]\Theta[\boldsymbol{v}(t) \cdot (-\boldsymbol{e}_n)], \tag{3.14}$$

which is the simulation realization of the collision force expressed in Eq. (4.20). The corresponding increased friction $\Delta\gamma_{eff}$ is obtained based on Eq. (3.2).

3.4 Result

Fig. 3.5 (a) shows the simulation result of the increased friction $\Delta\gamma_{eff}$ versus the pulling velocity u for different solvent frictions and temperatures, $\{\gamma_0 = 1000,\ k_BT = 1000, 100\}$ and $\{\gamma_0 = 100,\ k_BT = 100, 10, 0\}$. All plots, except for $\{\gamma_0 = 100,\ k_BT = 0\}$, exhibit linear response, thinning and thickening as expected by the TTSP. For the exception, only linear response and thickening occur, because no diffusion but only damping and collision time scales are involved.

Fig. 3.5 (b) [3] shows the rescaled increased friction $\Delta\gamma_{eff}/\gamma_0$ versus Peclet number, $Pe = u/u_{diff} = \frac{R\gamma_0}{k_BT}u$. In the small Pe regime $Pe < 1$, the diffusion time scale dominates, all plots coincide with each other in a plateau value. With increasing Pe, diffusion becomes less important, all plots start to decrease around

[3] Data set of $\{\gamma_0 = 100,\ k_BT = 0\}$ is not included in fig.3.5 (b), because $u_{diff} = 0$, no diffusion is involved.

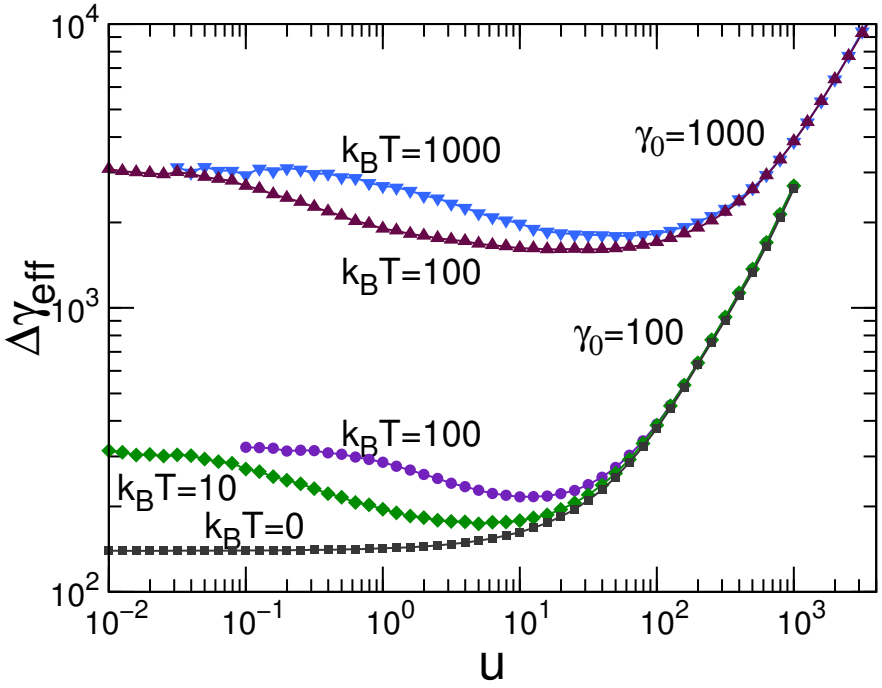

Figure 3.3: Simulation results for increased friction $\Delta\gamma_{eff}$ vs. pulling velocity u for different solvent frictions and temperatures. For a curve with fixed finite temperature and solvent friction, the increased effective friction exhibits linear response, thinning and thickening. For a curve with zero temperature, only linear response and thickening occur.

$Pe = 1$, which agrees with the TTSP. Between $Pe = 100$ and $Pe = 1000$, for $\{\gamma_0 = 1000,\ k_BT = 100\}$, the brown line, clearly there is a second plateau lower than the first one, being consistent with the TTSP. In addition, the length of the thinning regime varies for different data sets [4], because for the same Pe, the Re numbers can also be different. At $Pe = 100$, for $\{\gamma_0 = 1000,\ k_BT = 100\}$, $Re = 0.01$, bath particles are still in the damping dominated regime; for $\{\gamma_0 = 100,\ k_BT = 100\}$, $Re = 1$, bath particles are already in the inertia (thickening) regime, which suppresses the thinning process.

[4]The exception is that $\{\gamma_0 = 1000,\ k_BT = 1000\}$ and $\{\gamma_0 = 100,\ k_BT = 10\}$ coincide with each other in both fig. 3.5 (b) and (c), because for the same u, they have the same Pe and Re numbers.

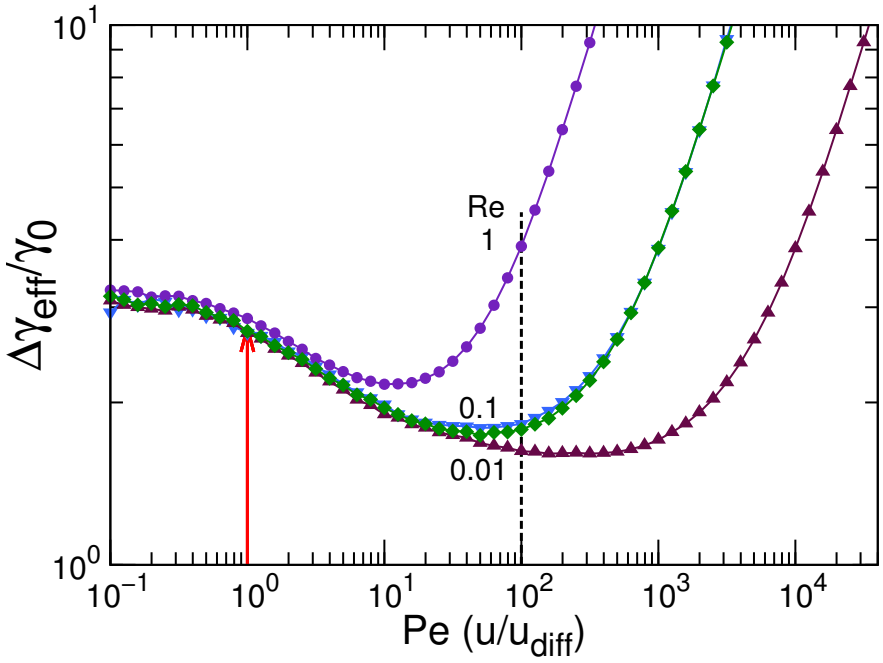

Figure 3.4: Rescaled increased friction $\Delta\gamma_{eff}/\gamma_0$ vs. Peclet number $Pe = u/u_{diff} = \frac{R\gamma_0}{k_BT}u$. The red arrow indicates $Pe = 1$. Different colors indicate different solvent frictions and temperatures as these are labelled in (a). At $Pe = 100$, for different solvent frictions and temperatures, the corresponding values of the Re number are indicated.

Fig. 3.5 (c) shows the rescaled increased friction $\Delta\gamma_{eff}/\gamma_0$ versus Reynolds number, $Re = u/u_{damp} = \frac{m_b}{R\gamma_0}u$. All plots start to converge around $Re = 1$, which agrees with the TTSP. In the small Re regime, for different plots, at $Re = 0.01$, the frictions increase with the decreasing Pe as indicated in the figure, which supports the TTSP that the diffusion causing larger friction than the one in the damping only regime $Pe \to \infty$. For $Re > 1$, i.e. the inertia regime, all plots coincide with each other and asymptotically tend to $\Delta\gamma_{eff} \propto u$, because the flux of bath particles passing through the P-B contact surface is $j \propto n_0 u$ with momentum transferring to the probe $p \propto mu$, and $\Delta\gamma_{eff} = \left\langle F_{col} \right\rangle / u = jp/u \propto u$.

In summary, the friction behaviour of different dominating time scales and of

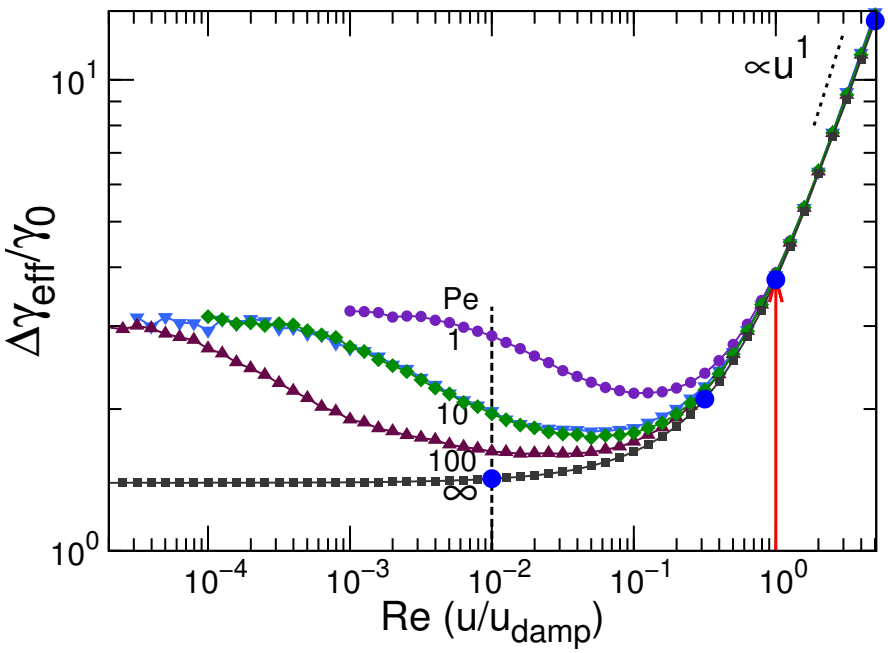

Figure 3.5: (c) Rescaled increased friction $\Delta\gamma_{eff}/\gamma_0$ vs. Reynolds number $Re = u/u_{damp} = \frac{m_b}{R\gamma_0}u$. The red arrow indicates $Re = 1$. At $Re = 100$, for different solvent frictions and temperatures, the corresponding values of the Pe number are indicated. On the plot of zero temperature, the gray line, four filled blue circles at $Re = 0.01,\ 0.3,\ 1,\ 5$ are drawn to compare with the corresponding streamlines in fig. 4.1.

the two starting points as shown in fig. 3.5, all agree quite well with the TTSP.

3.5 What's new

We propose a TTSP to unify thinning and thickening phenomena in active microrheology (see fig. 3.1), and confirm it by a model of pulling with fixed velocity. The simulation result (fig. 3.5), which is equivalent to the solution of the FPE (3.4) in the steady state, shows linear response, thinning and thickening. As far as we know, this is the first example demonstrating that both thinning and thickening can occur in non-interacting bath particles systems (only P-B interaction is

included), which indicates that the many body interaction is not necessary for thinning/thickening behaviour in the low density. Furthermore, as shown in fig. 3.5, the results of the onsets of the thinning and thickening being around $Pe = 1$ and $Re = 1$, respectively, and the friction behaviour in different time scale regimes, all agree with the TTSP.

According to the TTSP, thinning arises from the crossover from diffusion to damping, and thickening arises from inertia, starting from the crossover from damping to inertia and exiting in the whole regime when inertia is dominated. Note that diffusion was not involved in the experiments of pulling a single particle in static ($T = 0$) granular systems [13, 14], that's why thinning was not observed. For the same reason, it was not included in our earlier kinetic model [57]. Thickening was not found in colloidal systems [29, 30, 31, 24, 61], because they were limited to $Re \ll 1$ regime, where inertia is unimportant.

The TTSP should also be valid in the high density regime with dressed values of Pe and Re. B-B many body interaction increases the friction of a single bath particle, $\gamma_0' > \gamma_0$ (in the low density limit, γ_0' is just the solvent friction γ_0). Based on the TTSP, the onset of thinning $Pe = 1 \propto u\gamma_0'$ should shift to a smaller pulling velocity value, and that of the thickening $Re = 1 \propto u/\gamma_0'$ should shift to a larger value.

Chapter 4

Microscopic mechanism of thickening

In the last chapter, the three-time-scales picture (TTSP) was proposed to unify the thinning and the thickening behaviour of the probe with fixed velocity pulling. The time scales of bath particles, diffusion, damping and single probe-bath particles collision are the essential points. The pulling velocity controls the dominating time scales, leading to the thinning/thickening behaviour.

In this chapter, we will discuss the microscopic mechanism of the thickening, i.e. microscopically, how does inertia play a role. Furthermore, the validity of the assumption of the Maxwellian distribution will also be discussed.

4.1 Microscopic mechanism of thickening

Based on the TTSP, thickening is determined by the competition of the damping time scale and the single P-B collision time scale, which has nothing to do with the diffusion time scale. So let us consider the $T = 0$ limit, in which the diffusion time scale is ruled out, $Pe \to \infty$. The EOM of a bath particle in the coordinate of the probe, (3.3a), is reduced to

$$m_b \dot{\boldsymbol{v}} = -\gamma_0 \boldsymbol{v} - \gamma_0 \boldsymbol{u} \tag{4.1}$$

with the RBC (3.3b). Interestingly, such simple dynamics provides a clear mechanism of thickening: the crossover from creep flow in the low Re to gas-like (inertial) flow in high Re, as shown in fig. 4.1: the black curves are the stream-

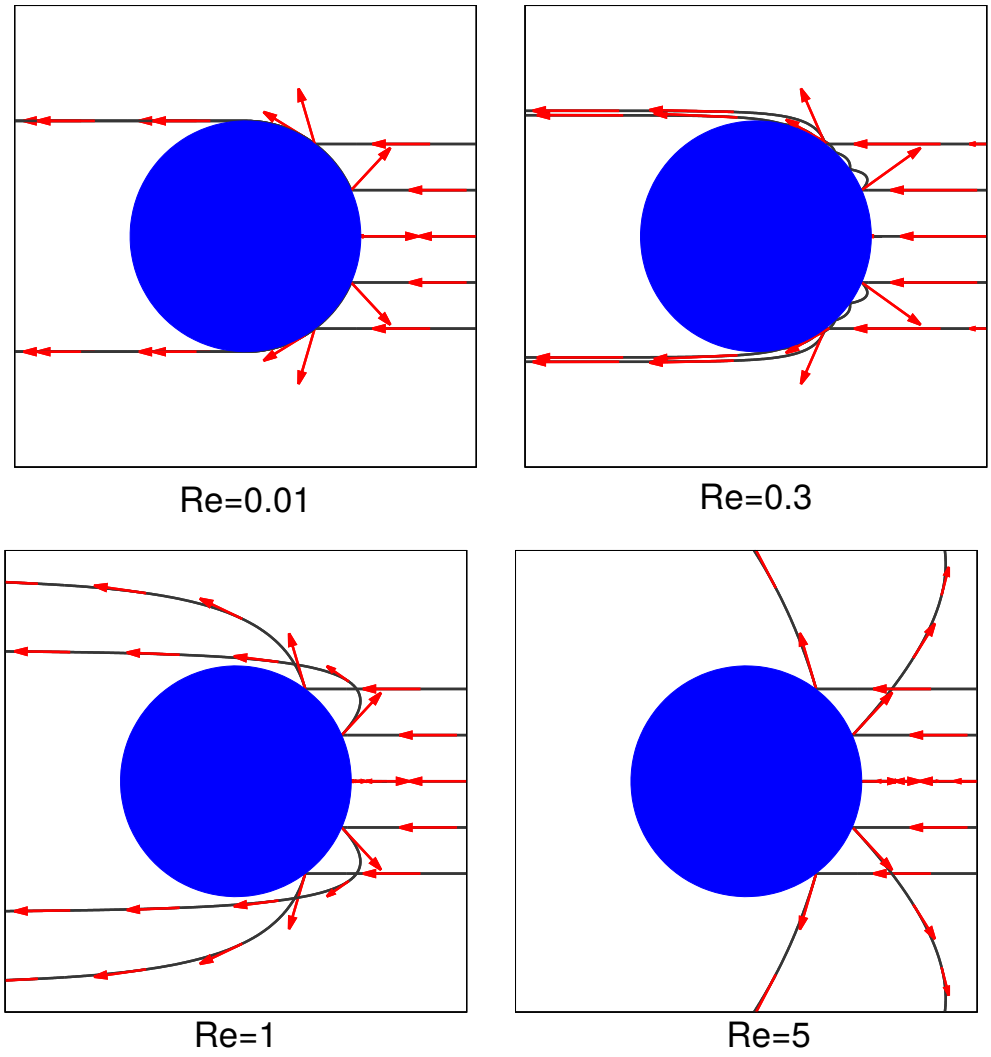

Figure 4.1: Streamlines of bath particles for different Reynolds numbers at the $T = 0$ limit. Red arrows are the velocity field (rescaled by the pulling velocity for comparison). For small Reynolds number, the bath particles behave like creep flow around the P-B contact surface. For high Reynolds number, they behave like a gas: after a single collision, the bath particles fly away. The corresponding increased frictions are indicated with four filled blue circles in the gray line in fig. 3.5(c).

lines of the bath particles in the frame of the probe; red arrows are the velocity field. Before any collision, bath particles are moving with a constant velocity $-\boldsymbol{u}$. Collision causes mirror-like reflection. The term $-\gamma_0 \boldsymbol{v}$ reduces the velocity, while $-\gamma_0 \boldsymbol{u}$ accelerates it. A loose criterion of single-collision-only should be $ut_{damp} \geq R$, *i.e.* $Re = u\frac{m_b}{R\gamma_0} \geq 1$. In the small Re limit, many P-B collisions occur and the bath particles tend to creep along the surface, see fig. 4.1 $Re = 0.01$, which causes $F_{col} \propto u$ and $\Delta\gamma_{eff} \propto u^0$, while in the large Re limit, the single collision causes $F_{col} \propto u^2$ and $\Delta\gamma_{eff} \propto u^1$.

Creep flow in low Reynolds number limit

Let us prove that in the limit $Re \to 0$, the P-B collision force is proportional to the pulling velocity of the probe

$$F_{col} \propto u. \tag{4.2}$$

A non-dimensional form of the EOM of the bath particles (4.1) is

$$\partial_{\bar{t}} \bar{\boldsymbol{v}} = -\bar{\boldsymbol{v}} - \bar{\boldsymbol{u}} \tag{4.3}$$

with the RBC (3.3b), where the EOM (4.1) is non-dimensionalized by setting $\bar{\boldsymbol{r}} = \boldsymbol{r}/R$, $\bar{t} = t/(m_b/\gamma)$ and $\bar{\boldsymbol{v}} = \boldsymbol{v}/(R\gamma/m_b)$. It means that the unit of length is the P-B contact surface radius R, the unit of time is the damping time of a bath particle m_b/γ, and the unit of velocity is the unit of length over the unit of time, $R\gamma/m_b$. By noting that $Re = u/u_{damp} = um_b/(R\gamma)$, the pulling velocity of the probe $\boldsymbol{u}$ is rescaled as $\bar{\boldsymbol{u}} = Re\boldsymbol{e}_u$. In the following, we omit the script "$-$" for simplicity.

Creep motion along a line

Consider a simple case that the P-B contact surface is just a straight line with length Δl. In the coordinate of the probe, the motion of a bath particle is illustrated in fig.4.2. It is convenient to separate the motion of the bath particle in the direction along the line $\boldsymbol{e}_x$ and in the direction being perpendicular to the line $\boldsymbol{e}_y$. Along the direction of the line $\boldsymbol{e}_x$, the bath particle always moves with a constant velocity

$$\boldsymbol{u}_x = u \sin\theta \boldsymbol{e}_x \tag{4.4}$$

(θ is the the angle between the incoming velocity $\boldsymbol{u}$ and the normal direction $\boldsymbol{e}_y$), because in this direction the effective force $\boldsymbol{G}_x = \boldsymbol{u}_x$ balances with the solvent

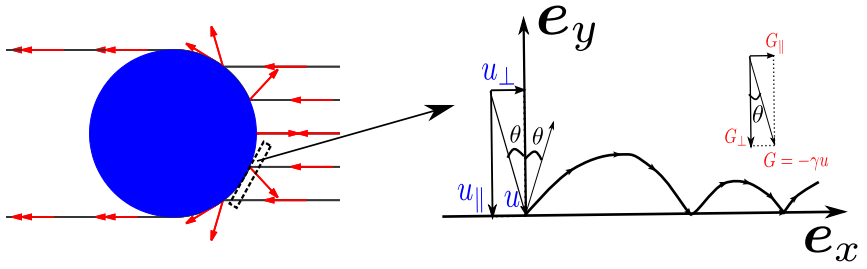

Figure 4.2: Sketch of the creep motion of a bath particle along the tangent plane to the P-B contact surface

drag force $\boldsymbol{F}_{drag,x} = -\boldsymbol{u}_x$, and no P-B collision occurs.

Now let us focus on the motion along the direction being perpendicular to the line $\boldsymbol{e}_y$. Denote the velocity of a bath particle just after the k-th collision with the line as $\boldsymbol{v}_k = (u\sin\theta\boldsymbol{e}_x, v_k^y\boldsymbol{e}_y)$. Obviously, $v_1^y = \boldsymbol{u}\cdot\boldsymbol{e}_y = u\cos\theta = u^y$. According to the EOM (4.3), between the k-th collision to the $k+1$ th collision, the velocity of the bath particle is

$$v_k^y(t) = (v_k^y + u^y)e^{-t} - u^y \tag{4.5}$$

and the displacement is

$$y_k(t) = \int_0^t v_k^y(t')dt' = (v_k^y + u^y)(1 - e^{-t}) - u^y t. \tag{4.6}$$

The time interval τ_k between the k-th collision and the $k+1$ th collision is determined by $y_k(\tau_k) = 0$, which equals

$$(1 + \widetilde{v}_k^y)(1 - e^{-\tau_k}) - \tau_k = 0 \tag{4.7}$$

with $\widetilde{v}_k^y = v_k^y/u^y$ and $\widetilde{v}_1^y = 1$. The solution of τ_k is

$$\tau_k = W_0\Big[-(1+\widetilde{v}_k^y)e^{-(1+\widetilde{v}_k^y)}\Big] + (1+\widetilde{v}_k^y), \tag{4.8}$$

where we have applied the Lambert-W function.[1] It is defined as the inverse function of $z(x) = xe^x$, i.e. $W(z) = x$. For $z \in \mathbb{R}$, there are two branches of the W function as shown in fig.4.3. The domain of $W_0(x)$ (the principle branch) is

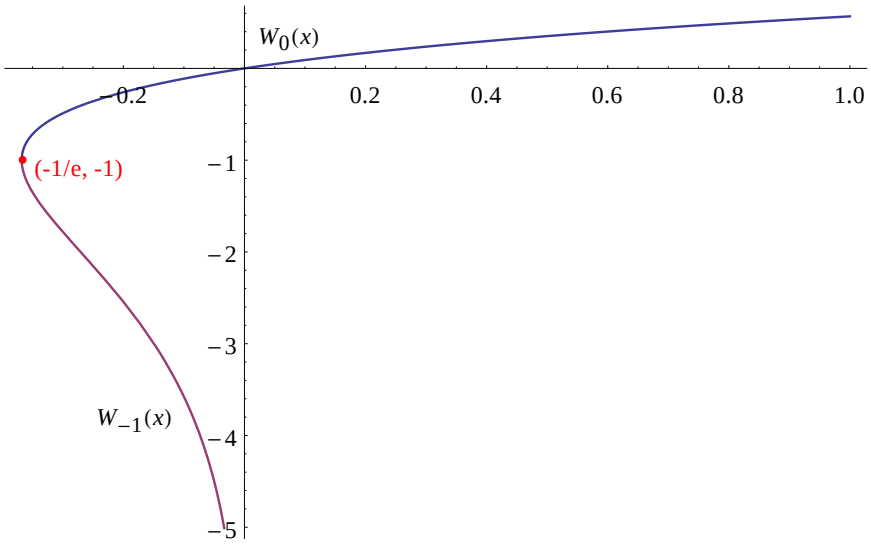

Figure 4.3: Two real branches of the Lambert W function. It is defined as the inverse of the function $z(x) = xe^x$.

$x \in [-1/e, \infty)$ and the domain of $W_{-1}(x)$ is $x \in (-1/e, 0)$.

The corresponding velocity of the bath particle just after the $(k+1)$-th collision is

$$v^y_{k+1} = -v^y_k(\tau_k) = -(v^y_k + u^y)e^{-\tau_k} + u^y \tag{4.9}$$

Inserting eqs. (4.7) and (4.8) into eq.(4.9), we get

$$\boxed{\widetilde{v}^y_{k+1} = W_0\Big[-(1+\widetilde{v}^y_k)e^{-(1+\widetilde{v}^y_k)}\Big] + 1, \quad \widetilde{v}^y_1 = 1}, \tag{4.10}$$

with $\widetilde{v}^y_k = v_k/u^y$. Eqs.(4.8) and (4.10) leads to

$$\boxed{\tau_k = \widetilde{v}^y_k + \widetilde{v}^y_{k+1}}. \tag{4.11}$$

Therefore, we can obtain the velocity of the bath particle after each collision by the recurrence formula (4.10) and the time interval by the relation (4.11).

[1] In general, the solution of equation $e^x = ax + b$ is $x = -W(-\frac{1}{a}e^{-\frac{b}{a})-\frac{b}{a}}$, which can be obtained by setting $y = ax + b$, the equation can be transformed to $-\frac{1}{a}e^{-\frac{b}{a}} = -\frac{y}{a}e^{-\frac{y}{a}}$, which results in $y = -aW(-\frac{1}{a}e^{-\frac{b}{a}})$ and the solution.

The incoming density current of the bath particles onto the line of length Δl is $j = n_0 u_\perp \Delta l$. The corresponding collision force is

$$F_{col}^{(1)} = j \cdot 2m_b u_\perp = 2n_0 \Delta l m_b u_\perp^2 \tag{4.12}$$

The average collision force of a bath particle except for the first incoming collision $F_{col}^{(1)}$ is

$$F_{col}^{k\geq 2} = \frac{\sum_{k=2}^{n} 2m_b(v_k)}{\sum_{k=1}^{n-1} \tau_k} = \frac{1 - v_1/s_n}{1 - v_n/s_n}\gamma u_\perp, \quad s_n = \sum_{k=1}^{n} v_k. \tag{4.13}$$

If the length Δl is long enough so that the collision time can be infinitely large, this results in $s_n \to \infty$ as $n \to \infty$. The steady state density of the bath particles is

$$n_{st} = n_0 \cot\theta, \tag{4.14}$$

which can be obtained by noting the balance of the incoming current and the outgoing current

$$n_{st} u_\parallel = j_{in} = j_{out} = n_0 u_\perp \tag{4.15}$$

Thus, the total collision force is

$$F_{col} = F_{col}^{1} + n_{st}\Delta l F_{col}^{k\geq 2} = 2n_0 \Delta l m_b u^2 + n_0 \Delta l \cot\theta \gamma u \tag{4.16}$$

which results in

$$F_{col} \propto u \tag{4.17}$$

in the small Re limit. Also note that in the large u limit, $F_{col} \propto u^2$. Therefore the crossover from the small u limit to the large u limit causes thickening of the probe's effective friction.

4.2 Density and velocity distributions

The TTSP tells us that thinning occurs when the damping time scale of the bath particle dominates its diffusion time scale, which can be indicated by the Peclet number $Pe := u_{damp}/u_{diff}$. In this section, we first have a detailed look at the density distribution for different Pe and then discuss the validity of the density distribution for calculation of the effective friction in different Re regimes.

4.2.1 Density distribution

Microscopically, it is convenient to compare the behaviour of bath particles in different Pe regimes by computing the pair distribution function $g(\boldsymbol{r})$, which is the normalized number density of bath particles in the coordinate of the probe

$$g(\boldsymbol{r}) = n(\boldsymbol{r})/n_0 = V \int d\boldsymbol{v}\, p(\boldsymbol{r}, \boldsymbol{v}) \tag{4.18}$$

where V is the volume of bath particles (for 2d it is the area) , $n_0 = N/V$ is the average number density of the bath particles, and $p(\boldsymbol{r}, \boldsymbol{v})$ is the steady state probability density of a bath particle appearing relative to the probe at position $\boldsymbol{r}$ with velocity $\boldsymbol{v}$.

Fig. 4.4 shows the simulation result $g(\boldsymbol{r})$ for different Pe numbers. For small Pe numbers $Pe = 0.1, 1$, bath particles are both built up in front and left behind of the probe, *i.e.* the diffusion dominating regime. As Pe is quite large, $Pe = 10, 100$, only a thin layer of bath particles build in front but no particles are left behind in a long tail region of the probe, which means that the diffusion is ignorable. The observation that diffusion dominates in the small Pe and is unimportant for large Pe, is consistent with the TTSP.

4.2.2 Velocity distribution

Does the pair distribution function contain enough information to calculate the effective friction?

If the velocity of bath particles is Maxwellian distributed, so the PDF of a bath particle is $f_{eq}(\boldsymbol{v}) = \big(\frac{1}{\sqrt{2\pi}v_{th}}\big)^d e^{-\frac{\boldsymbol{v}\cdot\boldsymbol{v}}{2v_{th}^2}}$ with thermal velocity $v_{th} = \sqrt{k_B T/m_b}$, then the total probability can be separated into

$$p(\boldsymbol{r}, \boldsymbol{v}) = V^{-1} g(\boldsymbol{r}) \big(\frac{1}{\sqrt{2\pi}v_{th}}\big)^d e^{-\frac{\boldsymbol{v}\cdot\boldsymbol{v}}{2v_{th}^2}} \tag{4.19}$$

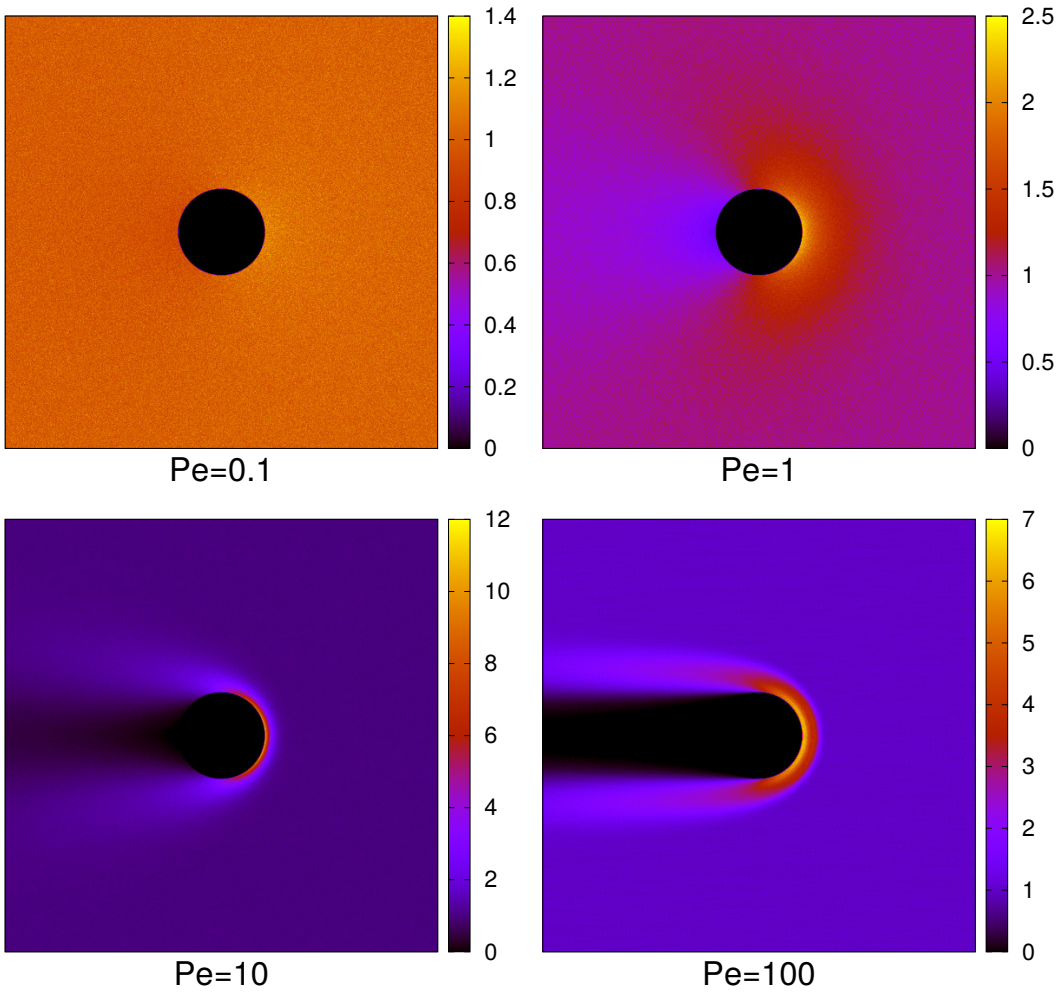

Figure 4.4: Pair distribution function $g(\boldsymbol{r})$ of bath particles in the frame of the probe for different Peclet numbers. The solvent friction is $\gamma_0 = 100$ and the temperature is $k_B T = 100$.

The collision force in eq. (3.5) can be reduced as

$$\begin{aligned}\left\langle \boldsymbol{F}_{p,col} \right\rangle &= -2n_0 m_p \oint_{r=R} dl \boldsymbol{e}_n g(\boldsymbol{r}) \Big(\frac{1}{2\pi v_{th}^2} \Big) \int d\boldsymbol{v} e^{-\frac{\boldsymbol{v}\cdot\boldsymbol{v}}{2v_{th}^2}} (\boldsymbol{v}\cdot\boldsymbol{e}_n)^2 \Theta(-\boldsymbol{v}\cdot\boldsymbol{e}_n) \\ &= -2n_0 m_p \oint_{r=R} dl \boldsymbol{e}_n g(\boldsymbol{r}) \Big(\frac{1}{2\pi v_{th}^2} \Big) \int_{-\infty}^{\infty} dv_t e^{-\frac{v_t^2}{2v_{th}^2}} \int_{-\infty}^{0} e^{-\frac{v_n^2}{2v_{th}^2}} v_n^2 \\ &= -n_0 m_p v_{th}^2 \oint_{r=R} dl \boldsymbol{e}_n g(\boldsymbol{r})\end{aligned} \tag{4.20}$$

Thus the collision force is reduced to

$$\boxed{\left\langle \boldsymbol{F}_{p,col} \right\rangle = -n_0 k_B T \oint_{r=R} dl \boldsymbol{e}_n g(\boldsymbol{r}) = \oint_{r=R} dl(-\boldsymbol{e}_n) n(\boldsymbol{r}) k_B T} \tag{4.21}$$

which means that under the assumption of the Maxwellian distribution, the collision force is just ideal gas like. The only difference is that the pressure of bath particles typically should not be isotropically distributed around the probe, due to anisotropy of the density distribution [2] : $\boldsymbol{\Pi}^{probe}_{pressure}(\boldsymbol{r}) = -\boldsymbol{e}_n n(\boldsymbol{r}) k_B T$. (Recall that $\boldsymbol{\Pi}^{ideal\,gas}_{pressure} = -\boldsymbol{e}_n n_0 k_B T$ with $n_0 = N/L^d$)

For a given position $\boldsymbol{r} = R\boldsymbol{e}_n$, after averaging out the velocity distribution, the flux of colliding particles passing through the surface $dl\boldsymbol{e}_n$ is

$$\begin{aligned} j_N(\boldsymbol{r}) &= \int d\boldsymbol{v} N P(\boldsymbol{r},\boldsymbol{v}) \boldsymbol{v}\cdot(-\boldsymbol{e}_n)\Theta(-\boldsymbol{v}\cdot\boldsymbol{e}_n) \\ &= -Ng(\boldsymbol{r}) \int d\boldsymbol{v} \Big(\frac{1}{2\pi v_{th}^2} \Big) e^{-\frac{\boldsymbol{v}\cdot\boldsymbol{v}}{2v_{th}^2}} \boldsymbol{v}\cdot\boldsymbol{e}_n \Theta(-\boldsymbol{v}\cdot\boldsymbol{e}_n) \\ &= -Ng(\boldsymbol{r}) \Big(\frac{1}{2\pi v_{th}^2} \Big) \int_{-\infty}^{\infty} dv_t e^{-\frac{v_t^2}{2v_{th}^2}} \int_{-\infty}^{0} e^{-\frac{v_n^2}{2v_{th}^2}} v_n dv_n \\ &= Ng(\boldsymbol{r}) \frac{v_{th}}{\sqrt{2\pi}} \end{aligned} \tag{4.22}$$

Comparing it with Eq. (4.21), we obtain

$$\left\langle \boldsymbol{F}_{col} \right\rangle = \sqrt{2\pi} m_b v_{th} \oint_{r=R} dl \boldsymbol{e}_n j_N(\boldsymbol{r}) \tag{4.23}$$

[2] The number density of bath particles is $n(\boldsymbol{r}) \equiv N \int d\boldsymbol{v} P(\boldsymbol{r},\boldsymbol{v}) = Ng(\boldsymbol{r})$.

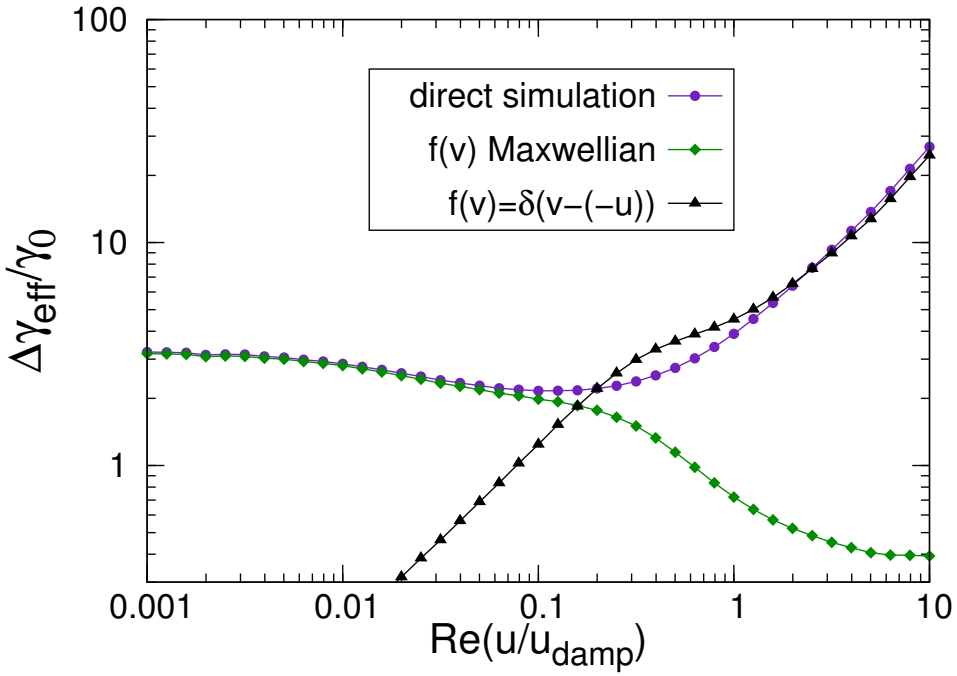

Figure 4.5: Increased effective friction calculated from different methods: the violet line is the direct simulation result. The green and the black lines are calculated by inputting $g(\boldsymbol{r})$ from the simulation associated with Maxwellian distribution and delta distribution of velocity parts, respectively.

which is identical to the expression in ref. [24].

If the velocity is delta distributed, $f(\boldsymbol{v}) = \delta\big(\boldsymbol{v} - (-\boldsymbol{u})\big)$, the collision force in Eq. (4.20) is reduced to

$$\left\langle \boldsymbol{F}_{p,col} \right\rangle = -n_0 2 m_b \oint_{r=R} dl \boldsymbol{e}_n g(\boldsymbol{r})(\boldsymbol{u}\cdot\boldsymbol{e}_n)^2 \Theta[\boldsymbol{u}\cdot\boldsymbol{e}_n] \tag{4.24}$$

Inputting $g(\boldsymbol{r})$ from the simulation into Eq.(4.21) and Eq.(4.24), respectively, we obtain two increased effective frictions, the green line and black line, respectively, as indicated in fig. 4.5. Comparing them with the direct simulation result, the violet line (see fig. 4.5), one can conclude that for the calculation of the friction, the pair distribution function still works, but the proper velocity distributions should

be input, according to different Re regimes: Maxwellian distribution in low Re and the delta distribution $\delta\big(\boldsymbol{v}-(-\boldsymbol{u})\big)$ in high Re.

4.2.3 Why does Maxwellian work or not?

Based on the microscopic picture of Re (fig. 4.1), the fact that the Maxwellian distribution works in low Re but fails in high Re can be understood. Let us consider the $Pe \gg 1$ limit, where a bath particle moves with velocity $-\boldsymbol{u}$ relative to the probe before any P-B collision [3]. Re determines whether the solvent plays a role during P-B collisions.

- If $Re \ll 1$, damping dominates, the incoming velocity $-\boldsymbol{u}$ of the bath particle is quickly erased due to the damping and agitation processes by the solvent at the beginning of a few P-B collisions. In the following multiple P-B collisions, the bath particle transfers the thermalized velocities to the probe. That's why the Maxwellian distribution works in this limit.
- If $Re \gg 1$, inertia dominates, the P-B collision happens only once. The bath particle's velocity transferred to the probe is exactly the incoming velocity $-\boldsymbol{u}$, which has nothing to do with the solvent. Thus, instead of the Maxwellian, the delta distribution $\delta\big(\boldsymbol{v}-(-\boldsymbol{u})\big)$ works in this limit.

4.3 What's new

In this chapter, the microscopic mechanisms of thickening is obtained. When $Re \ll 1$, damping dominates, the constant friction comes from creep flow, the bath particles collide with the probe and then creep around it; when $Re \gg 1$, inertia dominates, the increasing friction comes from the single P-B collisions.

Based on the picture of bath particles in different Re regimes, the applicability of the Maxwellian distribution can also be understood, which explains the reason why thickening is not observed in the over-damped dynamics (with hydrodynamical interaction). See for instance, Smolukwuski equation in theory [24] and Stokes dynamics in simulation [31].

[3] Indeed, before any P-B collision, the motion of a bath particle is determined by Pe only. It has nothing to do with Re.

Chapter 5

Pulling in High Density: Mode-coupling Theory

In the last chapter, we discussed the thinning and the thickening behaviour of the probe's friction in the low density limit, in which only the interactions between the probe and the bath particles are included, but not the interaction between bath particles. Under this two-body assumption, we find that the dominating time scales of bath particles are essential for the thinning and the thickening behaviour. The thinning depends on the Peclet number $Pe = u/u_{diff}$, and the thickening depends on the Reynolds number $Re = u/u_{damp}$. The corresponding thinning and thickening onsets are around $Pe = 1$ and $Re = 1$, respectively.

In high density, as the probe is pulled under a small force, the responding effective friction of it should indicate the rigidity of the system (because of crowding) close to the quasi-equilibrium state, i.e. the linear response regime. As the pulling force increases, the probe is driven away from the equilibrium, follows a thinning and a thickening regime.

The linear response and thinning regimes have been captured by the non-equilibrium MCT [27, 47]. The motivation here is that we want to extend the non-equilibrium MCT including the regime of thickening. We apply the MCT combined with a generalized Green-Kubo formula to calculate the effective friction of the probe in high density. There are three steps in the standard MCT method:

- applying the projection operator to get a reduced dynamics equation with memory term, the Mori-Zwanzig (MZ) equation

- applying the factorization approximation in the memory term to obtain a closed MCT equation.

- Inputting the static structure factor or reducing to a schematic model to numerically solve the MCT or the schematic-MCT equation.

5.1 Generalized Green-Kubo formula

We choose the FPE (1.13) to describe the microrheology of pulling with fixed force, which is equivalent to the under-damped LE (1.8). Being different from the Smoluchowski dynamics applied in the refs. [27, 47], where operation is only in position space, in the above FP dynamics, operation in velocity space is also included, due to the under-damped property of the granular systems. The advantage of this choice is that under the FPE, the dynamics of colloidal particles (large friction) and granular particles (low friction) can be uniformly described. The aimed average velocity of the probe is

$$\left\langle \boldsymbol{v}_s(t) \right\rangle = \int d\Gamma P(\Gamma, t) \boldsymbol{v}_s. \tag{5.1}$$

In the following, we will first introduce the ITT to reformulate the average velocity (5.1) by the velocity autocorrelation function (VACF), and then map the VACF to the density auto-correlator of the probe (DACP).

5.1.1 General formalism and proof

The ITT provides an exact formula for the average of an arbitrary response phase variable to external driving at a given time.

The formula of it is Eq. (5.8). Here we give the proof based on the derivation in ref. [47]. According to the definition, the average of a phase space variable A at time t is

$$\left\langle A \right\rangle(t) = \int d\Gamma P(\Gamma, t) A(\Gamma) \tag{5.2}$$

Assuming the evolution of the PDF satisfies

$$\partial_t P(\Gamma, t) = \Omega(\Gamma) P(\Gamma, t), \tag{5.3}$$

it has a formal solution

$$P(\Gamma, t) = e^{\Omega(\Gamma)t} P(\Gamma, 0). \tag{5.4}$$

Inserting eq.(5.4) into (5.2) and taking the derivative of both sides with respect to t, we obtain

$$\partial_t \Big\langle A \Big\rangle(t) = \int d\Gamma \Big[e^{\Omega(\Gamma)t} \Omega P(\Gamma, 0) \Big] A(\Gamma). \tag{5.5}$$

Correspondingly,

$$\Big\langle A \Big\rangle(t) = \Big\langle A \Big\rangle(0) + \int_0^t dt' \int d\Gamma \big[\Omega(\Gamma) P(\Gamma, 0) \big] e^{\mathcal{L}t'} A(\Gamma), \tag{5.6}$$

where we have defined the self conjugate operator $\mathcal{L}$ of Ω through

$$\int d\Gamma \Big[\Omega X(\Gamma) \Big] Y(\Gamma) = \int d\Gamma X(\Gamma) \Big[\mathcal{L} Y(\Gamma) \Big], \tag{5.7}$$

X, Y are arbitrary phase space variables. To further simplify, if the system is initially in equilibrium $P(\Gamma, t) = P_{eq}(\Gamma)$ and the probability operator can be separated as $\Omega = \Omega_0 + \Omega_{ex}$ satisfying $\Omega_0 P_{eq} = 0$, then we have

$$\boxed{\Big\langle A \Big\rangle(t) = \Big\langle A \Big\rangle(0) + \int_0^t dt' \int d\Gamma \big[\Omega_{ex}(\Gamma) P_{eq} \big] e^{\mathcal{L}t'} A(\Gamma)} \tag{5.8}$$

which is the so-called ITT. Noting that replacing $\Omega \to \Omega_0$ in the definition of (5.7), the dynamical operator will be correspondingly changed, denoted as $\mathcal{L} \to \mathcal{L}_{eq}$. The changing $\mathcal{L} \to \mathcal{L}_{eq}$ in the ITT is the famous Green-Kubo formula [62, 63] . For this reason, the ITT is also called a generalized Green-Kubo formula. An important feature of this generalization is that in the ITT, the formula is exact even for the non-linear regime, while the GK formula is valid in the linear response (small perturbation) only.

5.1.2 Application to fixed force pulling

Now let us apply the ITT to the fixed force pulling to calculate the effective friction. The aimed response variable is the velocity of the probe, $A = \boldsymbol{v}_s$. According to Eq. (1.13), the external phase-space operator for the FP dynamics is

$$\Omega_{ex} = -\frac{\boldsymbol{F}_{ex}}{m} \cdot \partial_{\boldsymbol{v}_s} \tag{5.9}$$

Initially, the system is in the equilibrium state with distribution function

$$P_{eq}(\Gamma) = \frac{1}{Z} e^{-H(\Gamma)/k_B T} \tag{5.10}$$

where $Z = \int d\Gamma e^{-H(\Gamma)/k_B T}$ is the normalization factor of the PDF, $H(\Gamma) = \frac{1}{2} m \boldsymbol{v}_i \cdot \boldsymbol{v}_i + \sum_{i<j} \mathcal{U}(\boldsymbol{r}_i, \boldsymbol{r}_j)$ is the Hamiltonian of the N-particle system without external pulling, and $\mathcal{U}(\boldsymbol{r}_i, \boldsymbol{r}_j)$ is the potential energy between particle i and j. Inserting Eqs. (5.9) and (5.10) into the ITT (5.8) and choosing the velocity of the probe in time, $\boldsymbol{v}_s(t)$, as our response variable, we get

$$\Big\langle \boldsymbol{v}_s(t) \Big\rangle = \frac{\boldsymbol{F}_{ex}}{k_B T} \cdot \int_0^t dt' \int d\Gamma P_{eq}(\Gamma) \boldsymbol{v}_s e^{\mathcal{L}_{FP} t'} \boldsymbol{v}_s = \frac{\boldsymbol{F}_{ex}}{k_B T} \cdot \int_0^t dt' \Big\langle \boldsymbol{v}_s \boldsymbol{v}_s(t') \Big\rangle_{eq} \tag{5.11}$$

where the subscript eq denotes that the average is under the equilibrium distribution P_{eq}. The time dependent average velocity now is connected to the integral of the velocity autocorrelation function. Symmetry of the system (the Hamiltonian) tells us only the velocity average along the pulling direction is nonzero. Thus the above formula can be simplified to

$$\boxed{\Big\langle \boldsymbol{v}_s(t) \Big\rangle = \frac{\boldsymbol{F}_{ex}}{k_B T} \int_0^t dt' \Big\langle v_s^z e^{\mathcal{L}_{FP} t'} v_s^z \Big\rangle_{eq}} \tag{5.12}$$

where we have choose the z axis along the pulling force $\boldsymbol{F}_{ex}$.

Note that the FP operator depends on the force, i.e. $\mathcal{L}_{FP} = \mathcal{L}_{FP}(\boldsymbol{F}_{ex})$. Therefore, in general, the relation between the external driving $\boldsymbol{F}_{ex}$ and the response average velocity $\Big\langle \boldsymbol{v}_s \Big\rangle$ is non-linear. While in the conventional GKF, $\mathcal{L}_{FP}$ is independent of the pulling force, the response velocity depends linearly on the external force, which is valid in the regime of small pulling force only.

5.1.3 Mapping ITT to the density correlator

The ITT expression of the average velocity eq. (5.12) is exact but lacks practical application. To proceed, let us connect the VACF to the self-density autocorrelator, and treat the latter by the standard MCT technique.

Density and current

Let us introduce the density of the probe particle and the bath particles in real space and its Fourier transform

$$\begin{aligned} \rho^s(\boldsymbol{r}) &= \delta(\boldsymbol{r}-\boldsymbol{r}_s), \quad \rho^s_{\boldsymbol{q}} = \int \rho^s(\boldsymbol{r}) e^{i\boldsymbol{q}\cdot\boldsymbol{r}_s} d\boldsymbol{r}_s = e^{i\boldsymbol{q}\cdot\boldsymbol{r}_s} \\ \rho(\boldsymbol{r}) &= \sum_{k=1}^{N} \delta(\boldsymbol{r}-\boldsymbol{r}_k), \quad \rho_{\boldsymbol{q}} = \int \rho(\boldsymbol{r}) e^{i\boldsymbol{q}\cdot\boldsymbol{r}} d\boldsymbol{r} = \sum_{k=1}^{N} e^{i\boldsymbol{q}\cdot\boldsymbol{r}_k} \end{aligned} \tag{5.13}$$

where $\rho^s(\boldsymbol{r})$ and $\rho(\boldsymbol{r})$ denote the number density of the probe and the bath particles in position space, and $\rho^s_{\boldsymbol{q}}$ and $\rho_{\boldsymbol{q}}$ denote the number density of them in Fourier space, respectively. Note that the probe particle is not included in the density expression of the bath particles. Being different from ref. [27, 47], our system is not overdamped, so here we also need to introduce the density current of the probe and the bath particles

$$\begin{aligned} \boldsymbol{j}^s(\boldsymbol{r}) &= \boldsymbol{v}_s \rho^s(\boldsymbol{r}), \quad \boldsymbol{j}^s_{\boldsymbol{q}} = \int \boldsymbol{j}^s(\boldsymbol{r}) e^{i\boldsymbol{q}\cdot\boldsymbol{r}_s} d\boldsymbol{r}_s = \boldsymbol{v}_s e^{i\boldsymbol{q}\cdot\boldsymbol{r}_s} \\ \boldsymbol{j}(\boldsymbol{r}) &= \sum_{k=1}^{N} \boldsymbol{v}_k \delta(\boldsymbol{r}-\boldsymbol{r}_k), \quad \boldsymbol{j}_{\boldsymbol{q}} = \int \boldsymbol{j}(\boldsymbol{r}) e^{i\boldsymbol{q}\cdot\boldsymbol{r}} d\boldsymbol{r} = \sum_{k=1}^{N} \boldsymbol{v}_k e^{i\boldsymbol{q}\cdot\boldsymbol{r}_k} \end{aligned} \tag{5.14}$$

Typically, we will use the current along the vector $j^s_{\boldsymbol{q}_L} = \hat{\boldsymbol{q}} \cdot \boldsymbol{j}^s_{\boldsymbol{q}}$ and $j_{\boldsymbol{q}_L} = \hat{\boldsymbol{q}} \cdot \boldsymbol{j}_{\boldsymbol{q}}$, where $\hat{\boldsymbol{q}} = \boldsymbol{q}/|\boldsymbol{q}|$ is the unit vector of the wave vector $\boldsymbol{q}$.

Connection between the self-density correlator and the average velocity

For convenience, let us apply the Dirac notation to the phase space variables:

$$\begin{aligned} \Big|A\Big\rangle &:= A(\Gamma) \\ \Big\langle A\Big| &:= A^*(\Gamma) \\ \Big\langle A\Big|B\Big\rangle &:= \int A^*(\Gamma) B(\Gamma) P_{eq}(\Gamma) d\Gamma \end{aligned} \tag{5.15}$$

The autocorrelation function of a phase space variable is

$$\Big\langle A\Big|A(t)\Big\rangle := \int A^*(\Gamma_0) A(\Gamma(t)) P_{eq}(\Gamma_0) d\Gamma_0 = \int A^*(\Gamma_0) A(\Gamma_0, t) P_{eq}(\Gamma_0) d\Gamma_0, \tag{5.16}$$

where $A(\Gamma_0)$ is the value of A at the initial point Γ_0 (* denotes its conjugate), $A(\Gamma(t)) = A(\Gamma_0, t)$ is the value of A at point $\Gamma(t)$ with the same initial point Γ_0.

In particular, we are interested in the DACP defined as

$$\phi^s_{\boldsymbol{q}}(t) := \left\langle \rho^s_{\boldsymbol{q}} \middle| \rho^s_{\boldsymbol{q}}(t) \right\rangle = \left\langle e^{i\boldsymbol{q}\cdot[\boldsymbol{r}_s(t)-\boldsymbol{r}_s]} \right\rangle_{eq} = \int e^{i\boldsymbol{q}\cdot[\boldsymbol{r}_s(t,\Gamma_0)-\boldsymbol{r}_s(\Gamma_0)]} P_{eq}(\Gamma_0) d\Gamma_0 \tag{5.17}$$

Note that $\mathcal{L}_{FP}\rho^s_{\boldsymbol{q}}(t) = \partial_t \rho^s_{\boldsymbol{q}}(t) = i\boldsymbol{q}\cdot\boldsymbol{v}_s\rho^s_{\boldsymbol{q}}(t) = iqv^s_{\boldsymbol{q}_L}\rho^s_{\boldsymbol{q}}(t)$, where we denote the velocity along the wave vector $\boldsymbol{q}$ as $\boldsymbol{e}_{\boldsymbol{q}}\cdot\boldsymbol{v}_s = v^s_{\boldsymbol{q}_L}$, $\boldsymbol{e}_{\boldsymbol{q}}$ is the unit vector of $\boldsymbol{q}$ and q is the absolute value of it. Conveniently, let us choose the wave-vector along the direction of the pulling force, $\boldsymbol{e}_{\boldsymbol{q}} = \boldsymbol{e}_{\boldsymbol{F}_{ex}}$. Thus

$$\begin{aligned} \mathcal{L}_{FP}\rho^s_{\boldsymbol{q}}(t) &= iqv^z_s\rho^s_{\boldsymbol{q}}(t) \\ \mathcal{L}^\dagger_{FP}\rho^s_{\boldsymbol{q}}(t) &= -(iq + \frac{F_{ex}}{k_BT})v^z_s\rho^s_{\boldsymbol{q}}(t) \end{aligned} \tag{5.18}$$

where we have applied the self- adjoint operator of $\mathcal{L}_{FP}$, see (A.13), in the second equation. Correspondingly,

$$\begin{aligned} \ddot{\phi}^s_{\boldsymbol{q}}(t) &= \left\langle \rho^s_{\boldsymbol{q}} \middle| e^{\mathcal{L}_{FP}t}\mathcal{L}^2_{FP} \middle| \rho^s_{\boldsymbol{q}} \right\rangle = \left\langle \mathcal{L}^\dagger_{FP}\rho^s_{\boldsymbol{q}} \middle| e^{\mathcal{L}_{FP}t} \middle| \mathcal{L}_{FP}\rho^s_{\boldsymbol{q}} \right\rangle \\ &= (-q^2 + iq\frac{F_{ex}}{k_BT})\left\langle v^z_s\rho^s_{\boldsymbol{q}} \middle| e^{\mathcal{L}_{FP}t} \middle| v^z_s\rho^s_{\boldsymbol{q}} \right\rangle. \end{aligned} \tag{5.19}$$

Note that $\rho^s_{\boldsymbol{q}} = e^{i\boldsymbol{q}\cdot\boldsymbol{r}_s} \to 1$ as $q \to 0$. Therefore the VACF is

$$\left\langle v^z_s \middle| e^{\mathcal{L}_{FP}t} \middle| v^z_s \right\rangle = \lim_{q\to 0} \frac{k_BT\ddot{\phi}^s_{\boldsymbol{q}}(t)}{iqF_{ex}} \tag{5.20}$$

Inserting (5.20) into (5.12), we get the average velocity expressed by the self-density autocorrelator as follows

$$\boxed{\left\langle v^z_s(t) \right\rangle = \lim_{q\to 0}\int_0^t \frac{\ddot{\phi}^s_{\boldsymbol{q}}(t')}{iq}dt' = \lim_{q\to 0}\frac{\dot{\phi}^s_{\boldsymbol{q}}(t)}{iq}} \tag{5.21}$$

where we have used the property $\dot{\phi}^s_{\boldsymbol{q}}(0) = 0$.

An alternative derivation

Note that the time derivative of the DACP is

$$\dot{\phi}^s_{\boldsymbol{q}}(t) = i\boldsymbol{q}\cdot\left\langle \boldsymbol{v}_s(t)e^{i\boldsymbol{q}\cdot[\boldsymbol{r}_s(t)-\boldsymbol{r}_s]}\right\rangle = iq\int v^z_s(t,\Gamma_0)e^{iq[r^z_s(t,\Gamma_0)-r^z_s]}P_{eq}(\Gamma_0)d\Gamma_0, \tag{5.22}$$

where we have chosen the wave-vector $\boldsymbol{q}$ along z. Correspondingly,

$$\left\langle v^z_s\right\rangle = \lim_{q\to 0}\frac{\dot{\phi}^s_{\boldsymbol{q}}(t)}{iq} \tag{5.23}$$

which gives the same result with simpler derivation compared to the one based on the ITT. So why ITT? Because this trick does not work in most cases, and ITT provides a general framework to calculate the nonlinear response variable.

The corresponding effective friction of the probe is

$$\boxed{\gamma_{eff} := \lim_{t\to\infty}\frac{F_{ex}}{\left\langle v^z_s(t)\right\rangle} = iF_{ex}\lim_{t\to\infty}\lim_{q\to 0}\frac{q}{\dot{\phi}^s_{\boldsymbol{q}}(t)}} \tag{5.24}$$

5.2 Mori-Zwanzig equation

5.2.1 General formalism and proof

Now we should derive a dynamical equation for $\phi_{\boldsymbol{q}}(t)$. In general, let us consider the time derivative of a phase space's variable $\Big|A(t)\Big\rangle$, which can be rewritten as follows

$$\begin{aligned}\Big|\dot{A}(t)\Big\rangle &= \mathcal{L}\Big|A(t)\Big\rangle = e^{\mathcal{L}t}\mathcal{L}\Big|A\Big\rangle \\ &= e^{\mathcal{L}t}(\mathcal{P}+\mathcal{Q})\mathcal{L}\Big|A\Big\rangle \\ &= e^{\mathcal{L}t}\Big\langle A\Big|A\Big\rangle^{-1}\Big|A\Big\rangle\Big\langle A\Big|\mathcal{L}\Big|A\Big\rangle + e^{\mathcal{L}t}\mathcal{Q}\mathcal{L}\Big|A\Big\rangle \\ &= \underbrace{\Big\langle A\Big|A\Big\rangle^{-1}\Big\langle A\Big|\mathcal{L}\Big|A\Big\rangle}_{-\lambda}\Big|A(t)\Big\rangle + e^{\mathcal{L}t}\mathcal{Q}\mathcal{L}\Big|A\Big\rangle,\end{aligned} \tag{5.25}$$

where the projectors are defined as

$$\begin{aligned}\mathcal{P} &= \Big\langle A\Big|A\Big\rangle^{-1}\Big|A\Big\rangle\Big\langle A\Big| \\ \mathcal{Q} &= \mathbf{1}-\mathcal{P}\end{aligned} \tag{5.26}$$

The projector $\mathcal{P}$ just picks out the component of a variable including $\Big|A\Big\rangle$. The formal solution of (5.25) is

$$\Big|A(t)\Big\rangle = e^{-\lambda t}\Big|A(0)\Big\rangle + e^{-\lambda t}\int_0^t e^{(\mathcal{L}+\lambda)t'}\mathcal{Q}\mathcal{L}\Big|A\Big\rangle dt' \tag{5.27}$$

However, usually it is difficult to solve the integration. The key point of the MZ equation is the reformulation of the integration above. Here I follow the derivation given in [64]. Note that

$$\Big\langle A\Big|e^{\mathcal{Q}\mathcal{L}t}\mathcal{Q}\mathcal{L}\Big|A\Big\rangle = 0 \tag{5.28}$$

Let

$$e^{\mathcal{L}t} - e^{\mathcal{Q}\mathcal{L}t} = e^{\mathcal{L}t}S(t) \tag{5.29}$$

Thus

$$\begin{aligned} S(t) &= 1 - e^{-\mathcal{L}t}e^{\mathcal{Q}\mathcal{L}t} \\ \dot{S}(t) &= e^{-\mathcal{L}t}\mathcal{L}e^{\mathcal{Q}\mathcal{L}t} - e^{-\mathcal{L}t}\mathcal{Q}\mathcal{L}e^{\mathcal{Q}\mathcal{L}t} \\ &= e^{-\mathcal{L}t}\mathcal{P}\mathcal{L}e^{\mathcal{Q}\mathcal{L}t}\end{aligned} \tag{5.30}$$

Formally,

$$S(t) = \int_0^t e^{-\mathcal{L}t'}\mathcal{P}\mathcal{L}e^{\mathcal{Q}\mathcal{L}t'}dt' \tag{5.31}$$

where we have applied that $S(0) = 0$ according to eq. (5.29). Thus

$$e^{\mathcal{L}t}\mathcal{Q}\mathcal{L}\Big|A\Big\rangle = e^{\mathcal{Q}\mathcal{L}t}\mathcal{Q}\mathcal{L}\Big|A\Big\rangle + \int_0^t e^{\mathcal{L}(t-t')}\mathcal{P}\mathcal{L}e^{\mathcal{Q}\mathcal{L}t'}\mathcal{Q}\mathcal{L}\Big|A\Big\rangle dt' \tag{5.32}$$

The above formula can be rewritten as

$$e^{\mathcal{L}t}\mathcal{Q}\mathcal{L}\Big|A\Big\rangle = \Big|f(t)\Big\rangle + \int_0^t e^{\mathcal{L}(t-t')}\mathcal{P}\mathcal{L}\Big|f(t')\Big\rangle dt' \tag{5.33}$$

where the fluctuating force is defined as

$$\Big|f(t)\Big\rangle := e^{\mathcal{Q}\mathcal{L}t}\mathcal{Q}\mathcal{L}\Big|A\Big\rangle. \tag{5.34}$$

Note that

$$\Big\langle A\Big|\mathcal{L}\Big|f(t)\Big\rangle = \Big\langle A\Big|\mathcal{L}\mathcal{Q}\Big|f(t)\Big\rangle = \Big\langle (\mathcal{L}\mathcal{Q})^\dagger A\Big|f(t)\Big\rangle = \Big\langle \mathcal{Q}\mathcal{L}^\dagger A\Big|f(t)\Big\rangle = \Big\langle f^\dagger(0)\Big|f(t)\Big\rangle \tag{5.35}$$

and

$$\begin{aligned} e^{\mathcal{L}(t-t')}\mathcal{P}\mathcal{L}\Big|f(t')\Big\rangle &= e^{\mathcal{L}(t-t')}\Big\langle A\Big|A\Big\rangle^{-1}\Big|A\Big\rangle\Big\langle A\Big|\mathcal{L}\Big|f(t')\Big\rangle \\ &= \Big\langle A\Big|A\Big\rangle^{-1}\Big\langle f^\dagger(0)\Big|f(t')\Big\rangle\Big|A(t-t')\Big\rangle \end{aligned} \tag{5.36}$$

Denote

$$\begin{aligned} m(t) &= \Big\langle A\Big|A\Big\rangle^{-1}\Big\langle f^\dagger(0)\Big|f(t)\Big\rangle \\ \Big\langle f^\dagger(0)\Big| &= \Big\langle \mathcal{Q}\mathcal{L}^\dagger A\Big| \end{aligned} \tag{5.37}$$

Thus we get the Mori-Zwanzig (MZ) equation

$$\boxed{\Big|\dot{A}(t)\Big\rangle = -\lambda\Big|A(t)\Big\rangle + \int_0^t m(t')\Big|A(t-t')\Big\rangle dt' + \Big|f(t)\Big\rangle} \tag{5.38}$$

Denoting the autocorrelator of the variable A as $C(t) := \Big\langle A\Big|A(t)\Big\rangle$, the MZ equation for the corresponding autocorrelator is

$$\boxed{\dot{C}(t) + \lambda C(t) - \int_0^t m(t')C(t-t')dt' = 0,} \tag{5.39}$$

where

$$\boxed{\begin{aligned} \lambda &= -\Big\langle A\Big|A\Big\rangle^{-1}\Big\langle A\Big|\mathcal{L}\Big|A\Big\rangle \\ m(t) &= \Big\langle A\Big|A\Big\rangle^{-1}\underbrace{\Big\langle \mathcal{Q}\mathcal{L}^\dagger A\Big|}_{\Big\langle f^\dagger(0)\Big|}e^{\mathcal{Q}\mathcal{L}t}\underbrace{\mathcal{Q}\mathcal{L}\Big|A\Big\rangle}_{\Big|f(0)\Big\rangle} \end{aligned}} \tag{5.40}$$

Matrix Form of the MZ equation

The projector can be generalized to project to a subspace and the corresponding MZ equation should have matrix form. Explicitly, the projection to a n dimen-

sional subspace $\{\Big|A_1\Big\rangle, \cdots, \Big|A_n\Big\rangle\}$ is

$$\mathcal{P}_n = \sum_{i,j} (\boldsymbol{C}^{-1})_{i,j} \Big|A_i\Big\rangle\Big\langle A_j\Big| \tag{5.41}$$

where the normalization matrix $\boldsymbol{C}^{-1}$ is the inverse of the matrx $\boldsymbol{C}$ with $\boldsymbol{C}_{i,j} := \big\langle A_i\big|A_j\big\rangle$. It can be readily proved that

$$\mathcal{P}_n^2 = \mathcal{P}_n, \tag{5.42}$$

which justifies the definition of a projector itself. The corresponding matrix form of the MZ equation is

$$\boxed{\dot{\boldsymbol{A}}(t) = -\boldsymbol{\lambda}\boldsymbol{A}(t) + \int_0^t \boldsymbol{m}(t')\boldsymbol{A}(t-t')dt' + \boldsymbol{f}(t)} \tag{5.43}$$

where

$$\boldsymbol{A}(t) = \Big(\Big|A_1(t)\Big\rangle, \cdots, \Big|A_n(t)\Big\rangle\Big)^T, \tag{5.44}$$

$$\boldsymbol{f}(t) = \Big(\Big|\boldsymbol{f}_1(t)\Big\rangle, \cdots, \Big|f_n(t)\Big\rangle\Big)^T \tag{5.45}$$

$$\boxed{-\boldsymbol{\lambda} = (\boldsymbol{C}^{-1}\boldsymbol{L})^T, \quad \boldsymbol{L}_{i,j} = \Big\langle A_i\Big|\mathcal{L}\Big|A_j\Big\rangle,} \tag{5.46}$$

and

$$\boxed{\boldsymbol{m} = (\boldsymbol{C}^{-1}\bar{\boldsymbol{m}})^T \quad , \bar{\boldsymbol{m}}_{i,j} = \Big\langle \mathcal{Q}_n\mathcal{L}^\dagger A_i\Big|e^{\mathcal{Q}_n\mathcal{L}t}\Big|\mathcal{Q}_n\mathcal{L}A_j\Big\rangle} \tag{5.47}$$

The corresponding MZ equation for autocorrelation function is

$$\boxed{\dot{\boldsymbol{C}}^T(t) + \boldsymbol{\lambda}\boldsymbol{C}^T(t) - \int_0^t \boldsymbol{m}(t')\boldsymbol{C}^T(t-t')dt' = 0} \tag{5.48}$$

MZ equation in the frequency domain

Now we want to get the MZ equation in frequency domain by a modified Laplace transform (LT) defined as

$$\widehat{\phi}(z) = i\int_0^\infty e^{izt}\phi(t)dt, \quad Im(z) > 0 \tag{5.49}$$

The conversion to the conventional LT $\bar{\phi}(s) = \int_0^\infty e^{-st}\phi(t)dt\,(Re(s) < 0)$ is

$$\widehat{\phi}(z) = i\int_0^\infty e^{-(-iz)t}\phi(t)dt = i\bar{\phi}(-iz) \tag{5.50}$$

Two important properties of the modified LT are

$$\begin{aligned}\widehat{\dot{\phi}}(z) &= i\bar{\dot{\phi}}(-iz) = i[(-iz)\bar{\phi}(-iz) - \phi(0)] \\ &= -iz\widehat{\phi}(z) - i\phi(0)\end{aligned} \tag{5.51}$$

and

$$\begin{aligned}&LT[\int_0^t f(t-t')g(t')dt'](z) \\ &= iLT[\int_0^t f(t-t')g(t')dt'](-iz) \\ &= i\bar{f}(-iz)\bar{g}(-iz) = -i\widehat{f}(z)\widehat{g}(z)\end{aligned} \tag{5.52}$$

which can be easily obtained from the ones of the conventional LT [65].

Doing LT of the MZ equation (5.39) with the LT properties (5.51, 5.52), one gets

$$\widehat{\dot{C}}(z) = -iz\widehat{C}(z) - iC(0) \tag{5.53}$$

$$LT[\int_0^t m(t')C(t-t')dt'] = -i\widehat{m}(z)\widehat{C}(z) \tag{5.54}$$

Thus

$$-iz\widehat{C}(z) - iC(0) + \lambda\widehat{C}(z) + i\widehat{m}(z)\widehat{C}(z) = 0 \tag{5.55}$$

The LT transform of the autocorrelation function of $\left|\mathrm{A(t)}\right\rangle$ is

$$\boxed{\widehat{C}(z) = \frac{iC(0)}{-iz + \lambda + i\widehat{m}(z)}} \tag{5.56}$$

$$\begin{aligned}\widehat{m}(z) &= i\int_0^\infty e^{izt}\langle A|A\rangle^{-1}\left\langle \mathcal{QL}^\dagger A\middle| e^{\mathcal{QL}t}\mathcal{QL}\middle| A\right\rangle dt \\ &= i\langle A|A\rangle^{-1}\left\langle \mathcal{QL}^\dagger A\middle|\int_0^\infty e^{izt}e^{\mathcal{QL}t}dt\middle|\mathcal{QL}A\right\rangle\end{aligned} \tag{5.57}$$

Note that

$$\begin{aligned}\int_0^\infty e^{izt}e^{\mathcal{Q}\mathcal{L}t}dt &= (iz+\mathcal{Q}\mathcal{L})^{-1}e^{(iz+\mathcal{Q}\mathcal{L})t}\Big|_0^\infty \\ &= -(iz+\mathcal{Q}\mathcal{L})^{-1}\end{aligned} \tag{5.58}$$

where we have used the property $e^{(iz+\mathcal{Q}\mathcal{L})\infty} \to 0$ due to $Im(z) > 0$. Thus

$$\widehat{m}(z) = -i\big\langle A\big|A\big\rangle^{-1}\Big\langle \mathcal{Q}\mathcal{L}^\dagger A\Big|(iz+\mathcal{Q}\mathcal{L})^{-1}\Big|\mathcal{Q}\mathcal{L}A\Big\rangle \tag{5.59}$$

5.2.2 Mori-Zwanzig equation of the probe

In this section, first we will derive the dynamics of the DACP $\phi^s_{\boldsymbol{q}}(t)$ based on the above MZ formalism.

Subspace and projectors

Let us pick a subspace whose bases are

$$S_2 = \Big\{\Big|A_1\Big\rangle = \Big|\rho^s_{\boldsymbol{q}}\Big\rangle, \Big|A_2\Big\rangle = \Big|j^s_{\boldsymbol{q}_L}\Big\rangle\Big\}, \tag{5.60}$$

where $\rho^s_{\boldsymbol{q}}$ and $j^s_{\boldsymbol{q}_L}$ are density and current of the probe defined in Eq. (5.13) and Eq.(5.14), respectively. Note that being different from refs.[27, 47], here we not only choose the density but also current as the basis, the reason is that granular particles are typically not over-damped, the density current may also be important to the dynamics of the self density correlator.

The projector $\mathcal{P}$ into the subspace of the probe's density and current is

$$\mathcal{P} = \sum_{i,j}\Big|A_i\Big\rangle\Big\langle A_j\Big|\Big(\boldsymbol{C}^{-1}\Big)_{i,j} \tag{5.61}$$

where $\boldsymbol{C}^{-1}$ is the inverse matrix of the correlation matrix $\boldsymbol{C}$ defined as $\boldsymbol{C}_{i,j} = \Big\langle A_i\Big|A_j\Big\rangle$. The dynamics of the density autocorrelator of the probe is included in the MZ equation

$$\dot{\boldsymbol{C}}^{\boldsymbol{T}}(\boldsymbol{t}) = -\boldsymbol{\lambda}\boldsymbol{C}^T(t) + \int_0^t \boldsymbol{m}(t')\boldsymbol{C}^T(t-t')dt' \tag{5.62}$$

with

$$\boxed{\begin{aligned} -\boldsymbol{\lambda} &= (\boldsymbol{C}^{-1}\boldsymbol{L})^T, \quad \boldsymbol{L}_{i,j} = \left\langle A_i \middle| \mathcal{L} \middle| A_j \right\rangle, \\ \boldsymbol{m} &= (\boldsymbol{C}^{-1}\bar{\boldsymbol{m}})^T, \quad \bar{\boldsymbol{m}}_{i,j} = \left\langle \mathcal{Q}\mathcal{L}^\dagger A_i \middle| e^{\mathcal{Q}\mathcal{L}_{FP}t} \middle| \mathcal{Q}\mathcal{L}A_j \right\rangle \end{aligned}}, \tag{5.63}$$

where $\boldsymbol{L}$ is the frequency matrix, ,$\bar{\boldsymbol{m}}$ is the memory matrix, and $-\boldsymbol{\lambda}$ and $\boldsymbol{m}$ are the normalization form of the corresponding matrices.

correlation matrix and frequency matrix

Note that $\rho^s_{\boldsymbol{q}} = e^{i\boldsymbol{q}\cdot\boldsymbol{r}^s}$, and $j^s_{\boldsymbol{q}_L} = v^s_{\boldsymbol{q}_L}\rho^s_{\boldsymbol{q}}$, and $\left\langle \rho^s_{\boldsymbol{q}} \middle| j^s_{\boldsymbol{q}_L} \right\rangle = \left\langle v^s_{\boldsymbol{q}_L} \right\rangle = 0$ due to symmetry in the initial equilibrium state. The correlation matrix $\boldsymbol{c}$ and its inverse matrix can be easily obtained,

$$\boldsymbol{C} = \begin{pmatrix} 1 & 0 \\ 0 & \frac{k_BT}{m_s} \end{pmatrix}, \quad \boldsymbol{C^{-1}} = \begin{pmatrix} 1 & 0 \\ 0 & \frac{m_s}{k_BT} \end{pmatrix}. \tag{5.64}$$

Note that $\mathcal{L}_{FP}\rho^s_{\boldsymbol{q}} = \boldsymbol{v}_s \cdot i\boldsymbol{q}\rho^s_{\boldsymbol{q}} = iqj^s_{\boldsymbol{q}_L}$ and $\mathcal{L}_{FP}j^s_{\boldsymbol{q}_L} = (iqv^{s\,2}_{\boldsymbol{q}_L} + \frac{F^{int}_{s\,L} - \gamma v^s_{\boldsymbol{q}_L} + F_{ex}}{m})\rho^s_{\boldsymbol{q}}$, and $\left\langle \boldsymbol{v}^s_{\boldsymbol{q}_L} \right\rangle = \left\langle \boldsymbol{v}^{s\,3}_{\boldsymbol{q}_L} \right\rangle = 0$, and $\left\langle \boldsymbol{v}^{s\,2}_{\boldsymbol{q}_L} \right\rangle = \frac{k_BT}{m}$ due to the Maxwellian distribution of the velocity in equilibrium state. The frequency matrix $\boldsymbol{L}$ is

$$\boldsymbol{L} = \begin{pmatrix} 0 & iq\frac{k_BT}{m_s} + \frac{F_{ex,\boldsymbol{q}_L}}{m_s} \\ iq\frac{k_BT}{m_s} & \frac{-\gamma_0 k_BT}{m_s^2} \end{pmatrix} \tag{5.65}$$

and the normalized form of the frequency matrix is

$$-\boldsymbol{\lambda} = (\boldsymbol{C}^{-1}\boldsymbol{L})^T = \begin{pmatrix} 0 & iq \\ \frac{F^{ex}_{\boldsymbol{q}_L}}{m_s} + \frac{iqk_BT}{m_s} & -\frac{\gamma_0}{m_s} \end{pmatrix}. \tag{5.66}$$

memory matrix

Now let us deal with the memory matrix. Note that $\mathcal{Q}\mathcal{L}_{FP}|\rho^s_{\boldsymbol{q}}\rangle = iq\mathcal{Q}|j^s_{\boldsymbol{q}_L}\rangle = 0$ and $\mathcal{Q}\mathcal{L}_{FP}|j^s_{\boldsymbol{q}_L}\rangle = iq\mathcal{Q}|v^{s\,2}_{\boldsymbol{q}_L}\rho^s_{\boldsymbol{q}}\rangle + \frac{1}{m}\mathcal{Q}|F^{int}_{s\,L}\rho^s_{\boldsymbol{q}}\rangle$. The conjugate term is

$$\begin{aligned} &\mathcal{L}^\dagger_{FP}\rho^s_{\boldsymbol{q}} = -(\boldsymbol{v}_s \cdot i\boldsymbol{q})\rho^s_{\boldsymbol{q}} + \frac{\boldsymbol{F}_{ex}}{k_BT} \cdot \boldsymbol{v}_s\rho^s_{\boldsymbol{q}} = -iqj^s_{\boldsymbol{q}_L} + \frac{F_{ex}}{k_BT}j^s_{\boldsymbol{q}_L} \\ &\implies \left\langle \mathcal{Q}\mathcal{L}^\dagger_{FP}\rho^s_{\boldsymbol{q}} \right| = 0 \end{aligned} \tag{5.67}$$

where we have assumed that the wave vector q is parallel to the pulling force, $\boldsymbol{q} \parallel \boldsymbol{F}_{ex}$, and applied the expression of the conjugate operator $\mathcal{L}_{FP}^{\dagger}$. Thus the memory term and its normalized form are simplified to

$$\bar{\boldsymbol{m}}(t) = \begin{pmatrix} 0 & 0 \\ 0 & m_q^s(t) \end{pmatrix}, \quad \boldsymbol{m}(t) = (\boldsymbol{C}^{-1}\bar{\boldsymbol{m}})^T = \begin{pmatrix} 0 & 0 \\ 0 & M_q^s \end{pmatrix} \tag{5.68}$$

where $M_q^s = \frac{m_s}{k_B T} m_q^s(t)$ and

$$\boxed{m_q^s(t) = \left\langle \mathcal{Q}\mathcal{L}_{FP}^{\dagger} j_{\boldsymbol{q}_L}^s \middle| e^{\mathcal{Q}\mathcal{L}_{FP}t} \middle| \mathcal{Q}\mathcal{L}_{FP} j_{\boldsymbol{q}_L}^s \right\rangle.} \tag{5.69}$$

MZ equation in the the frequency domain

By applying Laplace transform $\widehat{\phi}(z) = i\int_0^{\infty} e^{izt}\phi(t)dt, Im(z) > 0$, we can obtain the MZ equation in the frequency domain as

$$\boldsymbol{C}^T(z) = \Big\{ -z\boldsymbol{I} - i\boldsymbol{\lambda} + \boldsymbol{m}(z) \Big\}^{-1} \boldsymbol{C}^T(0) \tag{5.70}$$

Inserting the related matrices as obtained in the last subsection, we get

$$\hat{\boldsymbol{C}}^T(z) = \frac{-1}{z(z - M_q^s(z) + \frac{i\gamma}{m_s}) - (\frac{q^2 k_B T - i\boldsymbol{F}_{ex}\cdot\boldsymbol{q}}{m_s})} \begin{pmatrix} z - M_q^s(z) + \frac{i\gamma}{m_s} & -q\frac{k_B T}{m_s} \\ -\frac{qk_B T - i\boldsymbol{F}_{ex}\cdot\hat{\boldsymbol{q}}}{m_s} & z\frac{k_B T}{m_s} \end{pmatrix} \tag{5.71}$$

which is the MZ equation in the frequency domain. The density correlator of the pulled particle equals $\hat{\phi}_{\boldsymbol{q}}^s(z) = [\hat{\boldsymbol{C}}^T(z)]_{1,1}$, whose explicit form reads

$$\boxed{\hat{\phi}_{\boldsymbol{q}}^s(z) = \frac{-1}{z - \frac{(q^2 k_B T - i\boldsymbol{F}_{ex}\cdot\boldsymbol{q})/m_s}{z - M_q^s(z) + i\gamma/m_s}}} \tag{5.72}$$

MZ equation in the time domain

Rewriting the (5.72) as

$$\Big\{ -M_q^s(z) + \frac{i\gamma}{m_s} + z \Big\}\Big\{ z\hat{\phi}_{\boldsymbol{q}}^s(z) + 1 \Big\} - \Big\{ \frac{q^2 k_B T - i\boldsymbol{F}_{ex}\cdot\boldsymbol{q}}{m_s} \Big\}\hat{\phi}_{\boldsymbol{q}}^s(z) = 0 \tag{5.73}$$

Applying the LT properties, we have

$$\begin{aligned} \hat{\dot{\phi}}_{\boldsymbol{q}}^s(z) &= -i\big\{ z\hat{\phi}_{\boldsymbol{q}}^s(z) + \phi_{\boldsymbol{q}}^s(0) \big\} = -i\big\{ z\hat{\phi}_{\boldsymbol{q}}^s(z) + 1 \big\} \\ \hat{\ddot{\phi}}_{\boldsymbol{q}}^s(z) &= -i\big\{ z\hat{\dot{\phi}}_{\boldsymbol{q}}^s(z) + \dot{\phi}_{\boldsymbol{q}}^s(0) \big\} = -z\big\{ z\hat{\phi}_{\boldsymbol{q}}^s(z) + 1 \big\} \end{aligned} \tag{5.74}$$

Inserting (5.74) and the initial conditions $\phi^s_{\boldsymbol{q}}(0) = 1$ and $\dot{\phi}^s_{\boldsymbol{q}}(0) = 0$ into eq.(5.73), we obtain

$$-iM^s_q(z)\hat{\phi}^s_{\boldsymbol{q}}(z) - \frac{\gamma}{m_s}\hat{\phi}^s_{\boldsymbol{q}}(z) - \hat{\dot{\phi}}^s_{\boldsymbol{q}}(z) - \left\{\frac{q^2 k_B T - i\boldsymbol{F}_{ex}\cdot\boldsymbol{q}}{m_s}\right\}\hat{\phi}^s_{\boldsymbol{q}}(z) = 0 \quad (5.75)$$

Laplace transforming the above equation, we obtain the density auto correlator of the the pulled particle in time domain [1]

$$\boxed{\ddot{\phi}^s_{\boldsymbol{q}}(t) + \frac{\gamma}{m}\dot{\phi}^s_{\boldsymbol{q}}(t) + (\Omega^{s\,2}_q - \frac{i\boldsymbol{F}_{ex}\cdot\boldsymbol{q}}{m_s})\phi^s_{\boldsymbol{q}}(t) + \int_0^t d\tau\, M^s_q(t-\tau)\dot{\phi}^s_{\boldsymbol{q}}(\tau) = 0} \quad (5.76)$$

with

$$\boxed{\begin{aligned}\Omega^{s\,2}_q &= q^2\frac{k_B T}{m_s}\\ M^s_q(t) &= -\frac{m_s}{k_B T}\left\langle \mathcal{Q}\mathcal{L}^\dagger_{FP} j^s_{\boldsymbol{q}_L}\middle| e^{\mathcal{Q}\mathcal{L}_{FP}t}\middle|\mathcal{Q}\mathcal{L}_{FP} j^s_{\boldsymbol{q}_L}\right\rangle\end{aligned}} \quad (5.77)$$

Note that the above MZ equation is exact! But it is usually difficult to solve it due to the memory term $M^s_q(t)$. For the over-damped case, $\frac{\gamma}{m_s} \gg \Omega^s_q$, the second time derivative can be ignored and the MZ equation is reduced to

$$\frac{\gamma}{m}\dot{\phi}^s_{\boldsymbol{q}}(t) + (\Omega^{s\,2}_q - \frac{i\boldsymbol{F}_{ex}\cdot\boldsymbol{q}}{m_s})\phi^s_{\boldsymbol{q}}(t) + \int_0^t d\tau\, M^s_q(t-\tau)\dot{\phi}^s_{\boldsymbol{q}}(\tau) = 0 \quad (5.78)$$

which is identical to the eq. (54) in ref. [47] with the same frequency term $(\Omega^{s\,2}_q - \frac{i\boldsymbol{F}_{ex}\cdot\boldsymbol{q}}{m_s})$, see eq. (60) in ref.[47].

Connection to the effective friction

Here we want to obtain the effective friction γ_{eff} by combining the expression of (5.24) and the above MZ equation. Eq.(5.23) tells us that the average velocity of

[1] At first glance, the memory term looks inconsistent with the same derivation for a Hamiltonian system (the sign of the memory term is "+" in a Hamiltonian system). However, the results are consisted. Note that $\mathcal{L}_{FP} \longrightarrow i\mathcal{L}$ and $M^s_{q,FP}(t) = -\frac{m_s}{k_B T}\left\langle j^s_{\boldsymbol{q}_L}|\mathcal{L}_{FP}\mathcal{Q}e^{\mathcal{Q}\mathcal{L}_{FP}t}\mathcal{Q}\mathcal{L}_{FP}|j^s_{\boldsymbol{q}_L}\right\rangle$
$\longrightarrow -\frac{m_s}{k_B T}\left\langle j^s_{\boldsymbol{q}_L}|i\mathcal{L}\mathcal{Q}e^{\mathcal{Q}i\mathcal{L}t}\mathcal{Q}i\mathcal{L}|j^s_{\boldsymbol{q}_L}\right\rangle = \frac{m_s}{k_B T}\left\langle j^s_{\boldsymbol{q}_L}|\mathcal{L}\mathcal{Q}e^{\mathcal{Q}i\mathcal{L}t}\mathcal{Q}\mathcal{L}|j^s_{\boldsymbol{q}_L}\right\rangle$

the probe along a wave vector $\boldsymbol{q}$ is $\left\langle \boldsymbol{v}_s(t)\cdot\hat{\boldsymbol{q}}\right\rangle = \lim_{q\to 0}\frac{\dot{\phi}^s_{\boldsymbol{q}}(t)}{iq}$. Note that

$$\begin{aligned}\dot{\phi}^s_{\boldsymbol{q}}(t\to\infty) &= \int_0^\infty \ddot{\phi}^s_{\boldsymbol{q}}(t')dt' + \dot{\phi}^s_{\boldsymbol{q}}(0) = -i\hat{\dot{\phi}}^s_{\boldsymbol{q}}(z)\Big|_{z\to 0} \\ &= iz\big\{z\hat{\phi}^s_{\boldsymbol{q}}(z)+1\big\}\Big|_{z\to 0} = iz^2\hat{\phi}^s_{\boldsymbol{q}}(z)\Big|_{z\to 0}\end{aligned} \tag{5.79}$$

where we have applied the definition of the LT and its property (5.74). We have chosen the wave vector $\boldsymbol{q}$ along the direction of the pulling force $\boldsymbol{q}\parallel\boldsymbol{F}_{ex}$. Inserting the above expression (5.79) and the MZ equation (5.72) into the expression of the effective friction (5.24), we get

$$\begin{aligned}\gamma_{eff} &= iF_{ex}\lim_{t\to\infty}\lim_{q\to 0}\frac{q}{\dot{\phi}^s_{\boldsymbol{q}}(t)} = F_{ex}\lim_{z\to 0}\lim_{q\to 0}\frac{q}{z\big\{z\hat{\phi}^s_{\boldsymbol{q}}(z)+1\big\}} \\ &= F_{ex}\lim_{z\to 0}\lim_{q\to 0}\Big[\frac{q}{z}+\frac{-i\gamma+(M^s_q(z)-z)m_s}{qk_BT-iF_{ex}}\Big] \\ &= \gamma + im_sM^s_{q\to 0}(z\to 0)\end{aligned} \tag{5.80}$$

Note that the limit order cannot be changed for the term $\frac{q}{z}$ in the third equation! Thus we obtain

$$\boxed{\gamma_{eff} = \gamma + m_s\int_0^\infty M^s_{q\to 0}(t')dt'} \tag{5.81}$$

Here the expression of the effective friction is exactly connected to the memory term in the MZ equation, while in [47], the force autocorrelator is approximated by projecting onto the pair density pairs, see Eq. (88-89) in [47].

5.3 Microscopic MCT of the probe

In the MZ equation of the probe, the memory term may slowly decay in high density due to crowding. Thus we will apply the standard mode-coupling approximation (MCA) to the memory term

$$M^s_q(t)\approx M^{s,MCT}_q(t) = -\frac{m_s}{k_BT}\Big\langle j^s_{\boldsymbol{q}_L}\Big|\mathcal{L}_{FP}\mathcal{Q}\mathcal{P}^s_2e^{\mathcal{Q}\mathcal{L}_{FP}t}\mathcal{P}^s_2\mathcal{Q}\mathcal{L}_{FP}\Big|j^s_{\boldsymbol{q}_L}\Big\rangle \tag{5.82}$$

where the projector is defined as

$$\boxed{\begin{aligned}&\mathcal{P}_2^s = \sum_{\boldsymbol{k}_1,\boldsymbol{k}_2,\boldsymbol{k}_1',\boldsymbol{k}_2'} \left|A_{\boldsymbol{k}_1,\boldsymbol{k}_2}\right\rangle\left\langle A_{\boldsymbol{k}_1',\boldsymbol{k}_2'}\right| \boldsymbol{C}^{-1}_{\boldsymbol{k}_1,\boldsymbol{k}_2,\boldsymbol{k}_1',\boldsymbol{k}_2'}\\ &\left|A_{\boldsymbol{k}_1,\boldsymbol{k}_2}\right\rangle = \left|\rho^s_{\boldsymbol{k}_1}\rho_{\boldsymbol{k}_2}\right\rangle\\ &\boldsymbol{C}_{\boldsymbol{k}_1,\boldsymbol{k}_2,\boldsymbol{k}_1',\boldsymbol{k}_2'} = \left\langle \rho^s_{\boldsymbol{k}_1}\rho_{\boldsymbol{k}_2}\middle|\rho^s_{\boldsymbol{k}_1'}\rho_{\boldsymbol{k}_2'}\right\rangle\end{aligned}} \tag{5.83}$$

5.3.1 Translational invariance

Note that translating all the positions with an arbitrary vector $\boldsymbol{R}$, $\Gamma = (\boldsymbol{r}_1, \cdots, \boldsymbol{r}_N) \to \Gamma' = (\boldsymbol{r}_1 + \boldsymbol{R}, \cdots, \boldsymbol{r}_N + \boldsymbol{R})$, both the Hamiltonian $H(\Gamma)$ and Fokker-Planck operator $\mathcal{L}_{FP}(\Gamma)$ are invariant, i.e.

$$H(\Gamma) = H(\Gamma'), \quad \mathcal{L}_{FP}(\Gamma) = \mathcal{L}_{FP}(\Gamma'), \tag{5.84}$$

which can be easily confirmed by their definitions. Applying the properties of the translational invariance, we have

$$\begin{aligned}\left\langle \rho^s_{\boldsymbol{q}}\middle|\rho^s_{\boldsymbol{p}}(t)\right\rangle &= \int \frac{e^{\frac{-H(\Gamma)}{k_BT}}}{Z} e^{-i\boldsymbol{q}\cdot\boldsymbol{r}_s} e^{\mathcal{L}_{FP}(\Gamma)t} e^{i\boldsymbol{p}\cdot\boldsymbol{r}_s} d\Gamma\\ &= \int \frac{e^{\frac{-H(\Gamma')}{k_BT}}}{Z} e^{-i\boldsymbol{q}\cdot(\boldsymbol{r}_s+\boldsymbol{R})} e^{\mathcal{L}_{FP}(\Gamma')t} e^{i\boldsymbol{p}\cdot(\boldsymbol{r}_s+\boldsymbol{R})} d\Gamma'\\ &= e^{i(\boldsymbol{p}-\boldsymbol{q})\cdot\boldsymbol{R}}\left\langle \rho^s_{\boldsymbol{q}}\middle|\rho^s_{\boldsymbol{p}}(t)\right\rangle = \left\langle \rho^s_{\boldsymbol{q}}\middle|\rho^s_{\boldsymbol{p}}(t)\right\rangle\delta_{\boldsymbol{q},\boldsymbol{p}}\end{aligned} \tag{5.85}$$

In the second equation of the above formalism, just a change of the integration variable $\Gamma \to \Gamma'$ is used, in the third equation, the translational invariance properties (5.84) are applied, and in the last equation, we have input a physics requirement that observables should be independent of the choice of coordinate and have noted that the vector $\boldsymbol{R}$ can have an arbitrary value. Similarly, we have

$$\left\langle \rho^s_{\boldsymbol{q}}\middle|\rho_{\boldsymbol{p}}(t)\right\rangle = \left\langle \rho^s_{\boldsymbol{q}}\middle|\rho_{\boldsymbol{p}}(t)\right\rangle\delta_{\boldsymbol{q},\boldsymbol{p}}, \quad \left\langle \rho_{\boldsymbol{q}}\middle|\rho_{\boldsymbol{p}}(t)\right\rangle = \left\langle \rho_{\boldsymbol{q}}\middle|\rho_{\boldsymbol{p}}(t)\right\rangle\delta_{\boldsymbol{q},\boldsymbol{p}} \tag{5.86}$$

5.3.2 Vertex terms and closure equation

The normalization matrix can be calculated by applying the translational invariance

$$\begin{aligned} \boldsymbol{C}_{\boldsymbol{k}_1,\boldsymbol{k}_2,\boldsymbol{k}_1',\boldsymbol{k}_2'} &= \left\langle \rho^s_{\boldsymbol{k}_1}\rho_{\boldsymbol{k}_2}\middle|\rho^s_{\boldsymbol{k}_1'}\rho_{\boldsymbol{k}_2'}\right\rangle \\ &= \left\langle \rho^s_{\boldsymbol{k}_1}\middle|\rho^s_{\boldsymbol{k}_1'}\right\rangle\left\langle \rho_{\boldsymbol{k}_2}\middle|\rho_{\boldsymbol{k}_2'}\right\rangle = \delta_{\boldsymbol{k}_1,\boldsymbol{k}_1'}NS_{k_2}\delta_{\boldsymbol{k}_2,\boldsymbol{k}_2'} \end{aligned} \tag{5.87}$$

where $S_{k_2} = \left\langle \rho_{\boldsymbol{k}_2}\middle|\rho_{\boldsymbol{k}_2}\right\rangle/N$ is the static structure of the bulk system. The corresponding inverse matrix is

$$\boldsymbol{C}^{-1}_{\boldsymbol{k}_1,\boldsymbol{k}_2,\boldsymbol{k}_1',\boldsymbol{k}_2'} = \frac{1}{NS_{k_2}}\delta_{\boldsymbol{k}_1,\boldsymbol{k}_1'}\delta_{\boldsymbol{k}_2,\boldsymbol{k}_2'} \tag{5.88}$$

The explicit form of eq.(5.82) is

$$\begin{aligned} M^{s,MCT}_q(t) = -\frac{m_s}{k_BT}\sum_{\substack{\boldsymbol{k}_1,\boldsymbol{k}_2,\boldsymbol{k}_1',\boldsymbol{k}_2'\\ \boldsymbol{p}_1,\boldsymbol{p}_2,\boldsymbol{p}_1',\boldsymbol{p}_2'}} \boldsymbol{C}^{-1}_{\boldsymbol{k}_1,\boldsymbol{k}_2,\boldsymbol{k}_1',\boldsymbol{k}_2'}\boldsymbol{C}^{-1}_{\boldsymbol{p}_1,\boldsymbol{p}_2,\boldsymbol{p}_1',\boldsymbol{p}_2'} \\ \underbrace{\left\langle j^s_{\boldsymbol{q}_L}\middle|\mathcal{L}_{FP}Q\middle|\rho^s_{\boldsymbol{k}_1}\rho_{\boldsymbol{k}_2}\right\rangle}_{(L)}\underbrace{\left\langle \rho^s_{\boldsymbol{k}_1'}\rho_{\boldsymbol{k}_2'}\middle|e^{\mathcal{Q}\mathcal{L}_{FP}t}\middle|\rho^s_{\boldsymbol{p}_1}\rho_{\boldsymbol{p}_2}\right\rangle}_{(M)}\underbrace{\left\langle \rho^s_{\boldsymbol{p}_1'}\rho_{\boldsymbol{p}_2'}\middle|Q\mathcal{L}_{FP}\middle|j^s_{\boldsymbol{q}_L}\right\rangle}_{(R)} \end{aligned} \tag{5.89}$$

The right term (R) is

$$\begin{aligned} (R) = \left\langle \rho^s_{\boldsymbol{p}_1'}\rho_{\boldsymbol{p}_2'}\middle|Q\mathcal{L}_{FP}\middle|j^s_{\boldsymbol{q}_L}\right\rangle &= \left\langle \rho^s_{\boldsymbol{p}_1'}\rho_{\boldsymbol{p}_2'}\middle|\frac{F^{int}_{s\,L} + iq\big(v^{L\,2}_s m_s - k_BT\big)}{m_s}\rho^s_{\boldsymbol{q}}\right\rangle \\ = \frac{1}{m_s}\left\langle \rho^s_{\boldsymbol{p}_1'-\boldsymbol{q}}\rho_{\boldsymbol{p}_2'}\middle|F^{int}_{s\,L}\right\rangle &= \frac{k_BT}{m_s}i(\boldsymbol{p}_1'-\boldsymbol{q})\cdot\hat{\boldsymbol{q}}S^s_{p_1'-q}\delta_{\boldsymbol{p}_1'+\boldsymbol{p}_2',\boldsymbol{q}} \\ &= \frac{-ik_BT\boldsymbol{p}_2'\cdot\hat{\boldsymbol{q}}}{m_s}S^{s\,*}_{p_2'}\delta_{\boldsymbol{p}_1'+\boldsymbol{p}_2',\boldsymbol{q}} \end{aligned} \tag{5.90}$$

where we have used the result $\left\langle v^{L\,2}_s\right\rangle = \frac{k_BT}{m_s}$, have defined the probe-bath particles static structure

$$S^s_{\boldsymbol{q}} := \left\langle \rho^s_{\boldsymbol{q}}\middle|\rho_{\boldsymbol{q}}\right\rangle \tag{5.91}$$

and calculated the interaction force term

$$\begin{aligned}\left\langle \rho^s_{\boldsymbol{q}}\rho_{\boldsymbol{p}}\middle|\boldsymbol{F}^{int}_s\right\rangle &= \frac{1}{Z}\int d\Gamma e^{-\frac{H(\Gamma)}{k_BT}}\rho^{s*}_{\boldsymbol{q}}\rho^*_{\boldsymbol{p}}(-\partial_{\boldsymbol{r}_s}H) = \frac{-k_BT}{Z}\int d\Gamma e^{-\frac{H(\Gamma)}{k_BT}}\partial_{\boldsymbol{r}_s}(\rho^{s*}_{\boldsymbol{q}}\rho^*_{\boldsymbol{p}})\\ &= k_BTi\boldsymbol{q}\left\langle \rho^s_{\boldsymbol{q}}\middle|\rho_{-\boldsymbol{p}}\right\rangle = k_BTi\boldsymbol{q}S^s_q\delta_{\boldsymbol{q}+\boldsymbol{p},0}.\end{aligned} \tag{5.92}$$

In the calculation, the partial integrals and the identity $e^{-\frac{H(\Gamma)}{k_BT}}(-\partial_{\boldsymbol{r}_s}H) = k_BT\partial_{\boldsymbol{r}_s}e^{-\frac{H(\Gamma)}{k_BT}}$ have been applied in the second equation, and the translational invariance has been applied in the last equation.

The left term (L) can be calculated in a straightforward way as follows

$$\begin{aligned}(L) &= \left\langle Q\mathcal{L}^\dagger_{FP}j^s_{\boldsymbol{q}_L}\middle|\rho^s_{\boldsymbol{k}_1}\rho_{\boldsymbol{k}_2}\right\rangle = \left\langle \rho^s_{\boldsymbol{k}_1}\rho_{\boldsymbol{k}_2}\middle|Q\mathcal{L}^\dagger_{FP}j^s_{\boldsymbol{q}_L}\right\rangle^*\\ &= -\left\langle \rho^s_{\boldsymbol{k}_1}\rho_{\boldsymbol{k}_2}\middle|Q\mathcal{L}_{FP}j^s_{\boldsymbol{q}_L}\right\rangle^* + \left\langle \rho^s_{\boldsymbol{k}_1}\rho_{\boldsymbol{k}_2}\middle|\mathcal{Q}\Big\{\frac{2\gamma}{m}\Big[-\boldsymbol{v}_i+\frac{k_BT}{m}\partial_{\boldsymbol{v}_i}\Big]\cdot\partial_{\boldsymbol{v}_i}+\frac{\boldsymbol{F}_{ex}\cdot\boldsymbol{v}_s}{k_BT}\Big\}j^s_{\boldsymbol{q}_L}\right\rangle^*\\ &= -\left\langle \rho^s_{\boldsymbol{k}_1}\rho_{\boldsymbol{k}_2}\middle|Q\mathcal{L}_{FP}j^s_{\boldsymbol{q}_L}\right\rangle^* + \frac{F^L_{ex}}{k_BT}\left\langle \rho^s_{\boldsymbol{k}_1}\rho_{\boldsymbol{k}_2}\middle|\frac{-k_BT+mv^{L\,2}_s}{m}\rho^s_{\boldsymbol{q}}\right\rangle^*\\ &= \frac{-ik_BT\boldsymbol{k}_2\cdot\hat{\boldsymbol{q}}}{m_s}S^s_{k_2}\delta_{\boldsymbol{k}_1+\boldsymbol{k}_2,\boldsymbol{q}}\end{aligned} \tag{5.93}$$

where we have used the property of the relation that

$$\mathcal{L}^\dagger_{FP} = -\mathcal{L}_{FP}+\frac{2\gamma}{m}\Big[-\boldsymbol{v}_i+\frac{k_BT}{m}\partial_{\boldsymbol{v}_i}\Big]\cdot\partial_{\boldsymbol{v}_i}+\frac{\boldsymbol{F}_{ex}\cdot\boldsymbol{v}_s}{k_BT} \tag{5.94}$$

The middle term (M) can be obtained by the factorization approximation

$$\begin{aligned}(M) = \left\langle \rho^s_{\boldsymbol{k}'_1}\rho_{\boldsymbol{k}'_2}\middle|e^{\mathcal{Q}\mathcal{L}_{FP}t}\middle|\rho^s_{\boldsymbol{p}_1}\rho_{\boldsymbol{p}_2}\right\rangle &\approx \left\langle \rho^s_{\boldsymbol{k}'_1}\middle|e^{\mathcal{Q}\mathcal{L}_{FP}t}\middle|\rho^s_{\boldsymbol{p}_1}\right\rangle\left\langle \rho_{\boldsymbol{k}'_2}\middle|e^{\mathcal{Q}\mathcal{L}_{FP}t}\middle|\rho_{\boldsymbol{p}_2}\right\rangle\\ &\approx \left\langle \rho^s_{\boldsymbol{k}'_1}\middle|e^{\mathcal{L}_{FP}t}\middle|\rho^s_{\boldsymbol{p}_1}\right\rangle\left\langle \rho_{\boldsymbol{k}'_2}\middle|e^{\mathcal{L}_{FP}t}\middle|\rho_{\boldsymbol{p}_2}\right\rangle\\ &= \phi^s_{\boldsymbol{p}_1}(t)\phi_{\boldsymbol{p}_2}(t)NS_{p_2}\delta_{\boldsymbol{p}_1,\boldsymbol{k}'_1}\delta_{\boldsymbol{p}_2,\boldsymbol{k}'_2},\end{aligned} \tag{5.95}$$

Putting the results (5.88), (5.90), (5.93), and (5.95) together into (5.89), we get

$$\boxed{M^{s,MCT}_q(t) = \frac{k_BT}{m_s}\sum_{\boldsymbol{k}+\boldsymbol{p}=\boldsymbol{q}}\frac{(\boldsymbol{p}\cdot\hat{\boldsymbol{q}})^2S^s_pS^{s*}_p}{NS_p}\phi^s_{\boldsymbol{k}}(t)\phi_{\boldsymbol{p}}(t)} \tag{5.96}$$

which is the mode-coupling approximation (MCA) of the memory term. With inputting static structures and the density correlator of the bulk system $\phi_{\boldsymbol{k}}(t)$, which can be obtained by the standard MCT equation, the MZ equation (5.114) under the MCA (5.96) forms a closed equation, i.e. a microscopic MCT formalism for the fixed force pulling microrheology. An important difference to the refs.[27, 47] is that here the memory term has nothing to do with the external pulling force $\boldsymbol{F}_{ex}$. This is due to the fact that here the external force in the adjoint dynamics operator is coupled to the velocity, see term $\frac{\boldsymbol{F}_{ex}\cdot\boldsymbol{v}_s}{k_BT}$ in eq. (5.94), which is cancelled in the right term in the third line of eq. (5.93) due to parity. While the adjoint dynamics operator is coupled to the interacting force, see eq. (77) in [47], which results in a force dependent memory term, eq. (78) in [47].

5.4 Schematic-MCT model

Before solving the microscopic mode-coupling equation, it is interesting to investigate the simplified version of the microscopic equation, the schematic model. The basic assumption is that the essence of the MCT is captured by the coupling of the density correlators with different wave-vectors (the modes), which can be reduced to an equation of single wave-vector dependence. (additional fitting parameters are required.) This simplified model is important mainly for two reasons:

1. It helps to understand the underlying mathematical structure of the full-MCT (Note that the full-MCT is quite complex that there are vertex terms and couplings between different DACs). Many features of the full-MCT can be reproduced based on the schematic model. For instance, the two step decays and the exponent relation between α and β relaxations. A comprehensive and mathematical discussion can be found in W. Götze's book [52].

2. It provides a tool to compare the MCT with various experiments. The assumption is that the schematic model can capture the full-MCT equation with additional control parameters. In practice, applying the schematic-model to fit the glassy dynamics in experiments is not only convenient, because in many experiments, the precise interaction is unknown, which makes the construction of a full-MCT is quite difficult. A few nice examples of applying the schematic model to fit experimental data can be found in [27, 66, 67, 58].

5.4.1 Schematic model of fixed force pulling

Let us construct a simplified model of the MCT based on the expression of the effective friction eq.(5.81) and the mode-coupling approximation eq.(5.96). Note that

- the effective friction in eq.(5.81) is related to the memory kernel in the $q \to 0$ limit;
- the MCT approximation of the kernel eq.(5.96) requires all coupling terms of the DACs with the restriction of the wave vectors $\boldsymbol{k} + \boldsymbol{p} = \boldsymbol{q}$.

These hint us to construct a memory kernel which contains only a pair of wave vectors satisfying $\boldsymbol{k} + \boldsymbol{p} = \boldsymbol{0}$ and the wave vector $\boldsymbol{k}$ is chosen along $\boldsymbol{q}$. The corresponding MCT equation of the probe with a pair of coupling wave vectors only is

$$\begin{aligned}\ddot{\phi}^s_{\boldsymbol{k}}(t) + \frac{\gamma}{m}\dot{\phi}^s_{\boldsymbol{k}}(t) + \Big[\frac{k^2 k_B T}{m_s} - \frac{ikF_{ex}}{m_s}\Big]\phi^s_{\boldsymbol{k}}(t) \\ + \frac{k_B T}{m_s}\int_0^t d\tau\, \frac{k^2 S^s_k S^{s\,*}_k}{N S_k}\phi^{s\,*}_{\boldsymbol{k}}(t-\tau)\phi_{\boldsymbol{k}}(t-\tau)\dot{\phi}^s_{\boldsymbol{k}}(\tau) = 0\end{aligned} \tag{5.97}$$

where we have applied the properties $\phi^s_{-\boldsymbol{k}} = \phi^{s\,*}_{\boldsymbol{k}}$, $\phi_{-\boldsymbol{k}} = \phi_{\boldsymbol{k}}$ and $S_{-k} = S_k$.

To further simplify the above equation, we choose $k = \gamma = m_s = 1$ and replace the coupling parameter between the DAC of the probe and the DAC of the bath particles by a simple coupling parameter: $\frac{k^2 S^s_k S^{s\,*}_k}{N S_k} \to v_A$. The corresponding simplified equation is

$$\boxed{\begin{aligned}\ddot{\phi}_s(t) + \nu_s\dot{\phi}_s(t) + \Omega_s^2\phi_s(t) + \int_0^t d\tau\, M_s(t-\tau)\dot{\phi}_s(t) = 0 \\ M_s(t) = v_A\phi^{s\,*}(t)\phi(t)\end{aligned}}, \tag{5.98}$$

where the damping term and the frequency term are

$$\nu_s = 1, \quad \Omega_s^2 = 1 - iF_{ex}. \tag{5.99}$$

The above is a schematic model of the probe particle. The frequency term Ω_s^2 is identical to the earlier schematic equation for the over-damped colloidal systems [27, 47]; the memory term of the probe M_s is a product term of the reduced DAC

of the probe and the one of the bulk bath particles; v_A is a fitting parameter describing the coupling strength between the bath particles and the probe. $\phi(t)$ is the reduced DAC of the N-bath particles $\phi_{\boldsymbol{q}}(t) := \Big\langle \rho_{\boldsymbol{q}} \Big| \rho_{\boldsymbol{q}}(t) \Big\rangle \Big/ \Big\langle \rho_{\boldsymbol{q}} \Big| \rho_{\boldsymbol{q}} \Big\rangle$.

Assume that the N-bath particle system is large enough so that its DAC is not affected by the external pulling force. Consequently, the DAC of the bulk bath particles can be described by the equilibrium MCT equation. So the dynamics of the reduced DAC of the bath particles $\phi(t)$ is just the standard schematic model,

$$\boxed{\begin{gathered} \ddot{\phi}(t) + \nu\dot{\phi}(t) + \Omega^2\phi(t) + \int_0^t d\tau\, M(t-\tau)\dot{\phi}(\tau) = 0 \\ M(t) = v_1\phi(t) + v_2\phi^2(t) \end{gathered}} \tag{5.100}$$

where the memory term is a non-linear combination of the reduced DAC of the bath particles. The control parameters (v_1, v_2) of the bath particles determine the liquid or glassy state together with the distance of a chosen state point from a glass-transition line. In this case, the schematic models can be calculated analytically [52]. The state points

$$(v_1, v_2) = [v_1^c(1+\sigma), v_2^c(1+\sigma)] \tag{5.101}$$

are specified by a distance σ to the transition line given by $v_1^c = v_2^c(2/\sqrt{v_2^c} - 1)$ with the specific choice $v_2^c = 2$ for the transition point. For simplicity, we fixed the damping term and the frequency term of the bulk to be unit values $\nu = \Omega^2 = 1$.

The combination of eq.(5.98) and eq.(5.100) construct a simplified MCT equation, which is reduced to a standard F_{12} model in the case $F_{ex} = 0$. The only control parameter of the bath particles' DAC is the distance to the glass transition line σ by controlling the value of (v_1, v_2) in the memory term explicitly according to eq.(5.101). Except for σ, the control parameters of the probe's DAC are the coupling strength v_A, and the pulling force F_{ex}.

With inputting parameters σ, v_A and F_{ex}, we can obtain the reduced DACs $\phi^s(t)$ and $\phi(t)$ based on eq. (5.98) and eq.(5.100). Consequently, the relative effective friction of the probe can be calculated through

$$\gamma_{eff}/\gamma = 1 + v_A \int_0^\infty \phi^{s*}(t')\phi(t')dt' \tag{5.102}$$

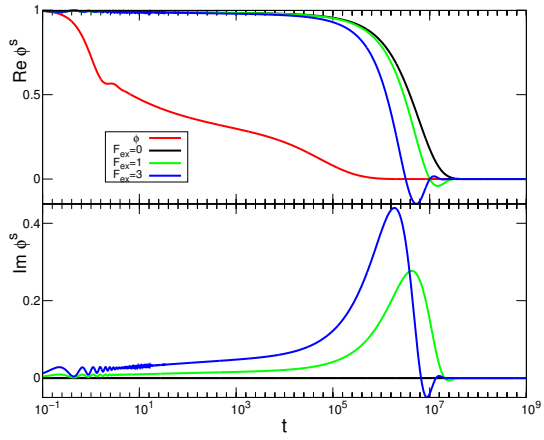

Figure 5.1: Schematic model calculation of the DACs of the probe particle for different pulling force $F_{ex} = 0, 1, 3$. The real and imaginary parts of the probe's DACs are plotted by numerical solution of the schematic model eq. (5.98) and eq. (5.100). The DAC of the bath particles are plotted in the red line. The parameters are $\nu = \Omega = 1$, $\nu_s = 1$, $\Omega_s = 1 - iF_{ex}$, $v_A = 200$ and $\sigma = -0.01$.

divergence problem of the schematic-model

Now we numerically solve the schematic model equations (5.98) and (5.100) with the fixed parameters mentioned above ($\nu = \Omega = 1$, $\nu_s = 1$, $\Omega_s = 1 - iF_{ex}$). And we choose the distance parameter as $\sigma = -0.01$ and the coupling strength between the probe and bath particles as $v_A = 200$. The numerical results are shown in fig.5.1.

In the small pulling force regimes, with increasing of the pulling force, the amplitude of the oscillation of the DACs increases, which is consistent with the behaviours of the probe's DAC in the low density limit. However, as the pulling force increases to $F_{ex} = 5$ (not plotted), the probe's DAC starts to exponentially increase, which is obviously unphysical due to the fact that the original probe's DAC should be normalized ($|\phi^s_{\boldsymbol{q}}(t)| = \left|\left\langle e^{i\boldsymbol{q}\cdot(\boldsymbol{r}_s(t)-\boldsymbol{r}_s}\right\rangle\right| = 1$).

Where does the divergence come from? The schematic model without memory term may be convergent, since it is possible that the simplifying of the MCT mem-

ory kernel causes the divergence, and for $M_s = 0$ (by setting $v_A = 0$), the model should be just a simple damped oscillator However, surprisingly, for the same parameters excluding $v_A = 0$, the model is still divergent, and even worse, the probe's DAC starts to be divergent at smaller force $F_{ex} = 2$ (Note that with memory term $v_A = 200$, the DAC is still convergent at $F_{ex} = 3$).

force dependent damping term $\nu_s(F_{ex})$

To clarify the origin of the divergence, let us analyse the schematic model without the memory kernel, i.e.

$$\ddot{\phi}_s(t) + \nu_s\dot{\phi}_s(t) + \Omega_s^2\phi_s(t) = 0 \tag{5.103}$$

with $\Omega_s^2 = 1 - iF_{ex}$. The exact solution is [2]

$$\phi^s(t) = (\frac{1}{2} + \frac{\nu_s}{4\beta})\exp\big\{(-\frac{\nu_s}{2} + \beta)t\big\} + (\frac{1}{2} - \frac{\nu_s}{4\beta})\exp\big\{(-\frac{\nu_s}{2} - \beta)t\big\}, \tag{5.104}$$

where $\beta = \sqrt{(\frac{\nu_s}{2})^2 - \Omega_s^2}$, and we have input the initial conditions $\phi^s(0) = 1$ and $\dot{\phi}^s(0) = 0$.

Note that different from the solution for the real parameters as discussed, where the correlator is always bounded (either under-damped or over-damped), the solution for the complex parameter can exponentially increase by noting that the solution has the term $e^{(-\frac{\nu_s}{2}\pm\beta)t}$ with $\beta = \sqrt{(\frac{\nu_s}{2})^2 - \Omega_s^2}$. The convergence condition $\phi^s(t \to \infty) < \infty$ requires that

$$\mathbf{Re}\frac{\nu_s}{2} > \big|\mathbf{Re}\beta\big| \tag{5.105}$$

For $\Omega_s^2 = 1 - iF_{ex}$ and real ν_s, it leads to

$$\boxed{\nu_s > F_{ex}\,!} \tag{5.106}$$

Surprisingly, different from equilibrium MCT and the corresponding schematic model, the damping term must depend on the pulling force. In the former case, ν_s is set to be a constant due to its irrelevance with the long time glassy dynamics.

[2] The general solution can be readily got by setting $\phi^s(t) = Ae^{\alpha t}$, $\alpha \in \mathbb{C}$. Inputting it into eq. (5.103), one gets $\alpha^2 + \nu_s\alpha + \Omega_s^2 = 0$, so $\alpha = \frac{1}{2}\big(-\nu_s \pm \sqrt{\nu_s^2 - 4\Omega_s^2}\big)$.

Under the convergence condition (5.106), we propose two possible sets of $\nu_s(F_{ex})$: (a) $\nu_s = 1 + F_{ex}$ and (b) $\nu_s = 1 + F_{ex}^2$. The numerical solutions for the force dependent friction are plotted in fig.5.2, where

$$\sigma(\bar{\varphi}) := (\bar{\varphi} - \bar{\varphi}^c)/\bar{\varphi}^c \tag{5.107}$$

is the reduced parameter of glass transition with $\bar{\varphi}^c$ denoting the parameter of the critical point of the transition.

The diagram of the probe's effective friction can be separated into three regimes, see fig.5.2:

1. Linear response regime: the friction coefficient is constant within a certain range of small pulling forces, or equivalently, the average velocity of the probe is proportional to the external pulling force.

2. Force thinning regime: the friction coefficient tends to decay to the value near to the bare friction coefficient with the increasing of the pulling force.

3. Large force pulling regime: only in this regime, significant difference of Fig. 5.2 (a) and Fig. 5.2 (b) is exhibited. The friction coefficient in Fig.5.2(a) keeps constant asymptotically with increasing pulling force, while it starts to increase and tends to saturate asymptotically.

In general, Fig.5.2(a) is quite similar to the earlier schematic models for colloidal hard-sphere systems [27, 58, 68], and Fig.5.2(b) qualitatively exhibits the increasing friction coefficient found in a simulation of a granular hard sphere system [28], but fails to reproduce the scaling law $\zeta \propto \sqrt{F_{ex}}$ in it.

5.4.2 Comparison with simulation data

We apply our schematic model to fit a simulation result of pulling in driven granular systems

Simulation details

The simulation is performed by M. Grob and A. Zippelius, the simulation details is addressed by them in ref [57] as follows:

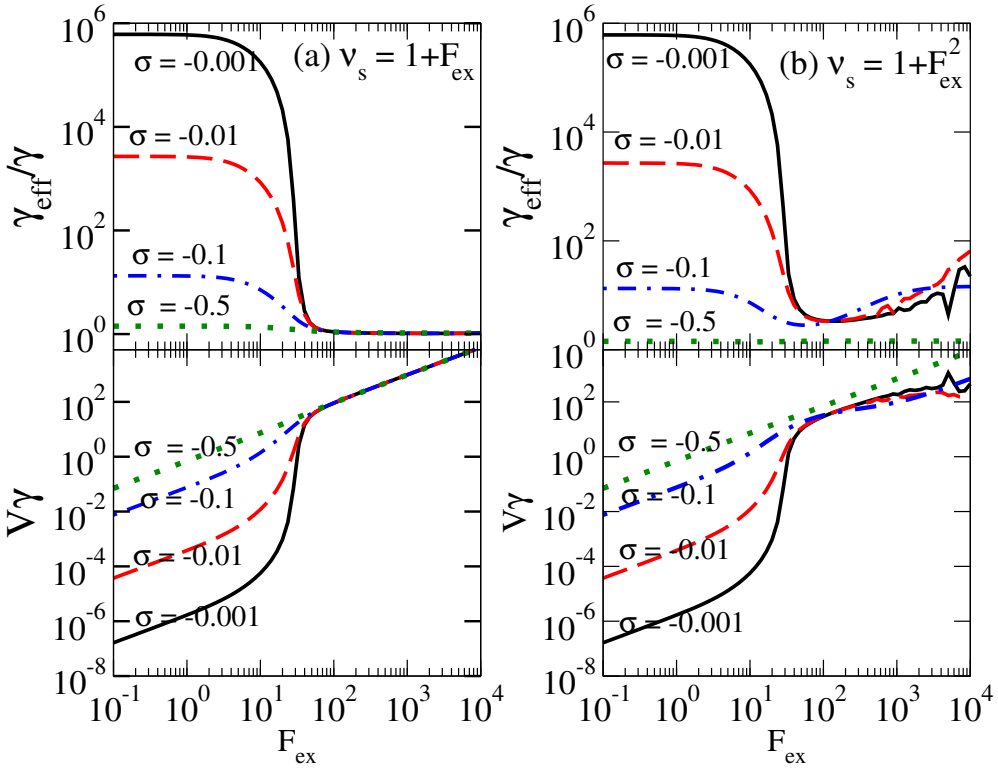

Figure 5.2: Force-Friction coefficient relation is shown for different $\nu_s(F_{ex})$. $\sigma = (\bar{\varphi} - \bar{\varphi}^c)/\bar{\varphi}^c$ is the distance to the transition point. $\bar{\varphi}^c$ is critical parameter for the glass transition.

The simulation is performed in two dimensions and the setup is the same as described in ref. [28]. In a bidisperse mixture of hard disks with size ratio $R_s/R_b = 4/5$ of small to big particles and a respective mass ratio $m_s/m_b = 16/25$, an intruder of radius $R_0 = 2R_s$ and mass $m_0 = 4m_s$ is suspended. All collisions are inelastic, characterized by the coefficient of restitution, ϵ. The particles are kicked randomly to balance energy input and dissipation by drag and inelastic collisions. Lengths and masses are measured such that $R_s = 1$ and $m_s = 1$ and a time scale is set by requiring that the granular temperature $T_G = 1$ in the system with $F_{ex} = 0$. An event driven code is implemented to simulate $N = 1024$ particles for a wide range of F_{ex}.

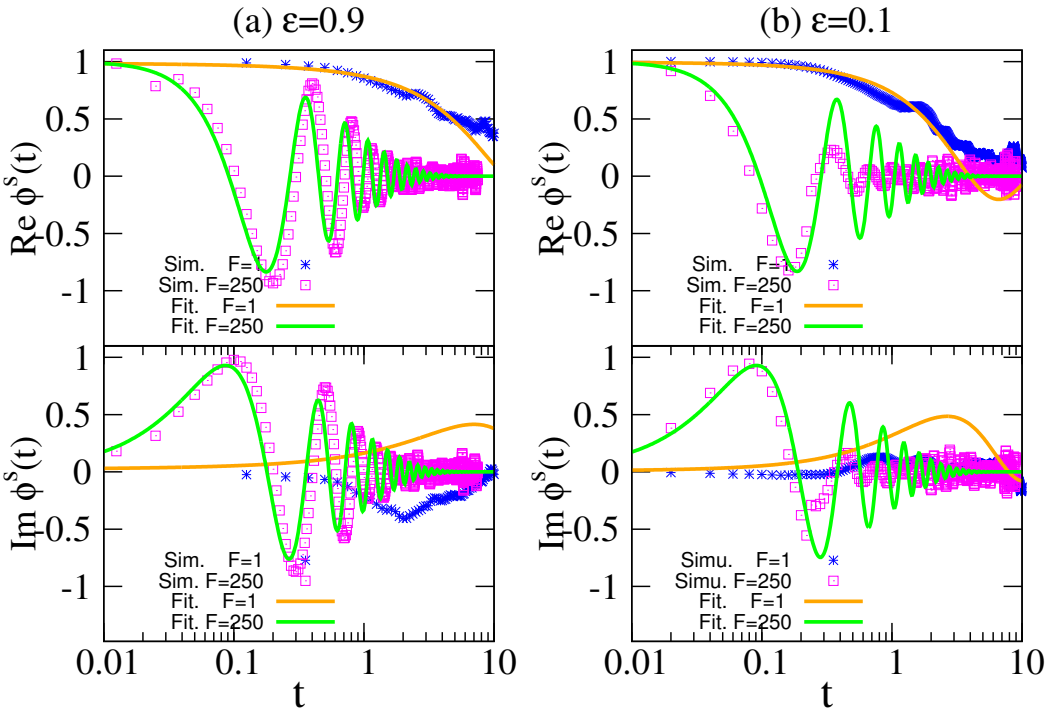

Figure 5.3: Fit of density autocorrelator of probe for different pulling force $F_{ex} = 1, 250$ under different energy dissipation $\varepsilon = 0.9, 0.1$. the Packing friction is fixed to $\varphi = 0.8$. Dashed line: simulation data; solid line: schematic fit.

Schematic model fitting

We adopt $\nu_s = 1 + F_{ex}^2$ as our schematic model to compare with the simulation data in detail due to this set of ν_s can show the increasing friction tendency. The fit of the DACP is given in fig. 5.3.

The numerical solution of the probe's DAC fits quite well with the corresponding simulation data for moderate force $F_{ex} = 250$. For small force $F_{ex} = 1$, it shows some deviation. The fit parameters are $v_A = 200$, $\sigma = -0.05$ for $\varepsilon = 0.9$ and $\sigma = -0.13$ for $\varepsilon = 0.1$. The other parameters are the same as the ones mentioned above.

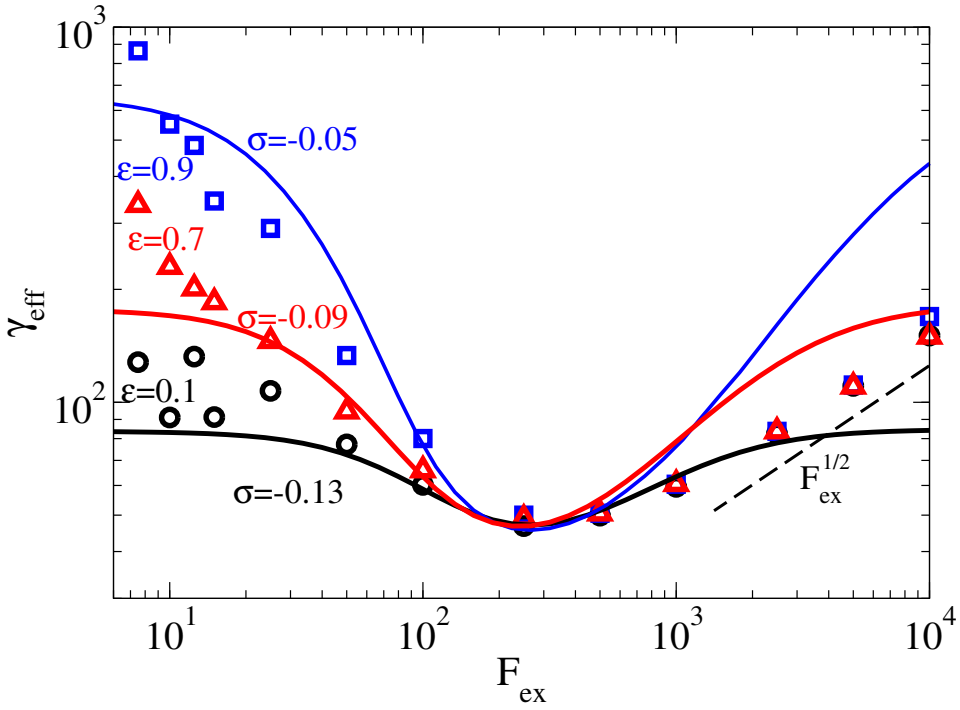

Figure 5.4: Fitting of the effective friction of the probe for different energy dissipation $\varepsilon = 0.9, 0.1$ with the fixed packing friction $\varphi = 0.8$. dashed line: simulation data; solid line: schematic fitting.

The corresponding fit of the friction is given according to the parameter set of the density autocorrelator fit. The result is shown in Fig. 5.4. In the small force regime, our schematic model shows a plateau while the simulation data tends to jump to a large value for $F_{ex} < 10$. The deviation we think is mainly due to the inaccuracy of simulation in this small force regime. The error bar of the simulation data can be comparable with the result itself. This large error may cause from comparable large thermal fluctuation for small pulling force $k_BT/(F_{ex}R)$, where R is particle size. In large force regime, the model can only qualitatively show the increasing friction coefficient as mentioned above.

Physics: dissipation melt the glass

Though the schematic model only qualitatively fits the simulation data, it confirms the physics picture from the earlier MCT calculation of the driven granular parti-

cles: energy dissipation plays a negative role to the glass transition [69, 70, 71].

In detail, see the small and moderate external pulling force regime ($F_{ex} < 100$) in Fig.5.4. For a fixed force F_{ex}, two important observations are that

1. The event driven simulation result shows that the effective friction of the probe decreases with the increasing energy dissipation rate $1 - \varepsilon^2$

2. The fit by the schematic model shows that the distance σ to the glass transition line of the host system should increase with the increasing energy dissipation rate.

These observations indicate that the rigidity of the system decreases with the increase of the energy dissipation, which is the main point in refs [69, 70, 71].

5.4.3 Microscopic derivation of $\nu_s(F_{ex})$

What's the microscopic origin of the force dependent friction term $\nu_s(F_{ex})$? Note that on one hand the slow dynamics is captured by the mode-coupling approximation (MCA), but the fast dynamics is ignored by the MCA due to its irrelevance to the slow glassy dynamics; on the other hand, in the large pulling force regime, the fast external driving dynamics dominates over the intrinsic slow glassy dynamics[3]. Therefore, it is important to extract the fast dynamics in the memory kernel of the MZ equation (5.76). Let us separate the exact memory kernel in the MZ equation (5.76) into two parts

$$M_q^s(t) \approx M_q^{s,F_{ex}}(t) + M_q^{s,MCT}(t) \tag{5.108}$$

The MCT part of the kernel is given in the MCA equation (5.96), which originated from the probe-bath particles interactions $\boldsymbol{F}_s^{int}$ in high density. To extract the short time dynamics, let us consider the Taylor expansion of the memory kernel of the

[3]So the divergence of the schematic model without force dependent damping term is understandable.

MZ equation with the approximation $\boldsymbol{F}_s^{int} = 0$ [4]

$$\begin{aligned} M_q^s(t) &= -\frac{m_s}{k_B T}\Big\langle \mathcal{QL}_{FP}^\dagger j_{\boldsymbol{q}_L}^s \Big| e^{\mathcal{QL}_{FP}t}\Big| \mathcal{QL}_{FP} j_{\boldsymbol{q}_L}^s \Big\rangle \\ &= -\frac{m_s}{k_B T}\Big\langle \mathcal{QL}_{FP}^\dagger j_{\boldsymbol{q}_L}^s \Big| \big[1 + \mathcal{QL}_{FP}t + \frac{t^2}{2}(\mathcal{QL}_{FP})^2 \\ &\qquad + \frac{t^3}{6}(\mathcal{QL}_{FP})^3 + O(t^4)\big]\Big| \mathcal{QL}_{FP} j_{\boldsymbol{q}_L}^s \Big\rangle \end{aligned} \tag{5.109}$$

Note that

$$\begin{aligned} \mathcal{L}_{FP}\Big| j_{\boldsymbol{q}_L}^s \Big\rangle &= iq{v_s^L}^2 \Big| \rho_{\boldsymbol{q}}^s \Big\rangle + \frac{F_{s\,L}^{int} - \gamma v_s^L + F_{ex}^L}{m}\Big| \rho_{\boldsymbol{q}}^s \Big\rangle \\ \mathcal{PL}_{FP}\Big| j_{\boldsymbol{q}_L}^s \Big\rangle &= \frac{iqk_BT + F_{ex}^L}{m}\Big| \rho_{\boldsymbol{q}}^s \Big\rangle - \frac{\gamma}{m}\Big| j_{\boldsymbol{q}_L}^s \Big\rangle \\ \mathcal{QL}_{FP}\Big| j_{\boldsymbol{q}_L}^s \Big\rangle &= \frac{F_{s\,L}^{int} - iqk_BT}{m}|\rho_{\boldsymbol{q}}^s\Big\rangle + iq{v_s^L}^2 |\rho_{\boldsymbol{q}}^s\Big\rangle \\ \Big\langle \mathcal{L}_{FP}^\dagger j_{\boldsymbol{q}_L}^s \Big| &= \Big\langle -iq{v_s^L}^2 \rho_{\boldsymbol{q}}^s \Big| + \Big\langle \frac{-F_{s\,L}^{int} - \gamma v_s^L - F_{ex}}{m}\rho_{\boldsymbol{q}}^s \Big| + \Big\langle \frac{F_{ex}^L}{k_BT}{v_s^L}^2 \rho_{\boldsymbol{q}}^s \Big| \end{aligned} \tag{5.110}$$

We set $F_{s\,L}^{int} = 0$. And by tedious but straightforward calculation, we obtain

$$\begin{aligned} a_0 &= \Big\langle \mathcal{QL}_{FP}^\dagger j_{\boldsymbol{q}_L}^s \Big| \mathcal{QL}_{FP} j_{\boldsymbol{q}_L}^s \Big\rangle = -\frac{-2iqk_BTF_{\text{ex}} + 2q^2(k_BT)^2}{m_s^2} \\ a_1 &= \Big\langle \mathcal{QL}_{FP}^\dagger j_{\boldsymbol{q}_L}^s \Big| (\mathcal{QL}_{FP})^2 j_{\boldsymbol{q}_L}^s \Big\rangle = \frac{4\gamma qk_BT\left(qk_BT - iF_{\text{ex}}\right)}{m_s^3} \\ a_2 &= \Big\langle \mathcal{QL}_{FP}^\dagger j_{\boldsymbol{q}_L}^s \Big| (\mathcal{QL}_{FP})^3 j_{\boldsymbol{q}_L}^s \Big\rangle \\ &= -\frac{qk_BT\left(qk_BT - iF_{\text{ex}}\right)\left[8\gamma^2 + 3qm_s\left(3qk_BT + 2iF_{\text{ex}}\right)\right]}{m_s^4} \\ a_3 &= \Big\langle \mathcal{QL}_{FP}^\dagger j_{\boldsymbol{q}_L}^s \Big| (\mathcal{QL}_{FP})^4 j_{\boldsymbol{q}_L}^s \Big\rangle \\ &= \frac{\gamma qk_BT\left(qk_BT - iF_{\text{ex}}\right)\left[16\gamma^2 + 3qm_s\left(31qk_BT + 14iF_{\text{ex}}\right)\right]}{m_s^5} \end{aligned} \tag{5.111}$$

where we have used the Gaussian property of v_s^L due to the Maxwellian distribution of the velocity in the initial equilibrium state

$$\Big\langle {v_s^L}^4 \Big\rangle = 3(\frac{k_BT}{m})^2. \tag{5.112}$$

[4] Since the interaction force is assumed to be captured in the memory kernel of the MCA.

Thus the Taylor expansion of the memory kernel without the interaction force F_{sL}^{int} is

$$M_q^{s,F_{ex}}(t) \approx M_q^s(t)\Big|_{F_{sL}^{int}=0} = a_0 + a_1 t + a_2\frac{t^2}{2} + a_3\frac{t^3}{6} + O(t^4)$$

Furthermore, assuming that $M_q^{s,F_{ex}}(t)$ decays so fast that it can be approximated by a delta function as

$$M_q^{s,F_{ex}}(t) \approx \left[a_0 + a_1\tau_0 + a_2\frac{\tau_0^2}{2} + a_3\frac{\tau_0^3}{6}\right]\tau_0\delta(t)$$

where τ_0 is a typical decay time scale. Correspondingly,

$$\begin{aligned}\int_0^t d\tau\, M_q^{s,F_{ex}}(t-\tau)\dot{\phi}_{\boldsymbol{q}}^s(\tau) &\approx \left[a_0 + a_1\tau_0 + a_2\frac{\tau_0^2}{2} + a_3\frac{\tau_0^3}{6}\right]\tau_0\dot{\phi}_{\boldsymbol{q}}^s(t) \\ &\approx \nu_s'(F_{ex})\dot{\phi}_{\boldsymbol{q}}^s(t)\end{aligned} \tag{5.113}$$

Interestingly, the damping term has an additional force dependent term $\nu_s'(F_{ex})$, which means that the short time dynamics depends on the pulling force. This may be a crucial point for the calculation of the effective friction of the probe by MCT. The failure of earlier microscopic MCT calculation refs.[27, 47] in the moderate pulling force regime may come from the lack of force dependent short time decay of the DAC. In refs. [27, 47], the force is coupled to the density pair only, see eq. (79) in [47].

The MZ equation now can be reformulated as follows

$$\boxed{\begin{aligned}\ddot{\phi}_{\boldsymbol{q}}^s(t) + \left\{\frac{\gamma}{m} + \nu_s'(F_{ex})\right\}\dot{\phi}_{\boldsymbol{q}}^s(t) + (q^2\frac{k_BT}{m} - \frac{i\boldsymbol{F}_{ex}\cdot\boldsymbol{q}}{m_s})\phi_{\boldsymbol{q}}^s(t) \\ + \int_0^t d\tau\, M_q^{s,MCT}(t-\tau)\dot{\phi}_{\boldsymbol{q}}^s(\tau) = 0\end{aligned}} \tag{5.114}$$

Note that $\nu_s = \frac{\gamma}{m} + \nu_s'(F_{ex})$, the corresponding schematic model is

$$\nu_s = 1 + F_{ex}^2 - iF_{ex} \tag{5.115}$$

which can be obtained by considering the terms contained in the eq. (5.111). The relative effective friction vs. the pulling force is shown in fig. 5.5. It exhibits both thinning and thickening, and the thickening part saturates to a second plateau value. The result is similar to the set $v_A = 1 + F_{ex}^2$. So here we do not use it to fit the simulation data again.

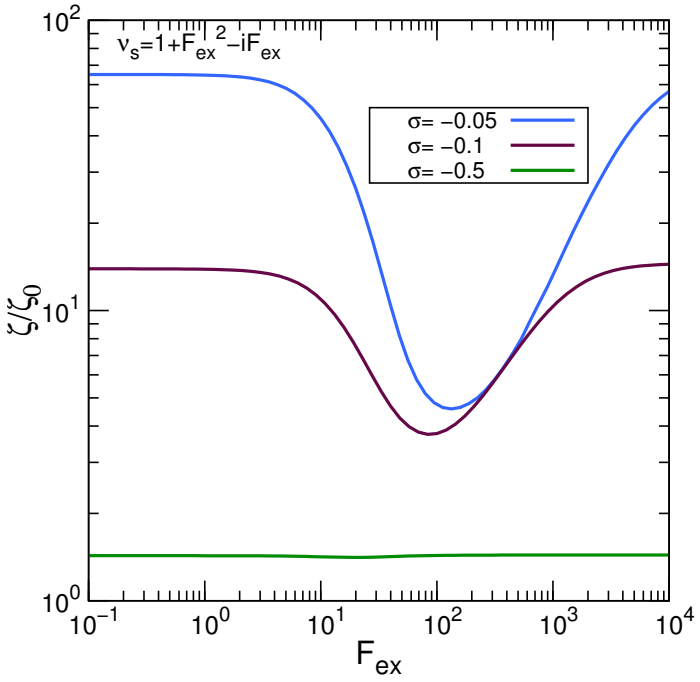

Figure 5.5: Schematic model calculation of the effective friction of the probe for different force. The damping term ν_s is as indicated in the figure. σ is the reduced packing fraction.

5.4.4 What's new

In this chapter, we derive a microscopic MCT equation for the probe particle and construct the corresponding schematic-MCT model. Different from earlier MCT on the microrheology refs. [27, 47], here we consider the under damping system and correspondingly we use the Fokker-Planck dynamics (the phase space and operators are have both position and velocity parts) but not the Smoluchowski dynamics (the phase space and operators depends on the position only). The main results are summarized as follows

1. We find the damping term ν_s should depend on the pulling force $\nu_s(F_{ex})$, which is different from earlier standard MCT [52] . In the standart MCT, the damping is treated as a constant value representing the dynamics of simple liquid, and is irrelevant with the long time glassy dynamics. However, in our non-equilibrium system, the microrheology, we find that the damping

term must depend on the pulling force, otherwise the probe's DAC will be divergent, which suggests that the earlier MCT treatment for the microrheology [27, 47] may not fully capture the force dependence of the probe's effective friction.

2. Furthermore, we find the explicit form of the $\nu_s(F_{ex})$ affects the behaviour of the probe's friction in the large pulling force regime. If ν_s is only related to the linear term F_{ex} or iF_{ex}, only thinning is observed in the large force regime. However, If ν_s depends on F_{ex}^2, then also increasing friction, i.e., thickening can be observed.

3. We use $\nu_s = 1 + F_{ex}^2$ to fit the experimental result of the microrheology for the driven granular hard-sphere system, and find the schematic model works in the small and moderate force regimes, and can exhibit increasing friction, though the scaling behaviour cannot be captured.

4. Microscopically, we also give the derivation of the force dependence of ν_s by Taylor expansion of the memory kernel by assuming that the interaction force is included in the MCA kernel and only consider $F_{s,L}^{int} = 0$ for the expansion.

In short, the most interesting part of our MCT is that we find the damping term ν in the MZ equation should depend on force, which affects not only the convergence of the probe's DAC, but also affect the behaviour (thickening or not) of the probe in large force regime.

Chapter 6

Conclusion and discussion

6.1 Conclusion

In this thesis, we investigate the non-linear response in active microrheology. In particular, starting from the under-damped Langevin dynamics, we extend the earlier two-body Smoluchowski equation [24] in low density and MCT [27, 47] in high density, both to include thickening. The mechanism of thickening is also clarified in the low density limit by a simple kinetic model and a Langevin dynamics simulation.

In chapter 1, we construct a simple point like collision model. The key idea is that assuming the many body interaction between probe-bath particles can be reduced to two body probe-bath particle collision, and considering the interaction as a series of discrete collisions. We find that inertia causing thickening. Thickening depends on the two time scales, velocity damping of a bath particle, and the collision between probe and a single bath particle. When collision dominates, thickening happens. In addition, by applying the stability of fixed point analysis, we find the dissipative collisions between particles are not essential for thickening.

In chapter 2, we extend the model to include the thinning regime, and unify the thinning and thickening by a three-time-scales picture, see fig. 3.1. The point is that thinning/thickening is determined by the dominating one of three distinctive processes (or time scales) of bath particles: diffusion, damping and single probe-bath particles collision. In detail, for small pulling velocity, the diffusion time scale dominates, which results in a high a high plateau of the effective friction of

the probe. As the velocity is much larger than the bath particle's diffusion, the diffusion can be ignored, damping dominates. The friction decreases to a lower plateau, i.e., thinning occurs. And as the pulling velocity is so large, that the collision between probe bath particles dominates over the damping, the friction starts to increase, i.e. thickening occurs. This time scale picture is confirmed by a Langevin dynamics without considering the interaction between bath particles.

Furthermore, in chapter 3, in the low density limit, we discuss the microscopic mechanism of thickening. We find the crossover from the creep motion around the probe-bath contact surface of a bath particle to the direct single collision only with the probe is the microscopic picture for the thickening, see fig. 4.1.

In the high density, in chapter 4, we extend the MCT to include the force-dependent short time decay, which is crucial for thickening. First we construct a schematic-MCT model, which can exhibit thickening behaviour as the friction contains the square of the force. And we apply it to fit simulation data of pulling in driven granular particles. Microscopically, the force dependent memory term in the schematic model is obtained by a MCT calculation. Comparing the MCT calculation in the thesis with the MCT in refs. [27, 47], except for the difference of the microscopic dynamics[1], in our calculation, a short decay and force dependent memory term is introduced to reproduce thickening, while in refs. [27, 47], no such short time decay term and thickening was included.

6.2 Discussion

In the low density limit, as far as we know, our Langevin dynamics simulation (or equivalently the numerical solution of a two-body Fokker-Planck equation) is the first result demonstrating that both thinning and thickening can occur in the low density limit. While earlier the Stokes dynamical simulation [31] and the analytical calculation based on a two-body Smoluchowski equation [24] can only capture thinning, but not thickening.

The non-linear behaviour of thinning and thickening can be unified by the three-time-scale picture (confirmed by the Langevin dynamics simulation). This fact tells us that the essence of "non-linear" in low density limit is just the interplay

[1] our calculation is based on the under-damped Fokker-Planck equation, while the earlier is based on the over-damped Smoluchowski dynamics

of different dominating time scales. The failure of reproducing thickening by the over-damped dynamics, Stokes [31] or Smoluchowski [24], suggests that as the system is driven far away from equilibrium, the inertia time scale is missing, and the velocity distribution can no longer be simply assumed as the Maxwellian distribution. While the under-damped dynamics, Langevin or Fokker-Planck, explicitly includes the velocity information, which can be applied from the range of near to equilibrium to far way from equilibrium.

In high density, it is interesting to investigate how does the many body interaction modify the time scales picture, especially the following prediction of the the three-time-scale picture: the onset of thinning should shift to smaller pulling velocity regime, and the onset of thickening should shift to larger one, since the effective solvent friction of the bath particles increases due to interaction.

For the MCT, we separate the memory term into two parts, $M = M^{F_{ex}} + M^{MCT}$. The force dependent term $M^{F_{ex}}$ is required for large pulling force, otherwise the density autocorrelator becomes unphysical: it increases exponentially. This finding suggests that strong external driving may destroy the collective slow dynamics, resulting in a fast dynamics. Correspondingly, for strong driving, in the Mori-Zwanzig equation, the dynamics of the density autocorrelator may be controlled by the memory term of the external driving but not the memory term of the MCT kernel. It is interesting to see microscopically how does the driving destroy the collective motion in high density.

Appendices

Appendix A

Operators of the Fokker-Planck Equation

Here we give the derivation of the Fokker-Planck equation, which is the starting point of the MCT calculation in the thesis.

Probability Operator

The probability evolution operator Ω is defined according to

$$\partial_t P(\Gamma, t) = \hat{\Omega} P(\Gamma, t). \tag{A.1}$$

Explicitly,

$$\Omega = -\partial_{\mathbf{\Gamma}} \cdot \dot{\mathbf{\Gamma}} - \dot{\mathbf{\Gamma}} \cdot \partial_{\mathbf{\Gamma}}, \tag{A.2}$$

In particular, for FP dynamics, the probability evolution operator reads

$$\boxed{\hat{\Omega}_{FP} = \underbrace{-\left[\boldsymbol{v}_i \cdot \partial_{\boldsymbol{r}_i} + \frac{\boldsymbol{F}_i}{m} \cdot \partial_{\boldsymbol{v}_i}\right]}_{\hat{\Omega}^0_{FP}} + \underbrace{\frac{\gamma}{m} \partial_{\boldsymbol{v}_i} \cdot \left[\boldsymbol{v}_i + \frac{k_B T}{m} \partial_{\boldsymbol{v}_i}\right]}_{\hat{\Omega}^1_{FP}} \underbrace{- \frac{\boldsymbol{F}_{ex}}{m} \cdot \partial_{\boldsymbol{v}_s}}_{\hat{\Omega}^{ex}_{FP}}} \tag{A.3}$$

where $\boldsymbol{F}_i = -\partial_{\boldsymbol{r}_i} U(\mathbf{\Gamma}_{\boldsymbol{r}})$. (See Risken eq. (4.113).)

Dynamics Operator $\mathcal{L}_{FP}$

The dynamical operator of a phase space variable is just the adjoin operator of the probability operator,

$$\int d\mathbf{\Gamma} \big(\hat{\Omega} A(\mathbf{\Gamma})\big) B(\mathbf{\Gamma}) = \int d\mathbf{\Gamma} A(\mathbf{\Gamma}) \mathcal{L}_{FP} B(\mathbf{\Gamma}) \tag{A.4}$$

because

$$\Big\langle A(t)\Big\rangle \equiv \int d\mathbf{\Gamma} P(\mathbf{\Gamma},t)A(\mathbf{\Gamma}) = \int d\mathbf{\Gamma}\Big[e^{\hat{\Omega}_{FP}t}P(\mathbf{\Gamma},0)\Big]A(\mathbf{\Gamma}) = \int d\mathbf{\Gamma} P(\mathbf{\Gamma},0)e^{\mathcal{L}_{FP}t}A(\mathbf{\Gamma}) \tag{A.5}$$

The explicit form of $\mathcal{L}_{FP}$ is

$$\boxed{\mathcal{L}_{FP} = \underbrace{\Big[\boldsymbol{v}_i\cdot\partial_{\boldsymbol{r}_i} + \frac{\boldsymbol{F}_i}{m}\cdot\partial_{\boldsymbol{v}_i}\Big]}_{\mathcal{L}^0_{FP}} + \underbrace{\frac{\gamma}{m}\Big[-\boldsymbol{v}_i + \frac{k_BT}{m}\partial_{\boldsymbol{v}_i}\Big]\cdot\partial_{\boldsymbol{v}_i}}_{\mathcal{L}^1_{FP}} + \underbrace{\frac{\boldsymbol{F}_{ex}}{m}\cdot\partial_{\boldsymbol{v}_s}}_{\mathcal{L}^{ex}_{FP}}} \tag{A.6}$$

which can be easily obtained by noting that

$$\begin{aligned}\int d\mathbf{\Gamma} A(\mathbf{\Gamma})\partial_i B(\mathbf{\Gamma}) &= \int d\mathbf{\Gamma}' A(\mathbf{\Gamma})B(\mathbf{\Gamma})|_{bound\,i} - \int d\mathbf{\Gamma} B(\mathbf{\Gamma})\partial_i A(\mathbf{\Gamma}) \\ &= -\int d\mathbf{\Gamma} B(\mathbf{\Gamma})\partial_i A(\mathbf{\Gamma})\end{aligned} \tag{A.7}$$

Its adjoint: $\mathcal{L}^\dagger_{FP}$

$\mathcal{L}^\dagger_{FP}$ as

$$\Big\langle A^*\mathcal{L}_{FP}B\Big\rangle_{eq} = \Big\langle(\mathcal{L}^\dagger_{FP}A)^*B\Big\rangle_{eq} \tag{A.8}$$

Explicitly,

$$\begin{aligned}\Big\langle A^*\mathcal{L}_{FP}B\Big\rangle_{eq} &= \int d\mathbf{\Gamma} P_{eq}A^*\mathcal{L}_{FP}B \\ &= \int d\mathbf{\Gamma}[(\hat{\Omega}^0_{FP} + \hat{\Omega}^1_{FP} + \hat{\Omega}^{ex}_{FP})(P_{eq}A^*)]B\end{aligned} \tag{A.9}$$

Calculate

$$\hat{\Omega}^0_{FP}(P_{eq}A^*)]B = [\hat{\Omega}^0_{FP}A^*]P_{eq}B \tag{A.10}$$

$$\begin{aligned}[\hat{\Omega}^1_{FP}(P_{eq}A^*)]B &= \frac{\gamma}{m}\Big\{\partial_{\boldsymbol{v}_i}\cdot\Big[\boldsymbol{v}_i + \frac{k_BT}{m}\partial_{\boldsymbol{v}_i}\Big](P_{eq}A^*)\Big\}B \\ &= \frac{\gamma}{m}\Big\{\partial_{\boldsymbol{v}_i}\cdot\Big[\boldsymbol{v}_iA^* + \frac{k_BT}{m}\partial_{\boldsymbol{v}_i}A^* - \boldsymbol{v}_iA^*\Big]P_{eq}\Big\}B \\ &= \frac{\gamma}{m}\Big\{\partial_{\boldsymbol{v}_i}\cdot\Big[\frac{k_BT}{m}\partial_{\boldsymbol{v}_i}A^*\Big]P_{eq}\Big\}B \\ &= \Big\{\Big[\frac{\gamma k_BT}{m^2}\partial_{\boldsymbol{v}_i}\cdot\partial_{\boldsymbol{v}_i} - \frac{\gamma}{m}\boldsymbol{v}_i\cdot\partial_{\boldsymbol{v}_i}\Big]A^*\Big\}P_{eq}B\end{aligned} \tag{A.11}$$

and

$$\begin{aligned}[\hat{\Omega}^{ex}_{FP}(P_{eq}A^*)]B &= \Big[-\frac{\boldsymbol{F}_{ex}}{m}\cdot\partial_{\boldsymbol{v}_s}(P_{eq}A^*)\Big]B \\ &= \Big\{ -\frac{\boldsymbol{F}_{ex}}{m}\cdot\Big[\partial_{\boldsymbol{v}_s}-\frac{m_i\boldsymbol{v}_i}{k_BT}\Big]A^*\Big\}P_{eq}B\end{aligned} \tag{A.12}$$

where we have applied the properties $P_{eq}=\frac{1}{Z}e^{-\frac{U+\frac{1}{2}m_i\boldsymbol{v}_i\cdot\boldsymbol{v}_i}{k_BT}}$, $\partial_{\boldsymbol{r}_i}P_{eq}=P_{eq}\frac{\boldsymbol{F}_i}{k_BT}$ and $\partial_{\boldsymbol{v}_i}P_{eq}=-P_{eq}\frac{m_i\boldsymbol{v}_i}{k_BT}$.

Collecting all the terms, we get

$$\boxed{\mathcal{L}^{\dagger}_{FP}=\underbrace{-\Big[\boldsymbol{v}_i\cdot\partial_{\boldsymbol{r}_i}+\frac{\boldsymbol{F}_i}{m}\cdot\partial_{\boldsymbol{v}_i}\Big]}_{\mathcal{L}^{\dagger\,0}_{FP}}+\underbrace{\frac{\gamma}{m}\Big[-\boldsymbol{v}_i+\frac{k_BT}{m}\partial_{\boldsymbol{v}_i}\Big]\cdot\partial_{\boldsymbol{v}_i}}_{\mathcal{L}^{\dagger\,1}_{FP}}+\underbrace{\frac{\boldsymbol{F}_{ex}}{m}\cdot\Big[-\partial_{\boldsymbol{v}_s}+\frac{m\boldsymbol{v}_s}{k_BT}\Big]}_{\mathcal{L}^{\dagger\,ex}_{FP}}}} \tag{A.13}$$

Bibliography

[1] R. G. Larson. *The Structure and Rheology of Complex Fluids*. Oxford University Press, New York, 1999.

[2] G. Elisabeth and J. Morris. *A physical introduction to suspension dynamics*. Cambridge University Press, Cambridge New York, 2012.

[3] Daniel T.N. Chen, Qi Wen, Paul A. Janmey, John C. Crocker, and Arjun G. Yodh. Rheology of Soft Materials. *Annual Review of Condensed Matter Physics*, 1(1):301–322, 2010.

[4] T. Waigh. Microrheology of complex fluids. *Reports on Progress in Physics*, 68(3):685–742, 2005.

[5] P. Cicuta and A. Donald. Microrheology: a review of the method and applications. *Soft Matter*, 3(12):1449, 2007.

[6] Todd M. Squires and Thomas G. Mason. Fluid Mechanics of Microrheology. *Annu. Rev. Fluid Mech.*, 42(1):413–438, 2010.

[7] A. Puertas and T. Voigtmann. Microrheology of colloidal systems. *J. Phys.: Condens. Matter*, 26(24):243101, 2014.

[8] T. Mason and D. Weitz. Optical Measurements of Frequency-Dependent Linear Viscoelastic Moduli of Complex Fluids. *Phys. Rev. Lett.*, 74(7):1250–1253, 1995.

[9] Th. Moschakis, B. Murray, and E. Dickinson. Particle tracking using confocal microscopy to probe the microrheology in a phase-separating emulsion containing nonadsorbing polysaccharide. *Langmuir : the ACS journal of surfaces and colloids*, 22(10):4710–9, 2006.

[10] P. Habdas, A. C. Levitt D. Schaar, and E. R. Weeks. Forced motion of a probe particle near the colloidal glass transition. *Europhys. Lett.*, 67(3):477–483, 2004.

[11] D. Anderson, D. Schaar, H. Hentschel, J. Hay, P. Habdas, and E. Weeks. Local elastic response measured near the colloidal glass transition. *J. Chem. Phys.*, 138:12A520, 2013.

[12] C. Olson Reichardt and C. Reichardt. Fluctuations, jamming, and yielding for a driven probe particle in disordered disk assemblies. *Physical Review E*, 82(5):051306, November 2010.

[13] Yuka Takehara, Sachika Fujimoto, and Ko Okumura. High-velocity drag friction in dense granular media. *Europhys. Lett.*, 92(4):44003, 2010.

[14] Y. Takehara and K. Okumura. High-Velocity Drag Friction in Granular Media near the Jamming Point. *Phys. Rev. Lett.*, 112(14):148001, April 2014.

[15] T. Mason and D. Weitz. Optical Measurements of Frequency-Dependent Linear Viscoelastic Moduli of Complex Fluids. *Phys. Rev. Lett.*, 74(7):1250–1253, 1995.

[16] L. Wilson and W. Poon. Small-world rheology: an introduction to probe-based active microrheology. *Phys. Chem. Chem. Phys*, 13(22):10617–10630, 2011.

[17] R. Candelier and O. Dauchot. Creep Motion of an Intruder within a Granular Glass Close to Jamming. *Phys. Rev. Lett.*, 103(12):128001, 2009.

[18] C. Coulais, A. Seguin, and O. Dauchot. Shear modulus and Dilatancy Softening in Granular Packings above Jamming. *Phys. Rev. Lett.*, 113(November):198001, 2014.

[19] R Kubo, M Toda, and N. Hashitsume. *Statistical Physics II: Nonequilibrium Statistical Mechanics*. Springer, 2nd edition, 2003.

[20] D. Evans and G. Morriss. *Statistical mechanics of nonequilibrium liquids*. Cambridge University Press, 2nd ed. edition, 2008.

[21] U. Marconi, A. Puglisi, L. Rondoni, and A. Vulpiani. Fluctuation-dissipation: Response theory in statistical physics. *Phys. Rep.*, 461(4-6):111–195, 2008.

[22] U. Seifert. Stochastic thermodynamics, fluctuation theorems and molecular machines. *Rep. Prog. Phys.*, 75(12):126001, 2012.

[23] P. Hänggi and P. Talkner. The other QFT. *Nature Phys.*, 11(2):108–110, 2015.

[24] T. Squires and J. Brady. A simple paradigm for active and nonlinear microrheology. *Phys. Fluid*, 17(7):073101, 2005.

[25] J. Swan and R. Zia. Active microrheology: Fixed-velocity versus fixed-force. *Phys. Fluid*, 25(8):083303, 2013.

[26] P. Reardon, A. Graham, J. Abbott, and H. Brenner. Experimental observations of non-continuum effects in suspensions: Falling-ball versus towed-ball rheometry. *Phys. Fluid*, 17(9):093101, 2005.

[27] I. Gazuz, A. Puertas, Th. Voigtmann, and M. Fuchs. Active and Nonlinear Microrheology in Dense Colloidal Suspensions. *Phys. Rev. Lett.*, 102(24):248302, 2009.

[28] A. Fiege, M. Grob, and A. Zippelius. Dynamics of an intruder in dense granular fluids. *Granular Matter*, 14(2):247–252, 2012.

[29] L. Wilson, A. Harrison, A. Schofield, J. Arlt, and W. Poon. Passive and active microrheology of hard-sphere colloids. *J. Phys. Chem. B*, 113(12):3806–12, 2009.

[30] J. Gomez-Solano and C. Bechinger. Probing linear and nonlinear microrheology of viscoelastic fluids. *Europhys. Lett.*, 108(5):54008, 2014.

[31] I. Carpen and J. Brady. Microrheology of colloidal dispersions by Brownian dynamics simulations. *J. Rheol.*, 49(6):1483, 2005.

[32] D. Winter, J. Horbach, P. Virnau, and K. Binder. Active Nonlinear Microrheology in a Glass-Forming Yukawa Fluid. *Phys. Rev. Lett.*, 108(2):28303, 2012.

[33] S. Takada and H. Hayakawa. Drag Law of Two Dimensional Granular Fluids. *arXiv preprint*, page 13, 2015.

[34] W. Poon. *Colloidal Suspensions*. Clarendon Press, Oxford, 2012.

[35] N Brilliantov. *Kinetic theory of granular gases*. Oxford University Press, Oxford New York, 2004.

[36] G. Hunter and E. Weeks. The physics of the colloidal glass transition. *Rep. Prog. Phys.*, 75(6):66501, 2012.

[37] Hans Martin Laun. Rheological properties of aqueous polymer dispersions. *Die Angewandte Makromolekulare Chemie*, 123(1):335–359, 1984.

[38] X. Xu, S. Rice, and A. Dinner. Relation between ordering and shear thinning in colloidal suspensions. *Proc.Natl. Acad. Sci.*, 110(10):3771–6, 2013.

[39] B. Guy, M. Hermes, and W. C. K. Poon. A unified description of the rheology of hard-particle suspensions. *arXiv:1506.09041v1*, 2015.

[40] M Wyart and M Cates. Discontinuous Shear Thickening without Inertia in Dense Non-Brownian Suspensions. *Phys. Rev. Lett.*, 112(9):98302, 2014.

[41] Takeshi Kawasaki, Atsushi Ikeda, and Ludovic Berthier. Thinning or thickening? Multiple rheological regimes in dense suspensions of soft particles. *Europhys. Lett.*, 107(2):28009, 2014.

[42] N. Wagner and J. Brady. Shear thickening in colloidal dispersions. *Phys. Today*, page 27, 1999.

[43] R. Seto, R. Mari, J. Morris, and M. Denn. Discontinuous Shear Thickening of Frictional Hard-Sphere Suspensions. *Phys. Rev. Lett.*, 111(21):218301, November 2013.

[44] R. Bagnold. Experiments on a Gravity-Free Dispersion of Large Solid Spheres in a Newtonian Fluid under Shear. *Proceedings of the Royal Society A: Mathematical, Physical and Engineering Sciences*, 225(1160):49–63, 1954.

[45] C. Campbell. Granular material flows - An overview. *Powder Technology*, 162(3):208–229, 2006.

[46] I. Lashgari, F. Picano, W. Breugem, and L. Brandt. Laminar, Turbulent, and Inertial Shear-Thickening Regimes in Channel Flow of Neutrally Buoyant Particle Suspensions. *Phys. Rev. Lett.*, 113(25):254502, December 2014.

[47] I. Gazuz and M. Fuchs. Nonlinear microrheology of dense colloidal suspensions: A mode-coupling theory. *Phys. Rev. E*, 87(3):032304, 2013.

[48] D. Acheson. *Elementary Fluid Dynamics*. Oxford University Press, 1990.

[49] H. Risken. *The Fokker-Planck equation : methods of solution and applications*. Springer, 1989.

[50] A Einstein. Über die von der molekularkinetischen Theorie der Wärme geforderte Bewegung von in ruhenden Flüssigkeiten suspendierten Teilchen. *Annalen der Physik*, 322(8):549, 1905.

[51] D. Reichman and P. Charbonneau. Mode-Coupling Theory (MCT) Lecture Notes. *J. Stat. Phys.*, page 05013, 2005.

[52] W. Götze. *Complex Dynamics of Glass-Forming Liquids-A Mode-Coupling Theory*. Oxford University Press, 2009.

[53] K. Kawasaki and J. Gunton. Theory of Nonlinear Transport Processes: Nonlinear Shear Viscosity and Normal Stress Effects. *Phys. Rev. A*, 8(4):2048, 1973.

[54] G. Morriss and D. Evans. Application of transient correlation functions to shear flow far from equilibrium. *Phys. Rev. A*, 35(2):792, 1987.

[55] M. Fuchs and M. Cates. Theory of Nonlinear Rheology and Yielding of Dense Colloidal Suspensions. *Phys. Rev. Lett.*, 89(24):248304, 2002.

[56] M. Fuchs and M. Cates. A mode coupling theory for Brownian particles in homogeneous steady shear flow. *J. Rheol.*, 53(4):957, 2009.

[57] T. Wang, M. Grob, A. Zippelius, and M. Sperl. Active microrheology of driven granular particles. *Phys. Rev. E*, 89(4):042209, 2014.

[58] M. Gnann, I. Gazuz, A. Puertas, M. Fuchs, and Th. Voigtmann. Schematic models for active nonlinear microrheology. *Soft Matter*, 7(4):1390, 2011.

[59] S. Strogatz. *Nonlinear Dynamics and Chaos*. Addison-Wesley, 1994.

[60] Ting Wang and Matthias Sperl. Thinning and thickening in active microrheology. *arXiv:1504.02277v1*, 2015.

[61] J. Reinhardt, A. Scacchi, and J. Brader. Microrheology close to an equilibrium phase transition. *J. Chem. Phys.*, 140(14):–, 2014.

[62] M. Green. Markoff Random Processes and the Statistical Mechanics of Time-Dependent Phenomena. II. Irreversible Processes in Fluids. *J. Chem. Phys.*, 22(3):398, 1954.

[63] R. Kubo. Statistical-Mechanical Theory of Irreversible Processes. I. General Theory and Simple Applications to Magnetic and Conduction Problems. *J. Phys. Soc. Jpn.*, 12(6):570, 1957.

[64] K. Binder and W. Kob. *Glassy Materials and Disordered Solids: An Introduction to Their Statistical Mechanics*. World Scientific Publishing Company, October 2005.

[65] M. Boas. *Mathematical methods in the physical sciences*. Wiley, Hoboken, NJ, 2006.

[66] W. Götze and Th. Voigtmann. Universal and nonuniversal features of glassy relaxation in propylene carbonate. *Phys.Rev.E*, 61:4133, 2000.

[67] W. Götze and M. Sperl. Nearly-logarithmic decay of correlations in glass-forming liquids. *Phys.Rev.Lett.*, 92:105701, 2004.

[68] Ch. Harrer, D. Winter, J. Horbach, M. Fuchs, and Th. Voigtmann. Force-induced diffusion in microrheology. *J. Phys.: Condens. Matter*, 24(46):464105, 2012.

[69] W. T. Kranz, M. Sperl, and A. Zippelius. Glass Transition for Driven Granular Fluids. *Phys. Rev. Lett.*, 104(22):225701, 2010.

[70] M. Sperl, W. T. Kranz, and A. Zippelius. Single-particle dynamics in dense granular fluids under driving. *Europhys. Lett.*, 98(2):28001, 2012.

[71] W. T. Kranz, M. Sperl, and A. Zippelius. Glass transition in driven granular fluids: A mode-coupling approach. *Phys. Rev. E*, 87(2):22207, 2013.